Advanced bioanalysis of light-controlled *S. cerevisiae* production strains

- Dissertation -

zur Erlangung des Grades eines
Doktor der Naturwissenschaften
(Dr. rer. nat.)
des Fachbereichs Chemie der Philipps-Universität Marburg

Vorgelegt von
Filipp Bezold
aus Wetzlar

Marburg, 2023

Die vorliegende Arbeit wurde unter der Betreuung von Herrn Prof. Dr. Lars-Oliver Essen von September 2017 bis Februar 2023 am Fachbereich Chemie der Philipps-Universität Marburg angefertigt.

Vom Fachbereich Chemie der Philipps-Universität Marburg (Hochschulkennziffer 1180) als Dissertation angenommen am: _____

Erstgutachter: Prof. Dr. Lars-Oliver Essen

Zweitgutachter: Priv. Doz. Dr. Christof Taxis

Tag der Disputation: _____

Eidesstattliche Erklärung

Ich versichere, dass ich meine Dissertation mit dem Titel:

"Advanced bioanalysis of light-controlled *S. cerevisiae* production strains"

selbstständig, ohne unerlaubte Hilfe angefertigt und mich dabei keiner anderen als der von mir ausdrücklich bezeichneten Quellen und Hilfen bedient habe.
Diese Dissertation wurde in der jetzigen oder einer ähnlichen Form noch bei keiner anderen Hochschule eingereicht und hat noch keinen sonstigen Prüfungszwecken gedient.

Ort, Datum	Filipp Bezold

Publications

Maestre-Reyna M, Wang P-H, Nango E, Hosokawa Y, Saft M, Furrer A, Yang C-H, Gusti Ngurah Putu E P, Wu W-J, Emmerich H-J, Franz-Badur S, Engilberge S, Caramello N, Wranik M, Glover H L, Weinert T, Wu H-Y, Lee C-C, Huang W-C, Huang K-F, Chang Y-K, Liao J-H, Weng J-H, Gad W, Chang C-W, Pang A H, Gashi D, Beale E, Ozerov D, Nass K, Knopp G, Johnson P J M, Cirelli C, Milne C, Bacellar C, Sugahara M, Owada S, Joti Y, Yamashita A, Tanaka R, Tanaka T, Luo F, Tono K, Müller P, **Bezold F**, Fuchs V, Gnau P, Kiontke S, Korf L, Reithofer V, Rosner C J, Werel L, Spadaccini R, Royant A, Yamamoto J, Iwata S, Standfuss J, Bessho Y, Essen L-O and Tsai M-D, "Watching the entire DNA repair process by a photolyase at atomic resolution in real time", manuscript in preparation

Bezold F, Scheffer J, Wendering P, Razaghi-Moghadam Z, Trauth J, Pook B, Nußhär H, Hasenjäger S, Nikoloski Z, Essen L-O and Taxis C "Optogenetic control of Cdc48 for dynamic metabolic engineering in yeast", manuscript submitted

Essen L-O, Taxis C, **Bezold F** and Scheffer J (2020) "Verfahren zur Herstellung eines Planzeninhaltsstoffes durch optogenetische Kontrolle von Zellzyklusregulatoren", patent: EP4006164A1

Gramazio S, Trauth J, **Bezold F**, Essen L-O, Taxis C, Spadaccini R (2022) "Light-induced fermenter production of derivatives of the sweet protein monellin is maximized in prestationary *Saccharomyces cerevisiae* cultures", Biotechnology Journal

Hepp S, Trauth J, Hasenjäger S, **Bezold F**, Essen L-O and Taxis C (2020) "An Optogenetic Tool for Induced Protein Stabilization Based on the *Phaeodactylum tricornutum* Aureochrome 1a Light-Oxygen-Voltage Domain", Journal of Molecular Biology

Linne U, **Bezold F** and Bamberger J (2019) "Coupling Methods in Mass Spectrometry", GIT Laboratory Journal

Wenn Sie die Art und Weise ändern, wie Sie die Dinge betrachten, ändern sich die Dinge, die Sie betrachten.

– Max Planck

Abstract

Vast progress in the field of biotechnology enabled metabolic engineering to become a powerful tool for the production of numerous biogenic substances in the last decade. Alongside methods for editing biological pathways, bioanalytical techniques play a central role in metabolic engineering approaches, as they allow for monitoring of pathway modifications, identification of bottlenecks and quantification of target substances.

The collaborative project "metabolic engineering with light controlled modules" (MELICOMO) aimed to harness optogenetic tools for the production of valuable secondary metabolites in *Saccharomyces cerevisiae* and to implement a light-inducible cell cycle arrest as the desired cellular production state. Within the present work a broad spectrum of bioanalytical methods was applied for the characterization of light-controlled *S. cerevisiae* cell cycle mutants (CCMs) and for the quantification of target molecules in the context of metabolic engineering.

The first part of this thesis summarizes results of biomass composition for cell cycle arrested Clb2$^{\Delta DB}$-psd^3 cells and the corresponding wild type (WT) strain. Here, growth-restricted Clb2$^{\Delta DB}$-psd^3 cells were found to contain more protein and RNA and less carbohydrates in comparison to WT cells.

Moreover, results of a proteomics experiment performed for the light-controlled CCM strains Cdc48-psd^3, Clb2$^{\Delta DB}$-psd^3 and bPAC were analyzed. Thereby, relative protein abundances comparing the restrictive growth conditions to the permissive growth conditions and to the WT strain were examined. Obtained results were processed using heatmaps, volcano plots, Venn diagrams and Gene Ontology enrichment analyses. Here, for each of the growth-restricted Cdc48-psd^3 and bPAC strains an acetyl-CoA synthetase isoform was found to be high abundant in comparison to the permissive growth condition and to the WT strain. This finding might explain increased β-carotene yields observed for both growth-restricted strains and indicates beneficial production conditions for other isoprenoid-derived products generated from precursors provided by the mevalonate pathway. Furthermore, the phosphatase Pho8 was found to be present at low levels in growth-restricted Cdc48-psd^3 cells compared with the WT strain, which may explain the observed increased cordycepin production of the growth-restricted CCM strain, since Pho8 is responsible for the degradation of the cordycepin precursor 3'AMP. In addition, enzymes of the respiratory chain and the tricarboxylic acid cycle were found to be upregulated for growth-restricted bPAC cells, which could imply an increased energy availability for this condition.

Finally a selection of LC-MS and HPLC analyses is shown, which helped to establish proof of principle 3'AMP, cordycepin and GA_4 production strains.

This thesis provides a large toolbox of state of the art bioanalytical methods, which helped to improve and rationalize the metabolic engineering approaches established within the MELICOMO project.

Zusammenfassung

Dank enormer Fortschritte im Bereich der Biotechnoligie hat sich *metabolic engineering* im letzten Jahrzehnt zu einer leistungsfähigen Methode entwickelt um die Herstellung biogener Substanzen zu ermöglichen. Neben molekularbiologischen Techniken spielen beim *metabolic engineering* bioanalytische Methoden eine zentrale Rolle.
Ziel des Projektes "*metabolic engineering with light controlled modules*" (MELICOMO) war es, optogenetische Werkzeuge für die Produktion wertvoller Sekundärmetabolite in *Saccharomyces cerevisiae* zu nutzen und einen lichtinduzierbaren Zellzykluss-Arrest als zellulären Produktionszustand zu implementieren. Dabei wurde im Rahmen der vorliegenden Arbeit ein breites Spektrum bioanalytischer Methoden für die Charakterisierung der Produktionsstämme und die Quantifizierung von Zielmolekülen etabliert.
Im ersten Teil der vorliegenden Arbeit werden die Ergebnisse einer Biomasse-Analyse von zellzyklusarretierten Clb2$^{\Delta DB}$-psd^3-Zellen und dem entsprechenden Wildtyp-Stamm zusammengefasst. Hier wurde festgestellt, dass zellzyklusarretierte Clb2$^{\Delta DB}$-psd^3-Zellen im Vergleich zum Wildtyp-Stamm mehr Protein und RNA und weniger Kohlenhydrate enthalten.
Darüber hinaus wurden Proteomics-Experimente zu den lichtgesteuerten Zellzyklus-Mutanten Cdc48-psd^3, Clb2$^{\Delta DB}$-psd^3 und bPAC durchgeführt und die Ergebnisse anhand von *heatmaps*, *vulcano plots*, Venn-Diagrammen und *Gene Ontology* Anreicherungs-Analysen diskutiert. Dabei wurde für den zellzyklusarretierten Cdc48-psd^3 und bPAC-Stamm im Vergleich zum permissiven Zustand und zum Wildtyp-Stamm jeweils eine hochabundante Acetyl-CoA-Synthetase-Isoform gefunden. Dies könnte die erhöhten Ausbeute an β-Carotin erklären, welche bei den beiden zellzyklusarretierten Stämmen festgestellt wurde und deutet auf generell günstige Produktionsbedingungen für Isoprenoide hin, die aus Produkten des Mevalonatwegs erzeugt werden. Desweiteren wurde festgestellt, dass die Phosphatase Pho8 in zellzyklusarretierten Cdc48-psd^3-Zellen im Vergleich zum Wildtyp-Stamm niedrig abundant ist, was die beobachtete erhöhte Cordycepin-Produktion des zellzyklusarretierten Cdc48-psd^3-Stamms erklären könnte, da Pho8 für den Abbau des Cordycepin-Vorläufers 3'AMP verantwortlich ist. Außerdem lagen beim zellzyklusarretierten bPAC-Stamm viele Enzyme der Atmungskette und des Citratzyklus hochabundant vor, was auf eine erhöhte Energieverfügbarkeit in diesem Zustand hindeuten könnte.
Im letzten Teil der Arbeit wird schließlich eine Auswahl von LC-MS- und HPLC-Analysen gezeigt, mit deren Hilfe die Etablierung von 3'AMP, Cordycepin und GA_4 Produktionsstämmen nachgewiesen werden konnte.
Damit stellt diese Arbeit eine umfangreiche Toolbox modernster bioanalytischer Methoden bereit, die dazu beigetragen haben, die im Rahmen des MELICOMO-Projekts etablierten *metabolic engineering* Ansätze zu verbessern und zu rationalisieren.

Abbreviations

Abbreviation	Term
AC	adenylate cyclase
ACN	acetonitrile
BLUF	blue light using flavin
BSA	bovine serum albumin
CCM	cell cycle mutant
DAD	diode array detector
DAP	differentially abundant protein
DB	destruction box
DBAA	dibutylammonium acetate
DNA	deoxyribonucleic acid
EC	end-capped
EIC	extracted ion chromatogram
ER	endoplasmic reticulum
ERAD	ER-associated protein degradation
FA	formic acid
FBA	flux ballance analysis
FDR	false discovery rate
FMN	flavinmononucleotid
FPP	farnesyl pyrophosphate
FT-ICR	fourier transform ion cyclotron resonance
GA_4	gibberellin A_4
GB	gigabyte
GGPP	geranylgerarnyl pyrophosphate
GO	Gene Ontology
$dd H_2O$	double-distilled water
HAc	acetic acid
HPLC	high performance liquid chromatography
IAA	iodoacetamide
ID	identification
IEC	Ion exchange column

Abbreviation	Term
LC	liquid chromatography
LCM	light controlled mutant
LFM	low fluorescence media
LFQ	label free quantification
LOD	limit of detection
LOQ	limit of quantification
LOV	ight oxygen voltage
MELICOMO	metabolic engineering with light controlled modules
MPI	Max Planck Institute
MRM	multiple reaction monitoring
MS	mass spectrometer
MWD	multiple wavelength detector
NAC	*N*-acetylcysteine
NC	not calculated
ND	not detected
ONC	overnight culture
O/N	overnight
PAS	Per-Arnt-Sim
PKA	protein kinase A
psd	photosensitive degron
RNA	ribonucleic acid
RP	reversed phase
RT	room temperature / retention time
SC	synthetic complete
SGD	*Saccharomyces* genome database
TCA	tricarboxylic acid cycle
TCEP	tris(2-carboxyethyl)phosphine
TC flask	tissue culture flask
TFA	trifluoroacetic acid (TFA)
TIC	total ion current
UV	ultra-violet

Contents

Chapter 1

Introduction

1.1 *S. cerevisiae*, Eukaryotic Model Organism and Versatile Host for Metabolic Engineering

In 1996, the budding yeast *S. cerevisiae* became the first eukaryotic organism to have its genome completely sequenced and has been studied extensively as a eukaryotic model organism because of its ease of cultivation and genetic manipulation.[36] *S. cerevisiae* can exist either haploid (mating type **a** and α) or diploid and two haploid cells of the opposite mating types readily mate to form diploids. Under nutrient-poor conditions, meiosis of diploid cells is induced, forming four haploid spores from diploid cells. In the haploid form of *S. cerevisiae*, gene mutations can be readily studied and a wide range of specific/conditional knockout mutants for haploid and diploid strain backgrounds were made commercially available to facilitate high throughput screening.[34] The genome of *S. cerevisiae* harbors ≈ 6000 open reading frames (ORFs), of which ≈ 5000 have a known function and 18 % of the total ORFs were found to be essential for growth on rich glucose medium.[28][35] Since many fundamental processes and biochemical pathways are conserved among yeast and higher eukaryotes, *S. cerevisiae* has been intensively studied to gain a better understanding of DNA repair, mRNA translation/degradation, and the cell cycle.[34] Moreover ≈ 40 % of the *S. cerevisiae* proteins have significant sequence similarity to at least one human protein (BLAST E-value $< 10^{-10}$), with hundreds of the human orthologs known to be involved in disease.[85] Consequently, *S. cerevisiae* is used as a model organism to understand diseases, a prominent example being research by Yoshinori Ōsumi on autophagy for which he was awarded the Nobel Prize in 2016.
Cultivation of *S. cerevisiae* for the production of fermented foods, wine, beer and sake has been practiced for millennia by societies around the globe and a vast number of specialized strains are used today by food industry and biofuel companies in order to convert carbon sources into products.[66] Economically, the most important industrial application of *S. cerevisiae* is the production of ethanol. Here *S. cerevisiae* is pre-dominatly responsible for the 100 billion liters of ethanol produced annually worldwide. The two

major ethanol producing countries are the United States of America, where 40 % of the corn harvest is used for the production of ethanol, and Brazil, where sugar cane is used for ethanol production. Each industry relies on a different specialized yeast strain, as the substrates and fermentation processes are fundamentally different.[30]

A targeted approach for the development of cell factories to produce desired compounds is metabolic engineering. This involves the rational genetic manipulation of cellular pathways to enable the production of specific targets or to increase the titer of an established production. As an example metabolic engineering is used to expand the substrate spectrum of the host organism or to improve the organism's stress tolerance towards the production conditions, with the goal of efficiently converting low-cost feedstock into valuable products.[67] In this context, metabolic engineering aims to create sustainable alternatives to conventional fossil fuel-based production and to the costly extraction of natural products from biological matrices. In metabolic engineering establishment of production strains is driven by iterative rounds of design/build/test/learn cycles.[87] This concept serves to integrate the results of a rationally designed modification into the next round of the genetic engineering process. Each step of the optimization cycle benefits greatly from scientific advances of the past decades. Rational pathway design takes advantage from a wealth of accessible information about biological systems, modern gene editing allows short turnover times for genetic modifications, advanced analytical instruments have become readily available to laboratories and data analysis has benefited greatly from software and hardware improvements. In addition, methods of systems biology such as metabolic flux modeling are already helping to streamline metabolic pathway design, and in perspective, machine learning might fundamentally revolutionize metabolic engineering approaches.[5] [65]

S. cerevisiae is used as a platform organism for metabolic engineering approaches due to the in-depth understanding of its metabolism and because it is easy to culture and genetically manipulate – reasons that made *S. cerevisiae* a model organism in the first place. In addition, this yeast is generally recognized as safe (GRAS) which facilitates industrial application.[67] As an eukaryote, *S. cerevisiae* harbors multiple cellular compartments which are often necessary for pathway establishment. Furthermore, it is capable of many post-translational modifications to produce functional recombinant eukaryotic enzymes. *S. cerevisiae* was engineered to develop industrial scale biorefineries for the production of platform chemicals including organic acids, sugar alcohols, furans, isoprene and glycerol derivatives. Current progress in this field has been described in detail by Baptista *et al.*[9] Moreover, the successful production of a large number of high-value fine chemicals, such as the cholesterol-lowering drug simvastatin acid or cannabinoids has been demonstrated in *S. cerevisiae*.[15] [72]

1.1.1 Isoprenoid Production in Yeast

Isoprenoids or terpenoids are the largest class of natural compounds, with numerous biological functions and industrial applications. They derive from C5 building blocks provided by isopentenyl diphosphate (IPP) and dimethylallyl diphosphate (DMAPP) and comprise mono- (C10), sesqui- (C15), di- (C20), sester- (C25), tri- (C30), tetra- (C40) and polyterpenoids, which can be composed of thousands of repeating isoprene subunits.[99] Isoprenoids are present in all living organisms and have diverse functions. They influence membrane fluidity, attenuate environmental stress, function as photoprotection or photosynthetic pigments, are substrates in the prenylation of proteins, are signal molecules to attract or repulse organisms and regulate growth in plants.[8] Furthermore isoprenoids play an important role in many industrial applications as pharmaceuticals, nutraceuticals, agricultural chemicals, flavors/fragrances, chemical feedstocks, colorants and as fuels or fuel additives in petroleum industry.[102] The isomeric isoprenoid precursors IPP and DMAPP are supplied by the cytosolic mevalonate pathway in archea, few eubacteria (probably through horizontal gene transfer events) and eukaryotes. In addition, both molecules are produced via the methylerythritol phosphate pathway, which is present in most bacteria and in chloroplasts.[99] [59] In the past, isoprenoid precursors derived from the yeast mevalonate pathway were used as precursors in metabolic engineering approaches in order to produce isoprenoids such as the antimalarian drug artemisinin and the antibacterial molecule limonene at high titers.[83] [23] Yeast is often the preferred host organism for isoprenoid production, as yeast readily expresses functional recombinant cytochrome P450 monooxygenases, which are obligatory for the synthesis of many modified isoprenoids.[59]

Within the MELICOMO project mainly two isoprenoids/isoprenoid-derivatives were produced via recombinant pathways in *S. cerevisiae*: The plant hormone gibberellin A_4 (GA_4) and the terpene β-carotene. As visualized in figure 1.1, synthesis of both molecules branches off ergosterol biosynthesis from farnesyl pyrophosphate (FPP) via the common endogenous precursor geranylgeranyl pyrophosphate (GGPP). GA_4 is a plant hormone applied in agriculture e.g. to prevent russeting on apple fruits and in the production of seedless fruit. On the commercial scale it is available from fermentation extracts of the fungus *Fusarium (Gibberella) fujikuroi*. Nevertheless, due to purification difficulties, GA_4 is commercially available only contaminated with GA_7.[88] This is problematic because different biological effects have been described for the two gibberellins. For instance, GA_7 is reported to inhibit flowering in apple, while GA_4 promotes flowering in apple.[20] In order to produce pure GA_4, the recombinant GA_4 production pathway established during the MELICOMO project aimed to mimic GA_4 production in plants. Here GA_4 is generated without GA_7 as unwanted side product and GGPP is converted to *ent*-kaurenoic acid by catalytic activity of *ent*-copalyl diphosphate synthase (CPS), *ent*-kaurene synthase (KS) and the cytochrome P450 monooxygenase *ent*-kaurene oxidase

(KO). Subsequently *ent*-kaurenoic acid is further oxidized by the second cytochrome P450 monooxygenase *ent*-kaurenoic acid oxidase (KAO) and converted to GA_4 by catalytic activity of gibberellin 20-oxidase and gibberellin 3-oxidase. Furthermore, the redox state of the heme cofactor of P450 monooxygenases has to be restored by a plant reductase in order to enable GA_4 generation via the recombinant pathway.

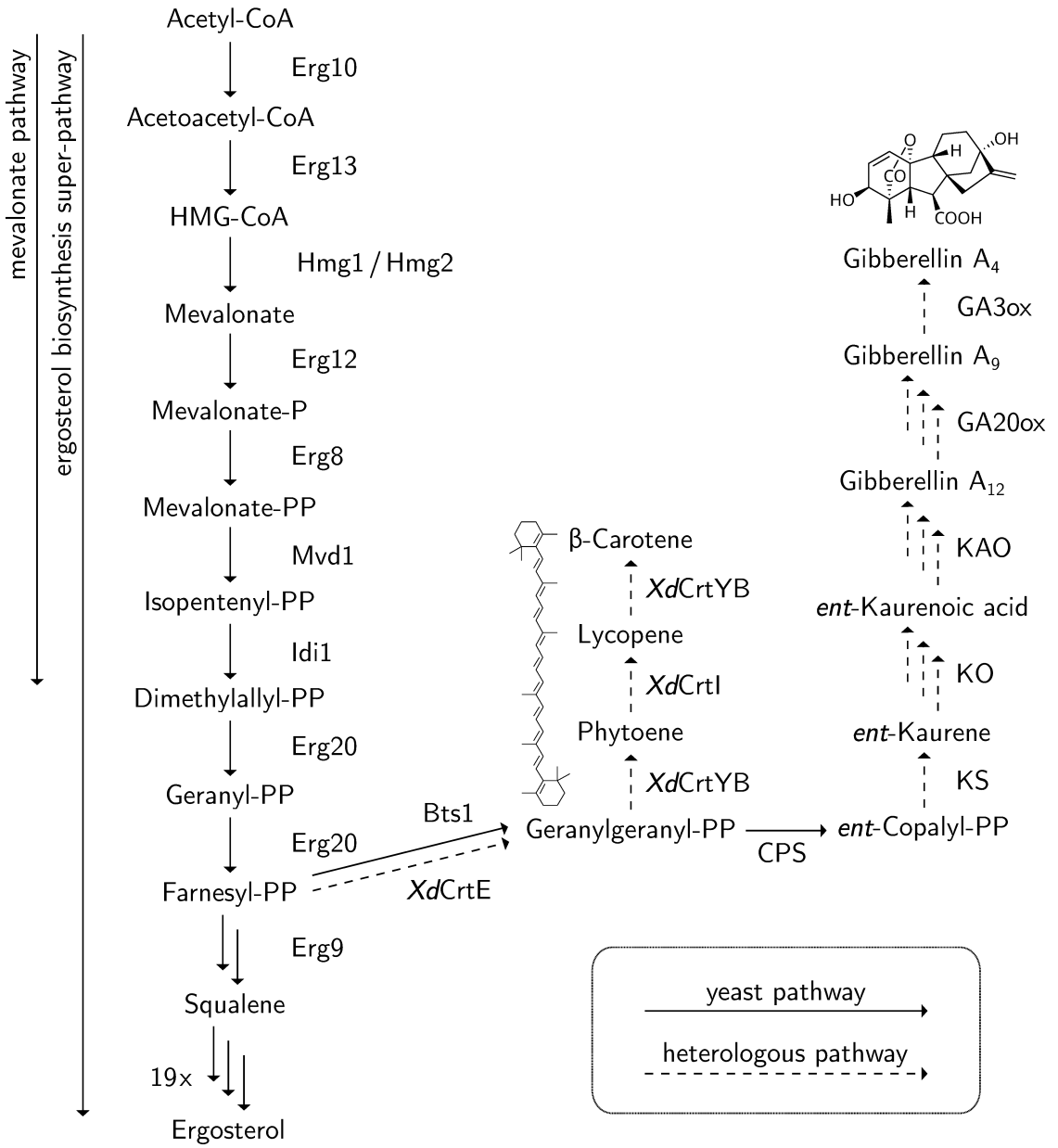

Figure 1.1: Schematic of the ergosterol biosynthesis superpathway in *S. cerevisiae* including the mevalonate pathway and the heterologous pathways established within the MELICOMO project for the production of β-carotene and Gibberellin A_4.

The second target molecule derived from intermediates of the mevalonate pathway was the red-orange pigment β-carotene. Among other things β-carotene plays a role in photoprotection and photosynthesis in plants and as provitamin A in human nutrition. Within the MELICOMO project β-carotene was used as a well established reporter molecule to monitor the production capacity for target molecules derived from the mevalonate pathway for different yeast strains. Corresponding strains expressed the bifunctional lycopene cyclase/phytoene synthase CrtYB and the phytoene desaturase CrtI from *Xanthophyllomyces dendrorhous* in order to enable β-carotene production from GGPP. In addition the geranylgeranyl pyrophosphate synthase *Xd*CrtE was expressed to increase the availability of GGPP for β-carotene production.[10]

1.2 Optogenetics

Optogenetics describes the use of genetically encoded light-responsive proteins to control cellular activity.[80] For the generation of optogenetic tools a wide variety of photoreceptors from different host organisms have been engineered in the past to enable photoinducible physiological responses. The optogenetic toolbox includes proteins responsive to the visible and non-visible regions of the light spectrum, including UV, violet, blue, cyan, green, red and far-red light.[60] Essential for an optogenetic tool is a chromophore, in most cases a cofactor, which absorbs light of a specific wavelength and mediates the induced photoexcitation to an effector module. Depending on the chromophore and the surrounding protein scaffold, photoexcitation can lead to the formation or cleavage of covalent bonds, change in hydrogen-bonding, photoreduction, or photoisomerization of the chromophore.[80] Thus, excitation of the chromophore induces changes in the conformation or the general physicochemical properties of the protein. This either directly affects the function/signaling of the protein or leads to the formation or dissociation of homomeric or heteromeric protein complexes as a result of changes in interaction surfaces. In a functional optogenetic tool, the light response is transferred to an effector domain, which subsequently changes its functionality. So far several receptor and effector domains have been combined to create optogenetic tools with the desired excitation properties and physiological response. The potential applications for optogenetic tools are broad and optogenetics has been used in the past e.g. to trigger gene expression by light-dependent transcription factors, to induce protein degradation, or to control neural activity by light-sensitive ion channels.[90] [89] [16] Light as an inducer of cellular processes has many advantages because it is inexpensive, in general non-toxic, adjustable in intensity and can be precisely controlled in a temporospatial fashion. In addition, the activation of many optogenetic tools is reversible by incubation in the dark and/or by exposure to light of a specific wavelength.

The light-oxygen-voltage (LOV) domain

Light-oxygen-voltage (LOV) domains are flavin binding blue-light sensory modules present in bacteria, archaea, plants and fungi.[48] At its core a LOV domain consists of a five-stranded antiparallel β-sheet and four α-helices in Per-Arnt-Sim (PAS) fold binding the cofactor. The core is flanked by an N-terminal A'α helix and a C-terminal Jα helix (see figure 1.2A).[104] Upon photoexcitation a metastable covalent bond is formed between the flavin cofactor and a neighboring cystein. The formation of the covalent bond triggers a conformational change and unfolding of the A'α helix, which promotes undocking and unfolding of the Jα helix.[114] Photoexcitation is reversible under dark conditions. This reaction, called dark reversion, is thermally controlled and takes minutes to hours, depending on the LOV domain.[57] Through their response to light, LOV domains induce a wide variety of biological responses in host organisms e.g. activation of sterically blocked effectors, reorientation of protein domains or homo-/heterodimerization.[94] In addition, linear amino acid motifs fused to the Jα helix are masked in the dark state of the protein and were found to be exposed to interaction partners under blue light conditions. These properties make LOV domains a highly interesting target for the development of optogenetic tools.

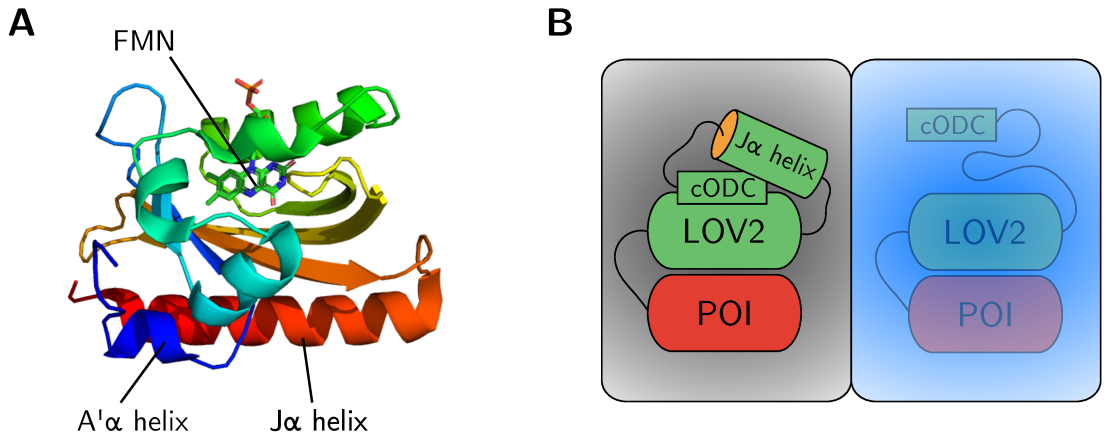

Figure 1.2: **A** Crystal structure of the AsLOV2 domain (PDB identifier: 2V0U). **B** Schematic of the blue light induced degradation of a protein of interest (POI) fused to the psd-module.

Within the MELICOMO project the photosensitive degron (psd) module, developed by Renicke *et al.*, was used to induce degradation of target proteins in *S. cerevisiae* under blue light conditions.[89] The psd module consists of the murine ornithine decarboxylase-like degradation sequence cODC1 fused to the C-terminus of a phototropin LOV2 domain. The psd in turn is genetically fused to the gene of the target protein whose stability is to be controlled. Upon exposure to blue light the LOV2 Jα helix unfolds and exposes the degron sequence to the proteasome, which leads to the degradation of the entire protein (figure 1.2B). In the present work, mostly the third generation psd module

(psd^3) was used. The psd^3 is derived from the flavin mononucleotide (FMN) binding LOV2 domain of *Avena sativa* phototropin, edited based on published mutations[41] and by deletion of alanine in position 146. The psd^3 module has a switching ratio of $\approx$ 40, which is about ten times higher than the original psd module and shows a significantly shorter half-life time to become fully active.[43]

The blue light using flavin (BLUF) domain

Photosensing blue light using flavin (BLUF) domains are present in prokaryotes, unicellular eukaryotes and fungi.[71] BLUF domains consist of about 100 amino acids and adopt a ferredoxin-like fold. They have a conserved tyrosine, glutamine, and methionine residue in the cofactor-binding region, and each of these amino acids is essential for signaling to the effector domain.[84] Even though the exact mechanism following cofactor excitation is still a matter of debate, the proposed mechanisms agree on a proton-coupled electron transfer, which leads to a rearrangement of the hydrogen bonds with the conserved glutamine in the flavin-pocket. The altered hydrogen-bonding propagates large conformational changes in the protein, which in turn triggers in the biological context activation of a large variety of effector domains or induces changes in interaction surfaces.[33] [56] Characteristic for BLUF photoreceptors is a $\approx$ 10 nm redshift in the absorption spectra for the signaling state caused by the altered hydrogen bonding of the chromophore.[84]

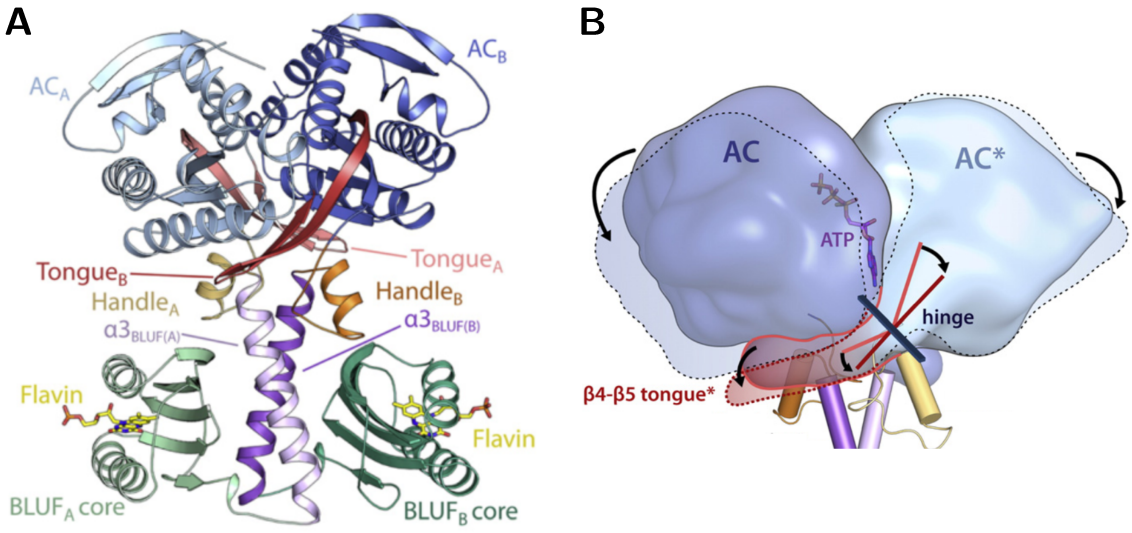

Figure 1.3: **A** Crystal structure of the bPAC homodimer with labeled structural features. **B** Visualization of the blue light induced rotation of the AC domains for the bPAC dimer. Images shown were published by Lindner *et al.*[68]

An optogenetic tool used in the present work containing a BLUF domain was the photoactivatable adenylate cyclase from *Beggiatoa* (bPAC). bPAC consists of a N-terminal BLUF domain and a C-terminal class III adenylate cyclase (AC) and is a popular optogenetic tool due to its small size, low dark activity and large increase in activity upon light exposure.[68] bPAC forms a parallel dimer and dimerizes via an intermolecular coiled coil interaction of the two α3 helices in the BLUF domain regions as visualized by figure 1.3. When exposed to light, activation of the BLUF domains triggers rotation of the AC domains around a hinge region, opening the active site and repositioning amino acids for substrate binding.[68] Adenylate cyclases provide the cell with the secondary messenger cAMP, which activates the cAMP-dependent protein kinase (PKA). PKA activity regulates many cellular processes such as growth, proliferation, metabolism, stress resistance, aging, morphogenesis and signaling of nutrient availability.[18] Within the MELICOMO project Cyr1, the endogenous adenylate cyclase of *S. cerevisiae*, was substituted by bPAC in order to control cellular cAMP concentrations in a blue light dependent manner. Here experiments focused on growth restriction of corresponding *S. cerevisiae* strains in darkness as inactivation of the PKA leads to cell cylce arrest in the G1 phase of the cell cycle.[112]

1.3 Cell Cycle of *S. cerevisiae*

The cell cycle is a highly conserved process among eukaryotes and consists of G1 (gap 1), S (synthesis), G2 (gap 2) and M (mitotic) phase. During the *S. cerevisiae* G1 phase, the cell grows and assesses at the "Start" checkpoint whether environmental and internal conditions are met to initiate cell cycle progression or to delay/arrest the cell cycle.[4] When all requirements are met, the cell prepares to enter the S phase, where DNA is replicated in preparation for mitosis. After DNA replication is complete, the cell transitions to G2 phase, continues to grow and repairs DNA defects before entering M phase. The mitotic phase is further divided into prophase (chromosome condensation, formation of the spindle apparatus), prometaphase (attachment of the spindle apparatus to the chromosomes, breakdown of the nuclear envelope), metaphase (alignment of the chromosmes at the metaphase plate), anaphase (separation of sister chromatids), telophase (formation of the nuclear envelope), followed by cytokinesis (separation of daughter cells), after which the two newly formed cells re-enter G1 phase.[105]

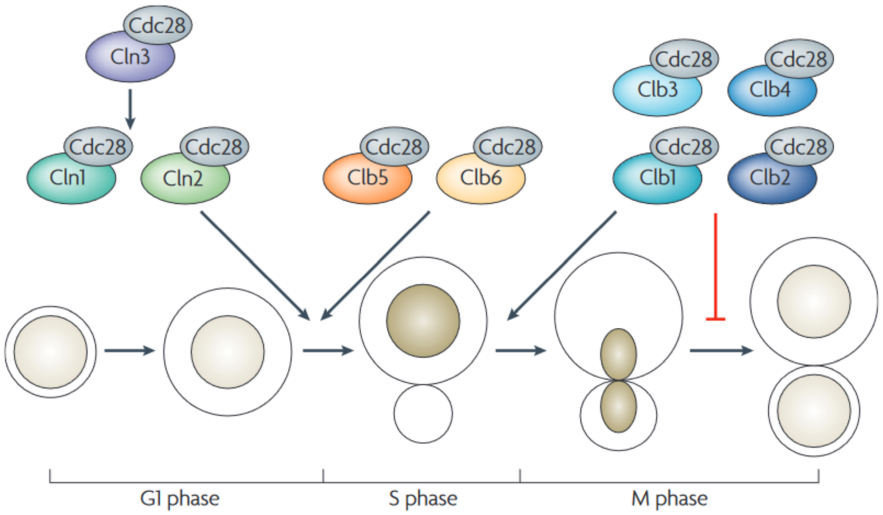

Figure 1.4: Schematic representation of cyclin-Cdc28 complexes involved in cell cycle progression for *S. cerevisiae*. The arrows point at the timing of expression during the cell cycle. The red marker indicates that late B cyclins must be depleted from the cell to undergo cytokinesis. Image shown was published by Bloom *et al.*[13]

Cell cycle progression is tightly regulated by the cyclin-dependent serine/threonine kinase Cdk1 (Cdc28), which mediates gene cluster expression by binding to activating cyclin subunits. During the cell cycle different sets of cyclins are expressed, inhibited and degraded to control the specificity of Cdc28 towards its targets. The degradation of cyclins is regulated by several ubiquitin ligase complexes that initiate specific proteolysis of the respective cyclins by the 26S proteasome. The transcriptional regulation of the G1/S gene cluster is well described. During G1 phase Cln3 is retained at the ER and is released in the late G1 phase to trigger "Start", when critical Cln3 levels are reached in the nucleus.[101] Here Cln3-Cdc28 activates the transcription factors SBF and MBF which leads to the expression of *CLN1* and *CLN2* (SBF-dependent) and the B-cyclins *CLB5* and *CLB6* (MBF-dependent). Subsequently, Cln1-Cdc28 and Cln2-Cdc28 provide a positive feedback-loop to further activate SBF and MBF.[42] Activation of Cdc28 by the G1-phase cyclins Cln1, Cln2, and Cln3 leads to transcription of genes required for bud emergence and polarized growth. Later in the cell cycle Clb2-Cdc28 inhibits the expression of the G1 cyclins *CLN1* and *CLN2*. During G1 phase the Clb-Cdc28 inhibitor Sic1 inhibits Clb5-Cdc28 and Clb6-Cdc28 activity but is progressively phosphorylated by Cln1-Cdc28 and Cln2-Cdc28, leading to its degradation and activation of Clb5-Cdc28 and Clb6-Cdc28 during S phase. Here, Clb5-Cdc28 and Clb6-Cdc28 are responsible for the expression of genes necessary for DNA replication. During M phase the B cyclins Clb1, Clb2, Clb3 and Clb4 drive gene expression and are ultimately ubiquitylated by the anaphase-promoting complex (APC) for mitotic exit and cell division.[13]

The desired production state for *S. cerevisiae* cells in the MELICOMO project was cell cycle arrest, and several different cell cycle mutant (CCM) strains were generated during the project. Within the present work three different CCM strains were tested. As described in section 1.2, for bPAC cells G1 arrest is induced at "Start" by incubation in darkness due to PKA inactivation.[112] For the Clb2$^{\Delta DB}$-psd^3 CCM strain an additional copy of *CLB2* is expressed lacking the destruction box (DB) and fused to the 3rd generation photosensitive degron (psd). Deletion of the destruction box, disables APC-mediated targeted degradation of the protein during the cell cycle and brings Clb2$^{\Delta DB}$-psd^3 degradation under blue light control. Under restrictive, dark growth conditions, Clb2$^{\Delta DB}$-psd^3 accumulates in the cell and the cell cycle arrests at the transition from metaphase to anaphase, as Clb2$^{\Delta DB}$-psd^3 prevents the cell from exiting M phase.[89] [13] For the Cdc48-psd^3 strain endogenous Cdc48 was genetically fused to psd^3. The essential AAA-ATPase Cdc48 participates in many cellular processes, including endoplasmic reticulum-associated degradation (ERAD), where it is central part of an adaptor complex to extract misfolded and ubiquitylated protein from the endoplasmic reticulum.[25] Conditional Cdc48 mutants show cell cycle arrest at the metaphase-anaphase transition, which can be induced by blue light in Cdc48-psd^3.[89] During anaphase Cdc48 is reported to promote the nuclear localization of tyrpe I phosphatase to antagonize Aurora B kinase activity.[24] In addition, Cdc48 and its adaptor Ubx4 affect proteasome distribution, leading to impaired degradation of B-cyclins, which prevents the cell from undergoing cytokinesis.[25]

1.4 Scope of the Project

The project "metabolic engineering with light controlled modules" (MELICOMO) aimed to harness optogenetic tools for the production of valuable secondary metabolites in *S. cerevisiae*. Within the project PhD students supervised by Prof. Dr. L.-O. Essen and Dr. Christof Taxis at Philipps University Marburg collaborated with the working group of Prof. Dr. Zoran Nikoloski at the university of Potsdam. The team in Marburg contributed to the project by generating corresponding *S. cerevisiae* production strains and by advancing respective optogenetic tools. The role of the working group of Prof. Dr. Zoran Nikoloski was to perform metabolic flux calculations adapted to the light-controlled yeast strains in order to identify bottlenecks for the production of the desired molecules. The MELICOMO project relied strongly on data for the evaluation of production capacities for different yeast strains and as a solid basis for flux modeling calculations. Hence, the present work aimend to establish reliable analytical workflows, providing required experimental data on:

1. Biomass composition of cell cycle arrested *S. cerevisiae* for metabolic flux modeling.
2. Effects of growth restriction on the proteome for *S. cerevisiae* cell cycle mutants.
3. Analyte quantification for *S. cerevisiae* production strains.

Chapter 2

Results

2.1 Biomass Analysis of Light-Controlled *S. cerevisiae*

Within this work a series of protocols for the quantification of *S. cerevisiae* biomass composition was implemented from literature. Protocols were down-scaled for application on 96-well plates and modified to suit the instrumentation provided by the university. The main goal was to investigate differences in biomass composition between cell cycle mutant (CCM) and wild type (WT) cells. Resulting protocols were used to provide a robust data basis for metabolic flux modeling performed by the group of Prof. Dr. Zoran Nikoloski at the university of Potsdam. Thereby a full analysis quantifying protein, carbohydrates, DNA, RNA and lipids was conducted for Clb2$^{\Delta DB}$-psd^3 cells grown under restrictive conditions and the corresponding WT strain. Furthermore, protein content was quantified for cells of the Clb2$^{\Delta DB}$-psd^3, Cdc48-psd^3 and bPAC CCM strains, grown under restrictive and permissive conditions, including the corresponding WT strains.

2.1.1 Cell Cultivation

In order to investigate differences in biomass composition between CCM and WT cells Clb2$^{\Delta DB}$-psd^3 was grown under restrictive conditions and corresponding WT cells were cultured as described in section 4.1.1. Obtained Clb2$^{\Delta DB}$-psd^3 cells showed the distinct enlarged budding phenotype as visualized in figure 2.1.[89] In general, WT cells grew to a higher OD (e.g. $OD_{WT\ (batch2)} \approx 6.1$ vs. $OD_{Clb2\ (batch2)} \approx 3.3$) but interestingly the difference in dry mass was less prominent (e.g. $m_{WT\ (batch2)} \approx 2.3\,g$/replicate vs. $m_{Clb2(batch2)} \approx 1.5\,g$/replicate). Accordingly, normalized to OD the Clb2$^{\Delta DB}$-psd^3 cells had 20 % more dry mass compared to WT cells.

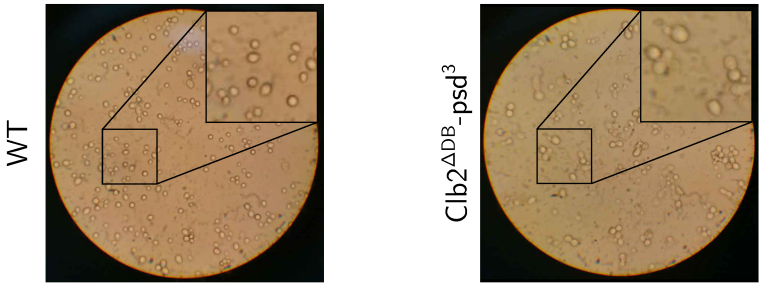

Figure 2.1: Microscopy pictures of Clb2$^{\Delta DB}$-psd^3 cells grown under restrictive growth conditions and corresponding WT cells. Clb2$^{\Delta DB}$-psd^3 cells showed for the most part a distinct enlarged budding phenotype. A magnified section is visualized in each picture.

2.1.2 Protein Quantification

Down-scaling of the instructions provided by Lange *et al.*[64] was straight forward, resulting in a robust protocol with minimal sample consumption. Results of protein quantification for Clb2$^{\Delta DB}$-psd^3 grown under restrictive conditions and the corresponding WT strain are shown in figure 2.2. The displayed data is summarized in the tables 5.1 and 5.2 in the appendix.

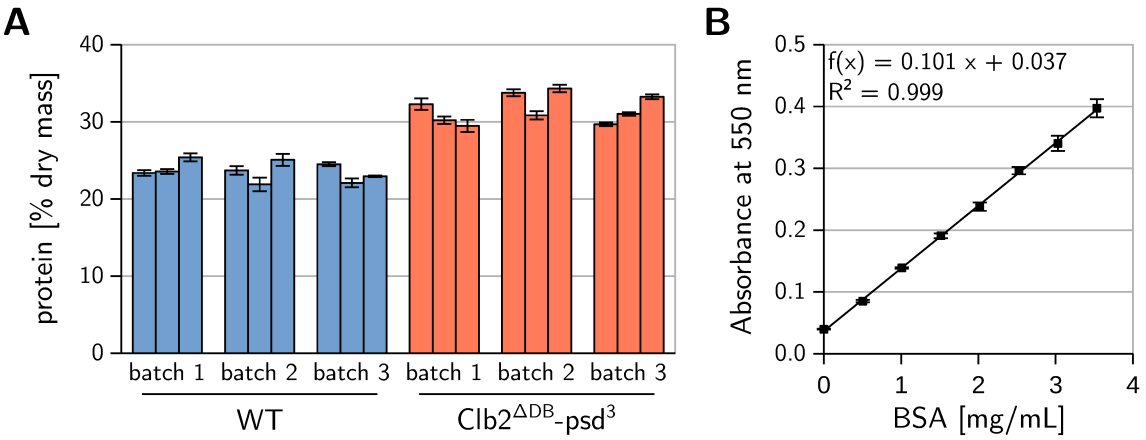

Figure 2.2: **A** Quantification of protein content from dry mass of Clb2$^{\Delta DB}$-psd^3 cells cultured under restrictive growth conditions and corresponding WT cells. Error bars represent standard deviation of three measurements. **B** Linear regression of the absorption for dried BSA standards.

On average Clb2$^{\Delta DB}$-psd^3 cells contained 31.7 % protein in relation to dry mass and standard deviation over all 9 biological replicates was $\pm$ 1.7 %. WT cells contained 23.6 % protein with a standard deviation of 1.2 %. The result of a two-sided unpaired Student's t-test comparing the protein content for biological replicates of Clb2$^{\Delta DB}$-psd^3 and WT was $7 \cdot 10^{-9}$. Hence, the mean protein content for both strains was clearly distinguishable from one another and was significantly increased for Clb2$^{\Delta DB}$-psd^3 cells.

2.1.3 Amino-Acid Composition

Results for amino-acid quantification from samples obtained by oxidative, acidic and alkaline protein hydrolysis are summarized in figure 2.3. Noteworthy, asparagine and aspartic acid, as well as glutamine and glutamic acid were indistinguishable after acidic protein hydrolysis and were quantified as aspartate and glutamate respectively. Many amino-acids were found to be higher abundant in Clb2$^{\Delta DB}$-psd^3 cells, exceptions were cysteine, alanine, lysine, arginine and tryptophan. This finding reflects the overall higher protein content of Clb2$^{\Delta DB}$-psd^3 cells already described in section 2.1.2. Protein content calculated on the basis of amino-acid composition was 35.6 % for Clb2$^{\Delta DB}$-psd^3 cells with a standard deviation of 1.4 % and 31.6 $\pm$ 1.2 % for corresponding WT cells. These values are significantly higher compared to the results shown in section 2.1.2.

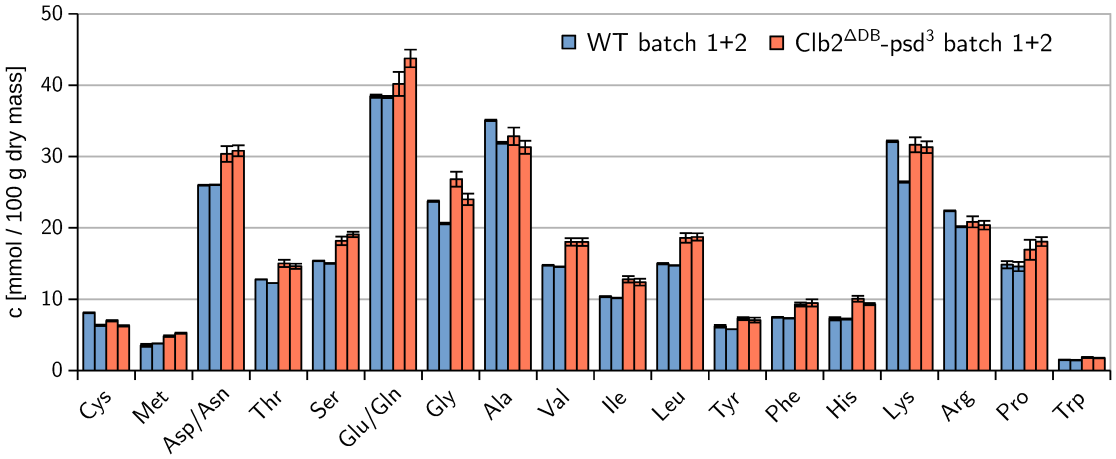

Figure 2.3: Amino-acid composition of Clb2$^{\Delta DB}$-psd^3 cells grown under restrictive growth conditions and corresponding WT cells. Error bars represent standard deviation of three measurements.

2.1.4 Carbohydrate Quantification

The implementation of the protocol for carbohydrate determination in 96-wells plates was laborious. Timing and routine handling were key to obtain reproducible results. In particular, the protocol step of diluting the concentrated sulfuric acid with the aqueous sample solution had a strong effect on the standard deviations obtained.

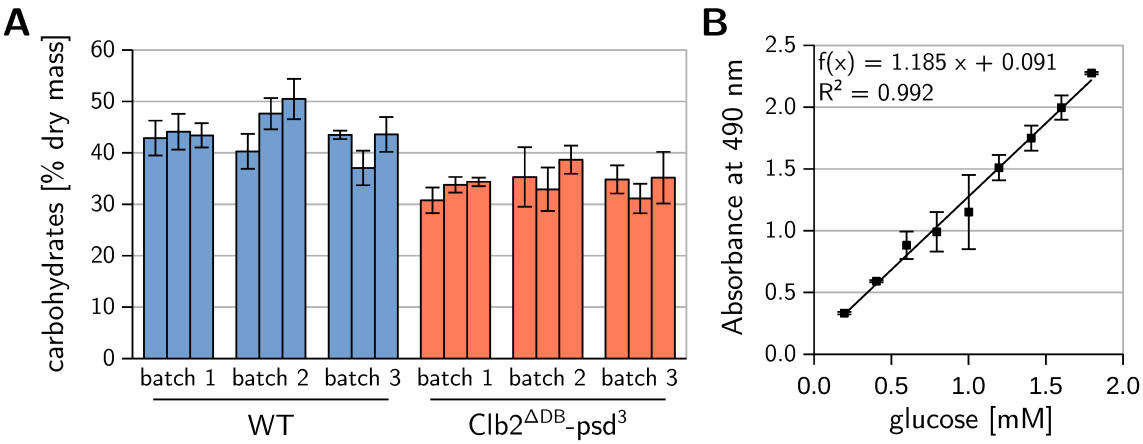

Figure 2.4: **A** Quantification of carbohydrate content from dry mass of Clb2$^{\Delta DB}$-psd^3 cells cultured under restrictive growth conditions and corresponding WT cells. Error bars represent standard deviation of three measurements. **B** Linear regression of the absorption for dried glucose standards.

Analyzed Clb2$^{\Delta DB}$-psd^3 cells contained 34.1 % carbohydrates. Here, standard deviation was 2.3 % and for corresponding WT cells a carbohydrate content of 43.7 $\pm$ 3.6 % was determined. Carbohydrate contents for biological replicates of both strains were tested using a two-sided unpaired Student's t-test. The resulting p-value of $9.9 \cdot 10^{-9}$ showed that carbohydrate content was significantly increased for WT cells compared to the Clb2$^{\Delta DB}$-psd^3 strain.

2.1.5 RNA and DNA Quantification

The scaled down protocol for consecutive RNA and DNA extraction from the same cell pellet was found to be reliable and reproducible. In this work, UV-determination of DNA content as described by Lange *et al.*[64] was replaced by the diphenylamin method, commonly used for the determination of DNA in literature. For RNA a recovery factor of 85.3 % was obtained and recovery for DNA was found to be quantitative.

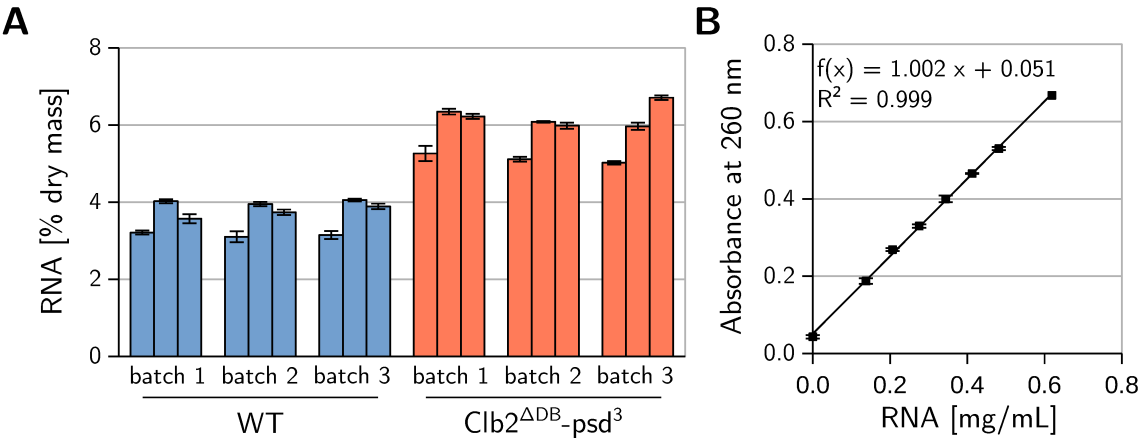

Figure 2.5: **A** Quantification of RNA content from dry mass of Clb2$^{\Delta DB}$-psd^3 cells cultured under restrictive growth conditions and corresponding WT cells corrected for RNA recovery of 85.3 %. Error bars represent standard deviation of three measurements. **B** Exemplary linear regression of the absorption for RNA standards.

Average RNA content of Clb2$^{\Delta DB}$-psd^3 cells was 5.9 % and standard deviation was 0.6 %. For corresponding WT cells, RNA content was determined to be 3.6 $\pm$ 0.4 %. The result of an two-sided unpaired Student's t-test comparing biological triplicates of both yeast strains was 6.0·10^{-8}, hence RNA content was significantly increased for Clb2$^{\Delta DB}$-psd^3 compared to WT cells.

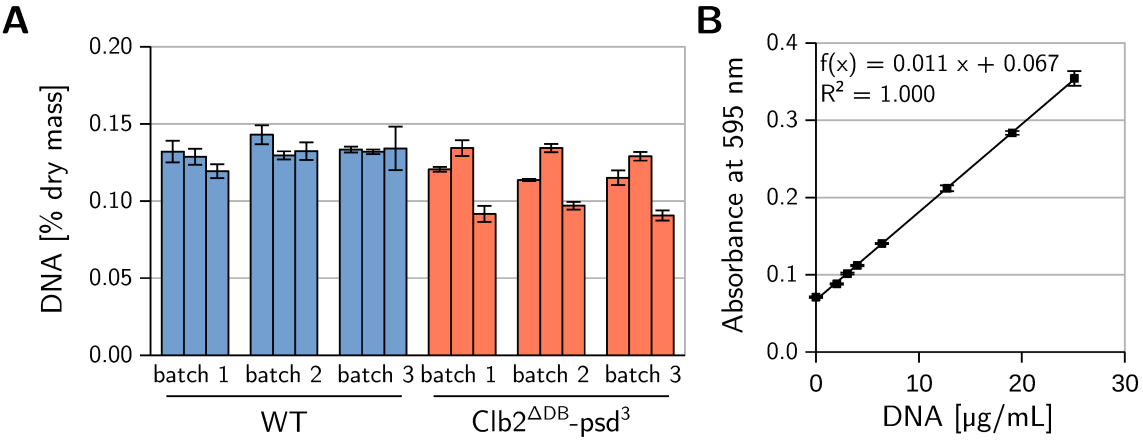

Figure 2.6: **A** Quantification of DNA content from dry mass of Clb2$^{\Delta DB}$-psd^3 cells cultured under restrictive growth conditions and corresponding WT cells. Error bars represent standard deviation of three measurements. **B** Exemplary linear regression of the absorption for DNA standards.

Cells of the Clb2$^{\Delta DB}$-psd^3 strain contained 0.11 % DNA with a standard deviation of 0.02 %. For corresponding WT cells DNA content was 0.13 $\pm$ 0.01 %. The p-value of a two-sided unpaired Student's t-test comparing biological triplicates of both strains was 0.012 representing a rather unclear differentiation of DNA content for both yeast strains.

2.1.6 Lipid Quantification

The extraction protocol for lipids from cellular material was implemented in glass ware because a significant amount of a characterized substance ($\approx 3\,\mathrm{mg}$) was obtained during test extractions using plastic tubes for blank samples. Applied to intact freeze dried cells the protocol yielded low and inconsistent results for lipid mass. In order to increase the extraction efficiency cells were lysed by glass beads or by lyticase treatment as described in section 4.1.7 prior to extraction. Microscope pictures of intact cells and cells lysed by glass beads and lyticase are shown in figure 2.7.

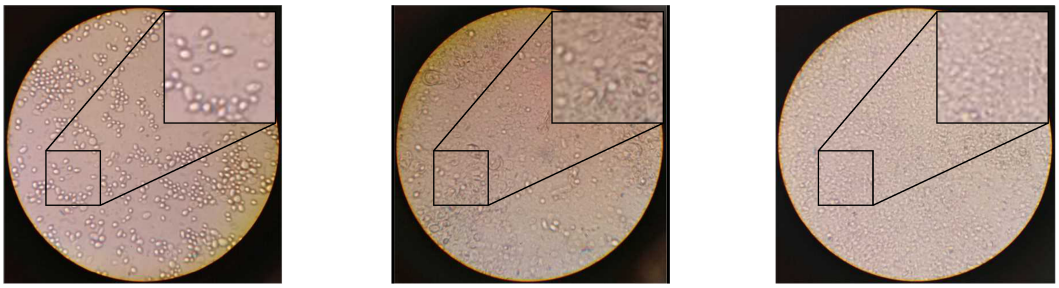

intact cells | cells lysed by glass beads | cells lysed by lyticase

Figure 2.7: Intact *S. cerevisiae* and cells lysed by glass beads and by lyticase treatment. A magnified section is visualized in each picture.

Remarkably, a significant proportions of cells still remained visibly intact after six rounds of glass bead treatment, retaining their well-defined shape and brightness. In contrast, cell debris after lyticase treatment was highly homogeneous revealing efficient cell lysis. In order to further examine the efficiency of the extraction protocol, *S. cerevisiae* producing the lipophilic orange compound β-carotene (ySH1 + pUDE269) and a control strain (ySH1) were extracted after and without prior lysis.

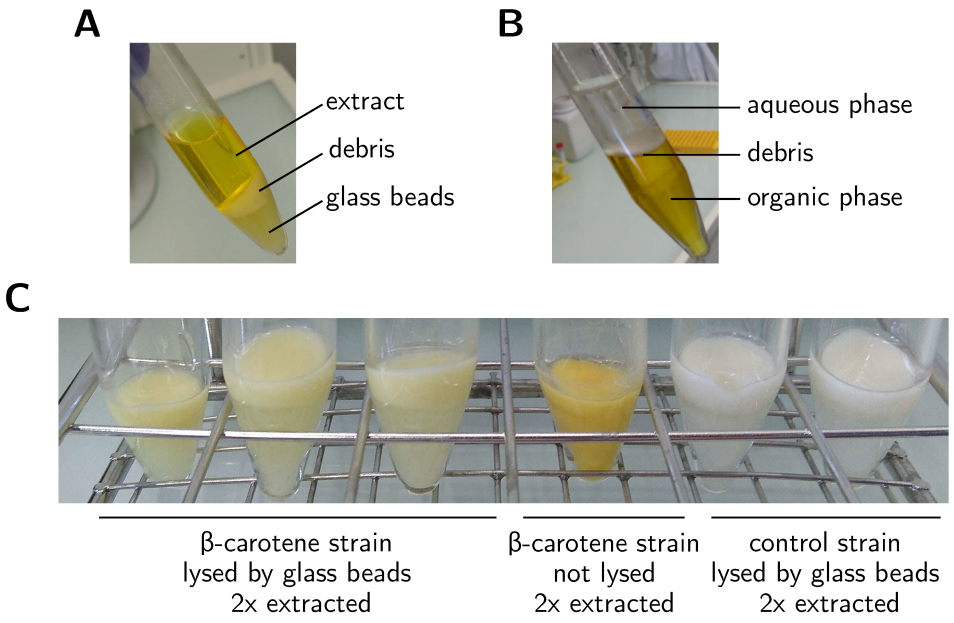

Figure 2.8: **A** Lipid extraction of the *S. cerevisiae* β-carotene strain lysed by glass beads. Picture of the first extraction, after the centrifugation step. **B** Lipid extraction of the *S. cerevisiae* β-carotene strain lysed by lyticase treatment. Picture of the first extraction, after phase separation and centrifugation. **C** Color comparison of *S. cerevisiae* pellets after two extraction cycles.

As visualized in figure 2.8, extraction of the lipophilic orange compound β-carotene was strongly improved by cell lysis with glass beads and the same should apply to other cellular lipophilic substances. Nevertheless the pellet remained slightly yellow after the second extraction and did not further decolorize after a third extraction. This observation reflects the observed intact cells after multiple cycles of cell lysis via glass beads described earlier. In contrast, cell debris resulting from lyticase treatment formed a colorless disc between hydrophilic and hydrophobic phase after phase separation, implying a complete extraction of lipophilic material. Based on this result, lyticase treatment was chosen as the lysis method for lipid quantification of Clb2$^{\Delta DB}$-psd^3 and corresponding WT cells.

On average Clb2$^{\Delta DB}$-psd^3 cells contained 7.6 % ± 0.4 % lipids. For WT cells, lipid content was determined as 6.4 ± 0.3 %. The result of a two-sided unpaired Student's t-test was $p = 0.016$. This p-value implies an unclear distinction of lipid content for both yeast strains and is influenced by the relative small sample size compared to the previous analyses.

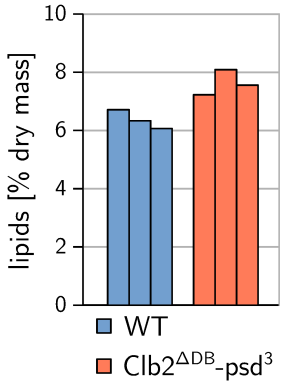

Figure 2.9: Quantification of lipid content from dry mass of Clb2$^{\Delta DB}$-psd^3 cells cultured under restrictive growth conditions and corresponding WT cells.

2.1.7 Summary of Biomass Analysis

As visualized in figure 2.10, overall biomass composition differs remarkably between both yeast strains. Clb2$^{\Delta DB}$-psd^3 cells contain more protein and RNA and less carbohydrates compared to WT cells. DNA and lipid contents of both strains are similar. For both strains a fraction cell dry mass of $\approx 20\,\%$ remained unassigned. In literature, in addition to the quantified compounds water (3.6 %), metals (2.5 %), inorganic phosphorus (1.5 %) and sulfate (0.5 %) contribute to cell dry mass.[64] Taking this into account, a biomass fraction of $> 10\,\%$ remains undetermined.

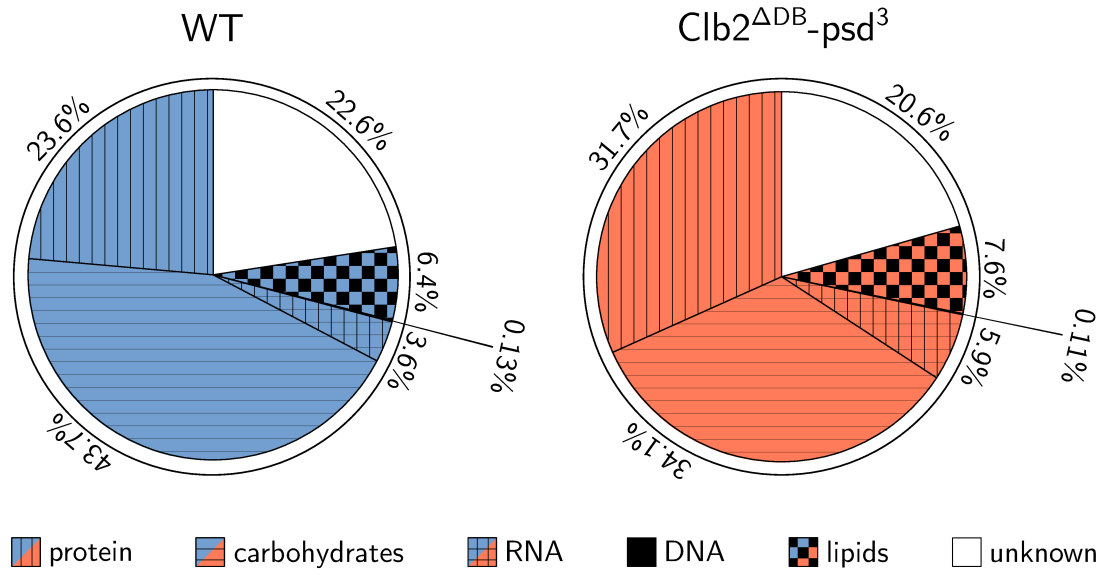

Figure 2.10: Summary of biomass composition for the Clb2$^{\Delta DB}$-psd^3 strain grown under restrictive conditions (blue) and corresponding WT cells (red).

The obtained biomass composition was used for the patent application "Verfahren zur Herstellung eines Pflanzeninhaltsstoffes durch optogenetische Kontrolle von Zellzyklusregulatoren" (EP4006164A1) registered within the MELICOMO project and as data basis for metabolic flux modeling, performed by the group of Prof. Dr. Zoran Nikoloski at the university of Potsdam. Furthermore, the established Biuret protocol contributed to the publication of Hepp *et al.*[46]

Table 2.1: Biomass composition and standard deviation of Clb2$^{\Delta DB}$-psd^3 cells cultured under restrictive growth condition and corresponding WT cells. Standard deviation of the unknown fraction corresponds to the sum of the standard deviations of the determined biomass fractions.

	WT	Clb2$^{\Delta DB}$-psd^3
protein	23.6 $\pm$ 1.2 %	31.7 $\pm$ 1.7 %
carbohydrates	43.7 $\pm$ 3.6 %	34.1 $\pm$ 2.3 %
RNA	3.6 $\pm$ 0.4 %	5.9 $\pm$ 0.6 %
DNA	0.13 $\pm$ 0.01 %	0.11 $\pm$ 0.02 %
lipids	6.4 $\pm$ 0.3 %	7.6 $\pm$ 0.4 %
unknown	22.6 $\pm$ 5.5 %	20.6 $\pm$ 5.0 %

2.1.7.1 Protein Quantification of *S. cerevisiae* Strains for Flux Modeling

In order to supply a robust data basis for the metabolic flux modeling performed by the group of Prof. Dr. Zoran Nikoloski, protein content was determined for Cdc48-psd^3, Clb2$^{\Delta DB}$-psd^3 and bPAC cells grown under permissive and restrictive condition and for corresponding WT strains. Cells were cultured as described in section 4.2.1 and freeze dried after the washing procedure. From the obtained cell pellets protein content was determined using the Biuret assay. Table 2.2 summarizes the results of the analysis.

Table 2.2: Protein content of the examined CCM strains grown under blue light conditions or in darkness under cultivation conditions of the proteomics experiment.

	darkness	blue light
SK1	18.8 ± 1.3 %	18.8 ± 1.3 %
bPAC	18.2 ± 0.1 %	20.9 ± 0.4 %
ESM356	22.0 ± 0.5 %	22.4 ± 0.3 %
Cdc48-psd^3	20.0 ± 0.3 %	20.0 ± 0.6 %
ESM356_Leu	19.8 ± 0.5 %	19.7 ± 0.4 %
Clb2$^{\Delta DB}$-psd^3	21.2 ± 0.5 %	20.0 ± 1.0 %

Results for protein quantification for cells grown under the conditions of the proteomics experiment were significantly lower compared to the results summarized by section 2.1.2. This is probably due to major differences in cultivation conditions of the cells. For the results shown by table 2.2 cultures of 50 mL were grown in TC flasks for 12 h under permissive conditions followed by 12 h under restrictive conditions. The results of section 2.1.2 were obtained for cultures grown for 3 h under permissive conditions followed by 24 h under restrictive conditions in 2 L in glass flasks.

2.2 Proteomics of Light-Controlled *S. cerevisiae*

In previous experiments, cell cycle mutants (CCMs) showed an increased production of valuable target molecules in comparison to the corresponding wild type (WT). Here, remarkable differences in product yield between restrictive and permissive light conditions were observed.[92,100] The increased product yield of CCM cells grown under restrictive conditions could be assigned to an increased energy availability for the production of secondary metabolites due to the cell cycle arrest. Furthermore, shifts in the proteome of CCM cells towards enzymes involved in the production of target molecules could explain the increased product yields.

In order to investigate into reasons for the higher productivity of restricted CCM cells on the proteome level, a series of proteomics experiments was performed for the Cdc48-psd^3, Clb2$^{\Delta DB}$-psd^3 and bPAC strain and corresponding WT strains as described in section 4.2. Culture ODs and protein content determined from dry mass are summarized in tables 5.14 and 5.15 in the appendix section. This data was later used together with results of the proteomics experiment for modeling calculations, which were performed by the group of Prof. Dr. Zoran Nikoloski at the university of Potsdam.

Within the proteomics experiment a total number of 24 LC-MS/MS measurements were performed for each of the three CCM strains. Here, each 2 h MS/MS measurement generated about 3 GB of raw data using the timsTOF Pro instrument and was analyzed using the *PEAKS* software. Exemplary specified for the bPAC strain and the corresponding WT, the dataset contained $\approx$ 225 million MS spectra and $\approx$ 4 million MS/MS spectra, which were assigned to $\approx$ 2 million *de novo* peptide spectra in the *de novo* analysis step of the software. During *PEAKS* analysis $\approx$ 54.000 peptides were mapped to the database and were assigned to 3546 of the 5441 protein sequences, which were provided by the database. Subsequently, in the label-free quantification (LFQ) step of the analysis, peptides were filtered for quality and average area according to guidelines of the software manufacturer.[3] Finally LFQ results were exported for 1019 proteins meeting the LFQ filter criteria listed in table 4.6 and plotted as heatmaps.

Results for the analysis of the proteomics datasets for all examined CCM yeast strains are summarized by table 2.3. LFQ results were generated for the Cdc48-psd^3 and Clb2$^{\Delta DB}$-psd^3 strains with identical filter parameters. For bPAC stricter filter criteria were applied due to a higher data quality.

Table 2.3: Summary of proteomics data. Assigned proteins are denoted relative to the number of proteins provided by the corresponding FASTA database.

analyzed CCM strain	mapped peptides	assigned proteins	filtered proteins
Cdc48-psd^3	78.001	4388/5924	1962
Clb2$^{\Delta DB}$-psd^3	83.332	4387/5923	2152
bPAC	54.314	3546/5441	1018

LFQ results were analyzed in a pairwise manner comparing two sample groups (e.g. CCM cultured under restricted growth condition with the corresponding WT) and volcano plots were generated for the resulting abundance ratios. From the comparisons, proteins were identified showing a significant abundance difference (p-value of the Student's t-test < 0.01 and mean abundance difference $> 10\,\%$). These differentially abundant proteins (DAPs) were further analyzed and used as input for GO-term enrichment analyses to reveal affected cellular pathways, functions, processes and components in the comparison of both sample groups.

2.2.1 Heatmaps of Relative Protein Abundance

Within the analysis workflow of proteomics data, large heatmaps were used to visualize protein abundance of biological and technical replicates in order to provide an overview of the overall outcome of the experiment. Heatmaps include abundance of all proteins meeting the quality parameters of the *PEAKS* analysis and were automatically generated in the LFQ step by the *PEAKS* software. Nevertheless heatmaps generated by *PEAKS* allow only the export to .png format, hindering customization and further analysis. In order to solve this problem, within this work R scripts were established to generate heatmaps from exported raw protein abundances.

Heatmaps were generated for all three CCM and corresponding WT strains cultured under the respective restrictive and permissive light condition of the CCM strain. Each heatmap summarizes a total of 24 measurements (four sample groups, grown as biological triplicates, measured in duplicate). In addition to the heatmaps visualizing all 24 data sets, condensed heatmaps were created from averaged abundances of technical duplicates.

2.2.1.1 Heatmaps – Cdc48-psd^3

Two heatmaps summarizing the outcome of the proteomics experiment for the Cdc48-psd^3 strain are shown in figure 2.11.

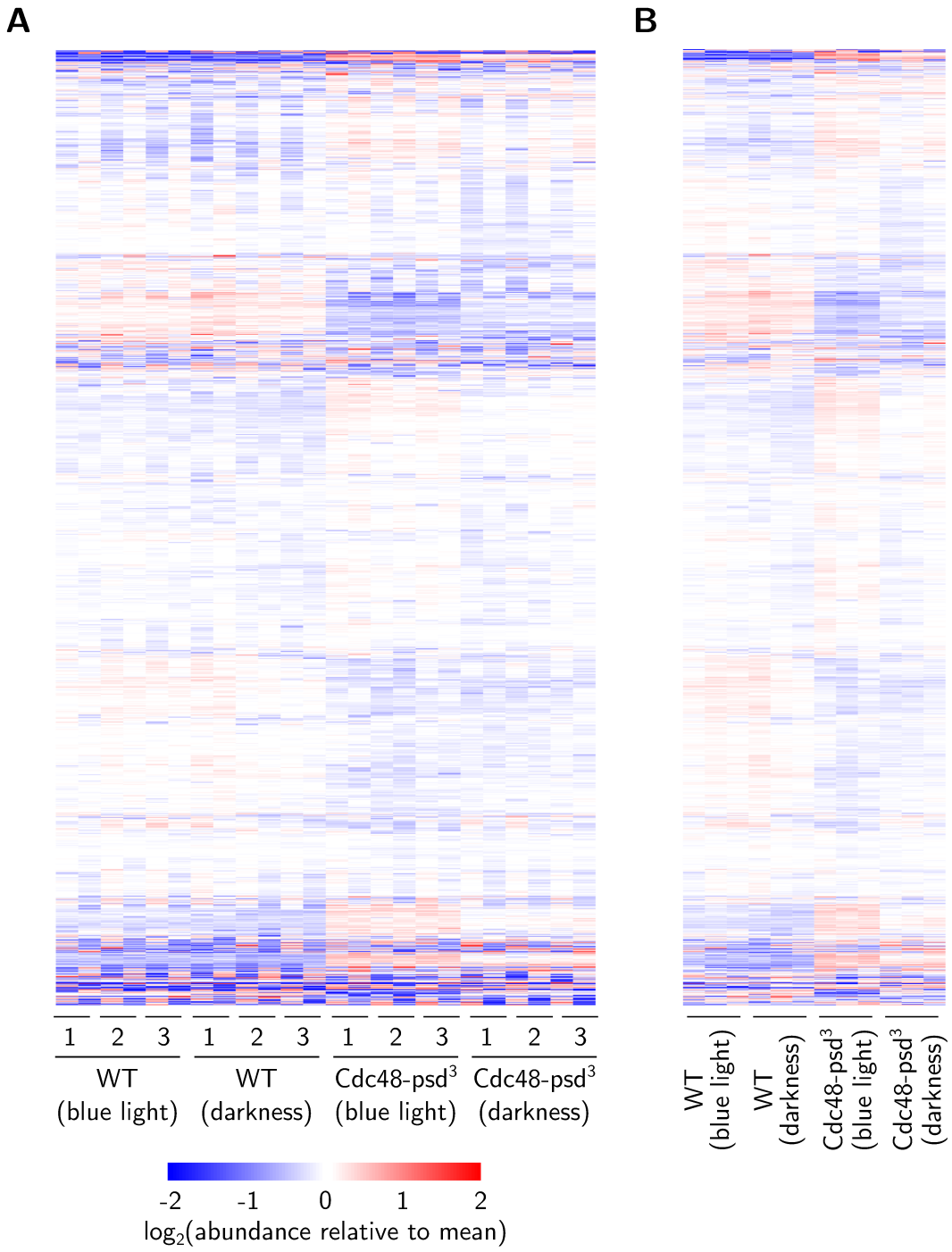

Figure 2.11: Heatmaps generated from protein abundances for the Cdc48-psd^3 strain and corresponding WT cells. Cultures were incubated under 30 $\frac{\mu mol}{m^2 \cdot s}$ blue light (restrictive condition) and in darkness (permissive condition). **A** Visualization of all obtained data sets including technical duplicates for each biological triplicate. **B** Visualization of proteomics data with calculated mean protein abundance for technical duplicates.

The generated heatmaps illustrate well the influence of blue light on the proteome of Cdc48-psd^3 cells. Here, large sections of the heatmaps were impacted in the comparison of Cdc48-psd^3 grown under restrictive (30 $\frac{\mu mol}{m^2 \cdot s}$ blue light) and permissive light conditions (darkness), thereby exhibiting clear differences in protein abundance. Between Cdc48-psd^3 grown under restricted and permissive condition, the abundance pattern of Cdc48-psd^3 cultured under permissive growth conditions related stronger to the abundance pattern of the WT strain. Hence Cdc48-psd^3 grown under permissive condition appeared to be more WT-like than restricted Cdc48-psd^3 on the proteome level. This observation will be further analyzed in section 2.2.2.1. Lacking optogenetic modifications the WT did not exhibit obvious differences between the two illumination conditions. Noticeable in figure 2.11A is distinct pattern of abundance ratios effecting every duplicate measurement with varying impact on different proteins. This behavior is probably due to the very long sample list, which meant that each technical replicate was measured four days after the first replicate. In the meantime, apparently instrumental or sample conditions changed causing the pattern structure in the heatmap. These changes in abundance are remarkably similar within the biological replicates and the heatmap in figure 2.11B (which is based on mean abundance of the technical duplicates) shows a uniform abundance pattern for biological replicates. Since the mean values of technical replicates are used for downstream analyses, the data generated for the Cdc48-psd^3 strain should provide a solid basis.

2.2.1.2 Heatmaps – Clb2$^{\Delta DB}$-psd^3

Heatmaps generated for the Clb2$^{\Delta DB}$-psd^3 strain and the corresponding WT strain background visualized in figure 2.12 are remarkably pale due to a overall similar protein abundance for most proteins over the entire analyzed sample set. Both heatmaps do not show an obvious visual pattern in order to distinguish between Clb2$^{\Delta DB}$-psd^3 grown in darkness (restrictive growth condition) and under 30 $\frac{\mu mol}{m^2 \cdot s}$ blue light (permissive growth condition). Furthermore, only slight differences on the proteome level are implied in the comparison between Clb2$^{\Delta DB}$-psd^3 and the WT, visible in the top and bottom third of the heatmap. The distinct stripe pattern described for the proteomics experiment for Cdc48-psd^3 is also present in the heatmap of figure 2.12A and appears to be a little more prominent due to missing colorful abundance clusters in the center of the heatmaps. Final conclusions about the outcome of the proteomics experiment for the Clb2$^{\Delta DB}$-psd^3 strain will be drawn after the evaluation of protein abundances below.

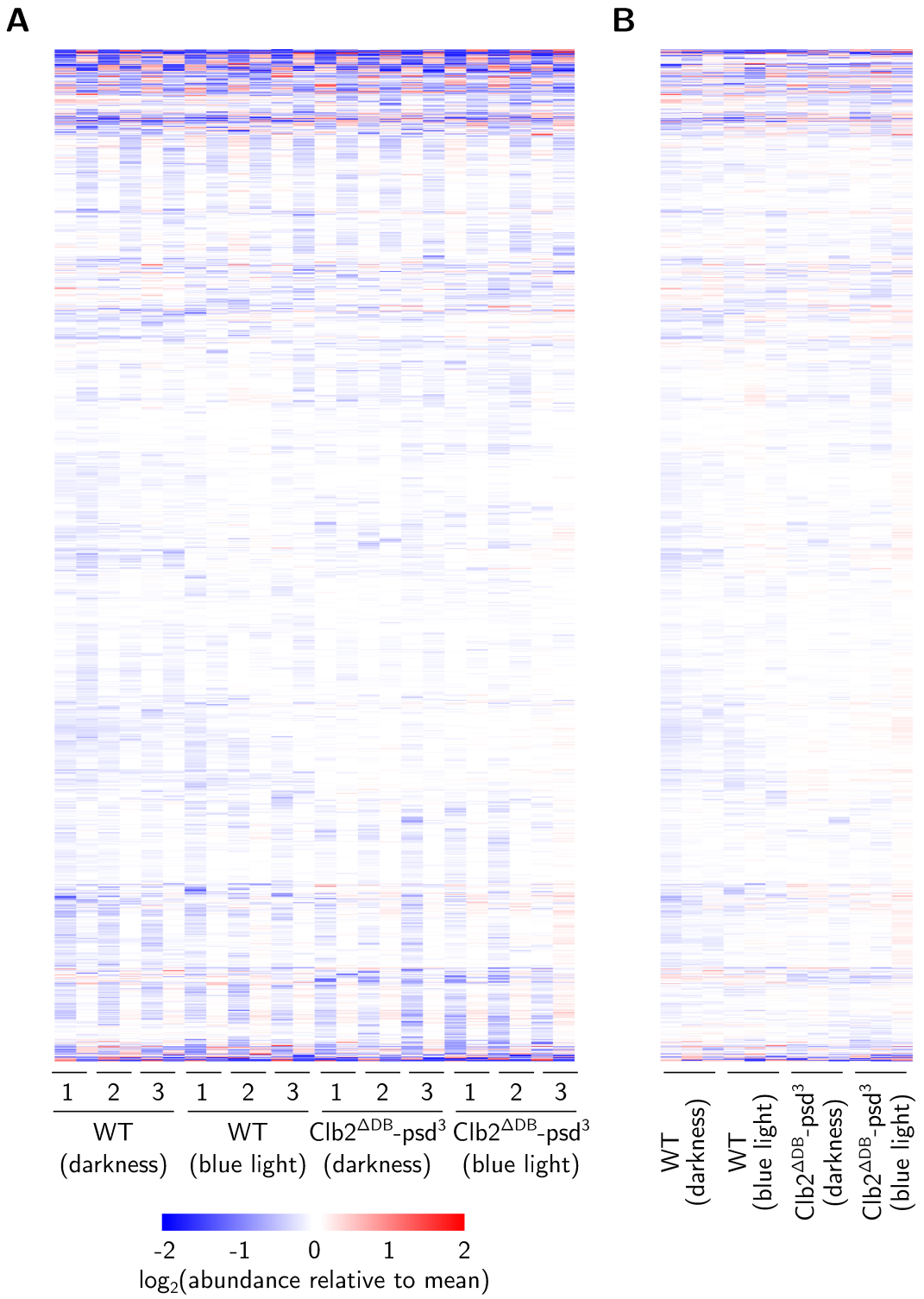

Figure 2.12: Heatmaps generated from protein abundances for the Clb2$^{\Delta DB}$-psd^3 strain and corresponding WT cells. Cultures were incubated in darkness (restrictive condition) and under 30 $\frac{\mu mol}{m^2 \cdot s}$ blue light (permissive condition). **A** Visualization of all obtained data sets including technical duplicates for each biological triplicate. **B** Visualization of proteomics data with calculated mean protein abundance for technical duplicates.

2.2.1.3 Heatmaps – bPAC

The heatmaps in figure 2.13 show great influence of blue light on the proteome for the light-controlled bPAC strain. Almost all sections of the heatmaps were impacted in the comparison of bPAC grown under permissive (1 $\frac{\mu mol}{m^2 \cdot s}$ blue light) and restrictive light condition (darkness), showing impressive differences in protein abundance. For the WT strain protein abundances were unaffected by the light condition. Furthermore, the abundance pattern for bPAC cultured under both light conditions differed clearly in comparison to the WT strain for almost the entire heatmap. The stripe pattern described earlier is also visible in figure 2.13A but mean abundance values seem to be unaffected as figure 2.13B shows a colorful uniform abundance pattern between biological replicates. Furthermore, both heatmaps are smaller and appear cleaner in comparison to Cdc48-psd^3 and Clb2$^{\Delta DB}$-psd^3, which is because different filter settings were used in the *PEAKS* export for the bPAC strain. Hence, data obtained for the bPAC strain should provide a solid data basis for a detailed investigation into changes on the proteome level.

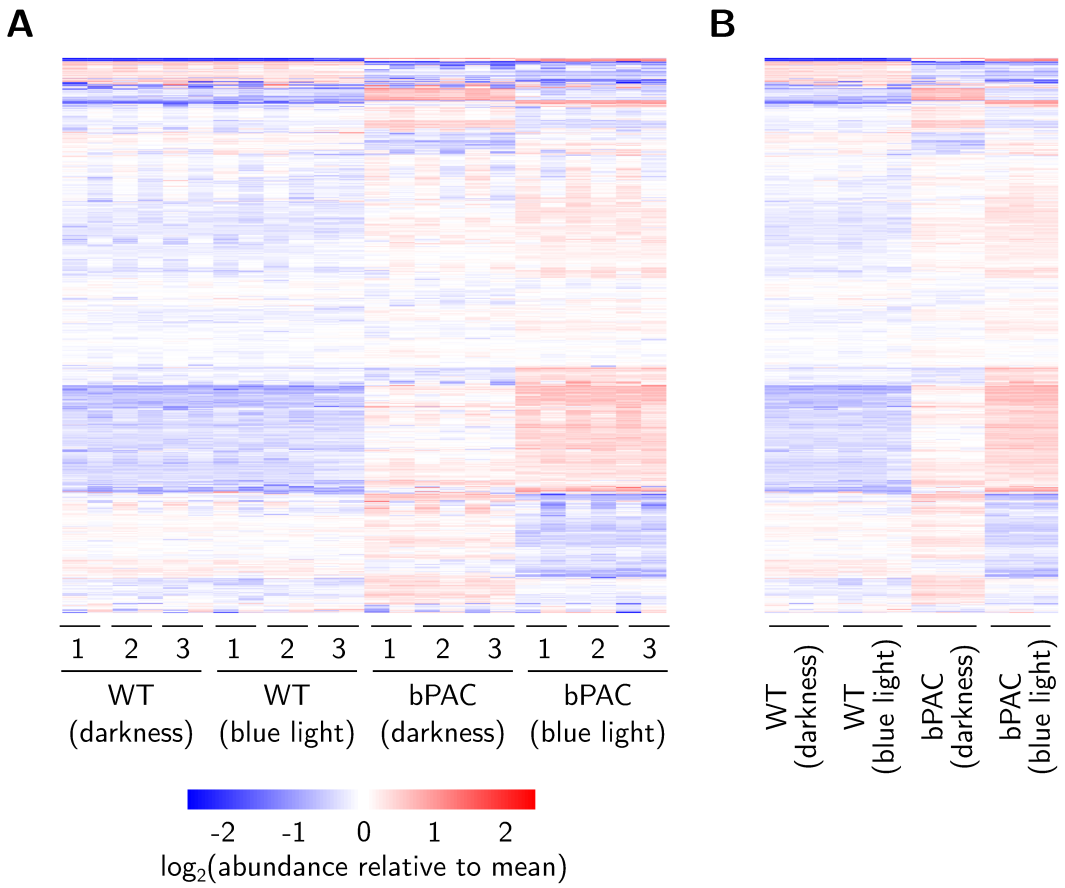

Figure 2.13: Heatmaps generated from protein abundances for the bPAC strain and corresponding WT cells. Cultures were incubated in darkness (restrictive condition) and under 1 $\frac{\mu mol}{m^2 \cdot s}$ blue light (permissive condition). **A** Visualization of all obtained data sets including technical duplicates for each biological triplicate. **B** Visualization of proteomics data with calculated mean protein abundance for technical duplicates.

2.2.2 Volcano Plots and Differentially Abundant Proteins

Volcano plots are scatter-plots used in proteomics to visualize fold changes and allow significance filtering for two related sample groups. Within this work volcano plots were generated both for the comparison of the growth-restricted CCM strain and the corresponding WT strain as well as for the growth-restricted CCM and the CCM strain cultured under permissive conditions. For both comparisons a positive $\log_2$(ratio) refers to a higher protein abundance for the growth-restricted CCM. In the plots the threshold for differentially abundant proteins (DAPs) ($p < 0.01$, mean abundance difference $> 10\,\%$) is visualized. Highlighted in the plots are proteins involved in pathways for precursor generation of gibberellin A_4 (GA_4), β-carotene and cordycepin, which are target molecules produced by the light-controlled production strains within the MELICOMO project. The synthesis of gibberellins and β-carotene branches off the ergosterol biosynthesis superpathway after the mevalonate pathway from farnesyl pyrophosphate (FPP) via geranyl geranyl pyrophosphate (GGPP), as visualized in figure 1.1 of the introduction section. In the volcano plots, enzymes upstream of GGPP and proteins downstream of FPP involved in the biosynthesis of ergosterol are highlighted. Furthermore, the repressible vacuolar alkaline phosphatase Pho8 is highlighted in the volcano plots, whose depletion was found to increase the availability of the cordycepin precursor 3'AMP.[52] The full list of highlighted proteins and plotted data is summarized in tables 5.16 to 5.18 in the appendix section.
Furthermore, obtained DAPs were used for Venn diagrams in order to visualize the overlap of different comparisons. Here, DAPs were excluded from the cross section of the Venn diagram in case of an opposite abundance profile (e.g exclusion of DAP with higher abundance in the comparison to the WT and lower abundance in the comparison to the permissive condition).

2.2.2.1 Volcano Plots and DAP Analysis – Cdc48-psd^3

For the Cdc48-psd^3 proteomics analysis 1962 proteins were meeting the export criteria of the *PEAKS* software. Regarding the comparison of Cdc48-psd^3 grown under restrictive light conditions and the WT strain 504 DAPs were identified. Here, remarkably the acetyl-CoA synthetase Acs2 exhibited twice the abundance for growth-restricted Cdc48-psd^3 compared to the WT strain. Additionally, the proteins Erg13 and Hmg1 of the mevalonate pathway were higher abundant in Cdc48-psd^3 cells. Furthermore, the proteins Erg9, Erg1, Erg11, Erg25 and Erg3 downstream of FPP in the ergosterol biosynthesis superpathway were among the DAPs with higher abundance for the Cdc48-psd^3 strain. Noteworthy, these proteins appear in the region of the volcano plot with high -$\log_{10}$(p) values and $\log_2$(ratio). DAPs lower abundant in Cdc48-psd^3 cells were Erg26, an enzyme downstream of FPP, and the protein Pho8 involved in the depletion of 3'AMP. In the comparison of Cdc48-psd^3 grown under restrictive and permissive condition only

194 DAPs were identified. Here, Acs2 as well as Erg11, Erg25, Erg3 and Pho8 were higher abundant in Cdc48-psd^3 grown under restrictive conditions. Volcano plots for both comparisons are shown in figure 2.14 and plotted data of the highlighted proteins is provided in table 5.16 in the appendix section.

The comparison between Cdc48-psd^3 grown under permissive conditions and the WT strain was not analyzed into great detail. Nevertheless, 328 DAPs were identified for this comparison, which were significantly less DAPs than in the comparison of Cdc48-psd^3 grown under restrictive conditions and the WT strain. This observation matches the analysis of the heatmap in section 2.11. Here, the abundance pattern appeared to be more WT-like for the permissive light condition compared to Cdc48-psd^3 grown under restricted conditions.

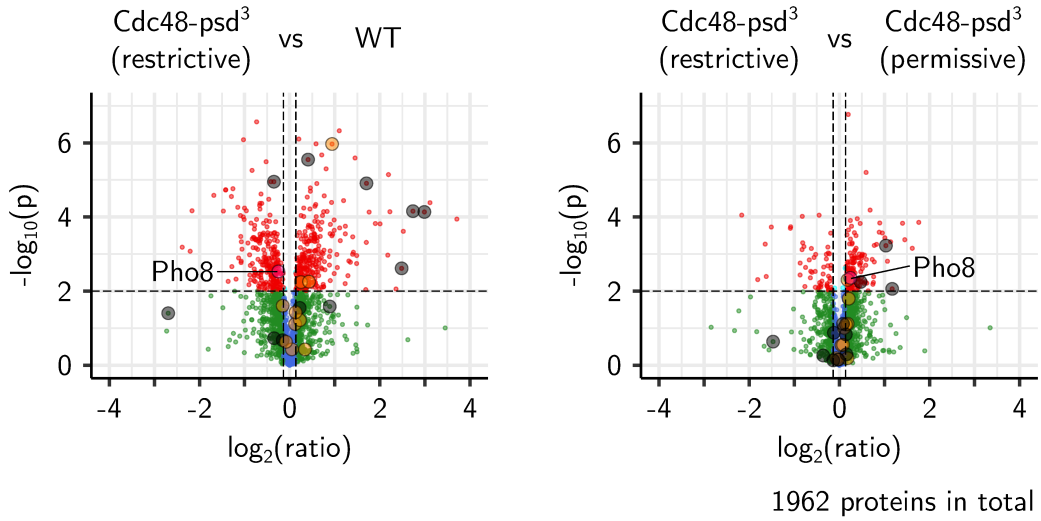

Figure 2.14: Volcano plots of proteomics data for the Cdc48-psd^3 strain. Differentially abundant proteins (DAPs) depicted in red are meeting the filter criteria of $p < 0.01$ and mean abundance difference of $> 10\,\%$. Enzymes upstream of GGPP involved in precursor generation for gibberellic acid and β-carotene are highlighted in orange, enzymes downstream of FPP towards ergosterol synthesis are emphasized in black. Pho8 which is involved in the depletion of the cordycepin precursor 3'AMP is highlighted in pink. **A** Comparison of the Cdc48-psd^3 strain grown under restrictive conditions and the corresponding WT strain. **B** Comparison of the Cdc48-psd^3 strain grown under restrictive and permissive conditions.

As visualized in figure 2.15 the two comparisons for the Cdc48-psd^3 strain shared 135 DAPs. Hence, most of the DAPs identified in the comparison of restrictive and permissive growth condition were also DAPs in the comparison to the WT strain.

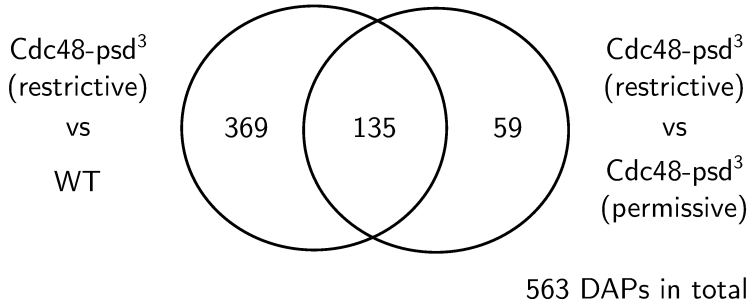

Figure 2.15: Venn diagram for DAPs identified for the Cdc48-psd^3 strain.

2.2.2.2 Volcano Plots and DAP Analysis – Clb2$^{\Delta DB}$-psd^3

For Clb2$^{\Delta DB}$-psd^3, data of 2152 proteins met the required quality criteria and corresponding data was exported for further analysis. In the comparison of Clb2$^{\Delta DB}$-psd^3 grown under restricted conditions and the WT only 107 DAPs were identified. Among these DAPs no protein was part of the mevalonate pathway, ergosterol biosynthesis superpathway or involved in the precursor generation of cordycepin.
For the comparison of Clb2$^{\Delta DB}$-psd^3 cultured under restrictive and permissive growth conditions 51 proteins were identified as DAPs. Among these proteins Erg1 was slightly higher abundant under permissive conditions, whereas Erg3 was slightly higher abundant under restrictive conditions. Both proteins are part of biosynthesis of ergosterol downstream of FPP. A summary of all exported proteins for both comparison is provided by figure 2.16 and the highlighted proteins are summarized in table 5.17.
In the comparison between Clb2$^{\Delta DB}$-psd^3 grown under permissive conditions and the WT strain a total number of 91 DAPs were identified. Hence, the light condition did not seem to an impact on the DAP count in the comparison of Clb2$^{\Delta DB}$-psd^3 to the WT, as in both comparisons $\approx 5\,\%$ of the exported proteins were matching the DAP criteria.

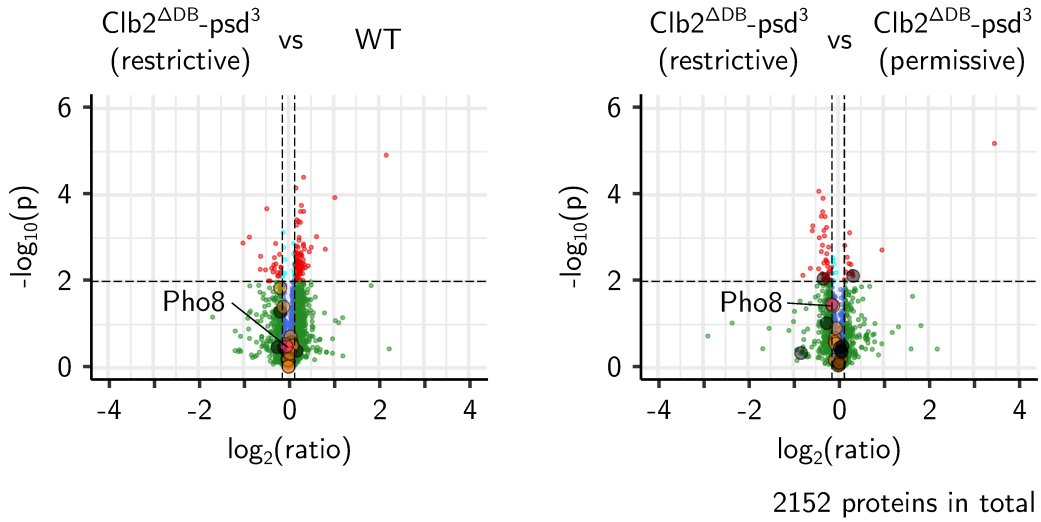

Figure 2.16: Volcano plots of proteomics data for the Clb2$^{\Delta DB}$-psd^3 strain. Differentially abundant proteins (DAPs) depicted in red are meeting the filter criteria of $p < 0.01$ and mean abundance difference of $> 10\,\%$. Enzymes upstream of GGPP involved in precursor generation for gibberellic acid and β-carotene are highlighted in orange, enzymes downstream of FPP towards ergosterol synthesis are emphasized in black. Pho8, which is involved in the depletion of the cordycepin precursor 3'AMP, is highlighted in pink. **A** Comparison of the Clb2$^{\Delta DB}$-psd^3 strain grown under restrictive conditions and the corresponding WT strain. **B** Comparison of the Clb2$^{\Delta DB}$-psd^3 strain grown under restrictive and permissive conditions.

As visualized by the Venn diagram in figure 2.17, DAPs identified by the two abundance comparisons for the Clb2$^{\Delta DB}$-psd^3 strain shown in figure 2.16 were exclusive for each comparison.

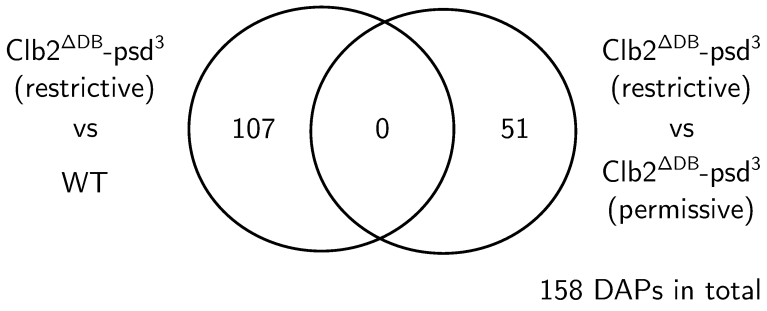

Figure 2.17: Venn diagram for DAPs identified for the Clb2$^{\Delta DB}$-psd^3 strain.

2.2.2.3 Volcano Plots and DAP Analysis – bPAC

For the proteomics analysis of the bPAC strain, protein abundances for 1018 proteins were exported using the *PEAKS* software. In the comparison of restricted bPAC and the WT 506 proteins were identified as DAPs. Hence, abundances of about half of the examined proteins were found to be significantly different between the two strains. For this comparison Acs1 and Erg13 upstream of GGPP were higher abundant for the restricted bPAC strain. Here, Acs1 stands out with a six-fold increased abundance ($\log_2(6) \approx 2.6$), which was among the highest abundance differences observed within the experiment. Additionally, in the biosynthesis pathway downstream of FPP towards ergosterol biosynthesis Erg9 abundance was found to be increased for restricted bPAC compared to the WT strain. For the WT strain Erg20 and Erg26 were found to be higher abundant.
In the comparison of the bPAC strain grown under restrictive and permissive conditions 527 DAPs were identified. Highly abundant in the restricted bPAC strain was Acs1, which was also highly abundant in the comparison to WT cells as mentioned above. Furthermore, Pho8 involved in the precursor depletion of cordycepin was among the DAPs and of increased abundance for restricted bPAC cells. For the bPAC strain grown under permissive conditions Acs2, Erg19 and Erg20 upstream of FPP and Erg11, Erg26 and Erg2 downstream of FPP were found to be of higher abundance. Figure 2.18 shows volcano plots for the exported proteins of both comparisons. Data of highlighted proteins in both plots is summarized in table 5.18 in the appendix section.
In the comparison between bPAC grown under permissive conditions and the WT strain 625 DAPs were identified, thereby exceeding the number of DAPs found for the comparison of bPAC grown under restrictive conditions and the WT strain. This observation underlines the impact of Cyr1 substitution by bPAC for this strain and the broad impact of light dependent cAMP production on the proteome.

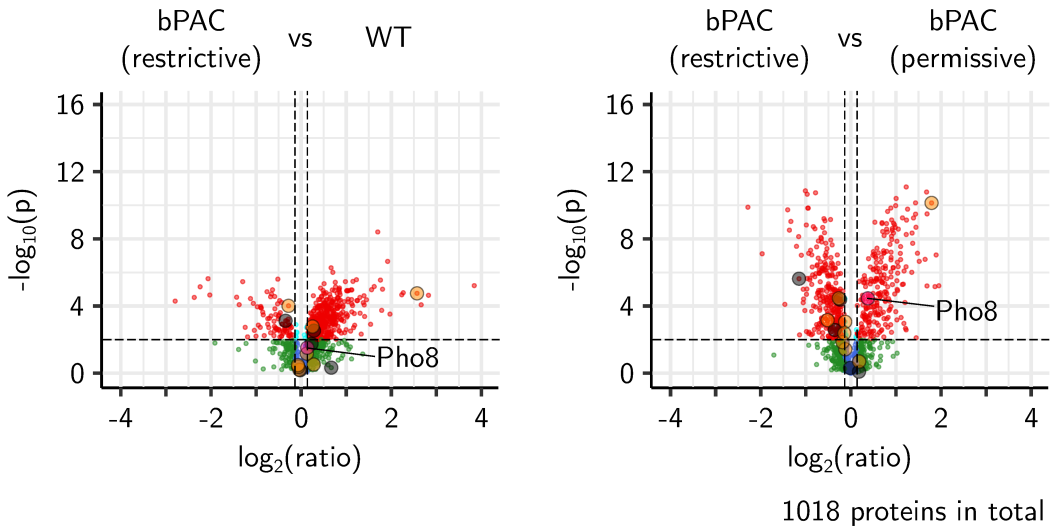

Figure 2.18: Volcano plots of proteomics data for the bPAC strain. Differentially abundant proteins (DAPs) depicted in red are meeting the filter criteria of $p < 0.01$ and mean abundance difference of $> 10\,\%$. Enzymes upstream of GGPP involved in precursor generation for gibberellic acid and β-carotene are highlighted in orange, enzymes downstream of FPP towards ergosterol synthesis are emphasized in black. Pho8, which is involved in the depletion of the cordycepin precursor 3'AMP, is highlighted in pink. **A** Comparison of the bPAC strain grown under restrictive conditions and the corresponding WT strain. **B** Comparison of the bPAC strain grown under restrictive and permissive conditions.

For the bPAC strain, 159 DAPs were shared between the two comparisons. The corresponding Venn diagram is shown in figure 2.19.

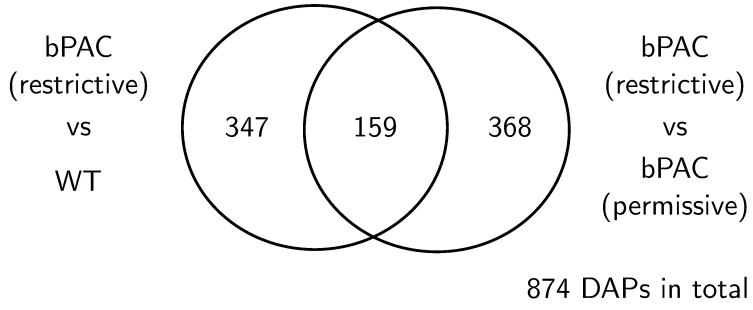

Figure 2.19: Venn diagram for DAPs identified for the bPAC strain.

2.2.2.4 Volcano Plots and DAP Analysis – Summary

For the Cdc48-psd^3 and bPAC strains a high number of DAPs were identified in the comparisons between restricted CCM and WT cell and between restricted CCM and permissive CCM cells respectively. For the Clb2$^{\Delta DB}$-psd^3 strain the overall amount of DAPs was significantly lower.

Many enzymes of the ergosterol biosynthesis superpathway were found with higher abun-

dance for growth-restricted Cdc48-psd^3 cells in the comparisons to the WT strain and to Cdc48-psd^3 cells grown under permissive conditions. This observation is important because the biosynthetic pathways for GA_4 and β-carotene branch off this pathway. For the Clb2$^{\Delta DB}$-psd^3 strain a total of only two enzymes of the ergosterol biosynthesis superpathway were identified as DAPs. Here, one protein was higher abundant and the other was lower abundant for growth-restricted Clb2$^{\Delta DB}$-psd^3 in comparison to Clb2$^{\Delta DB}$-psd^3 grown under permissive condition. In regard to the bPAC strain, identified DAPs of the superpathway were distributed evenly between high and low abundant for growth-restricted bPAC cells in the comparison of the growth-restricted bPAC strain to the WT strain. In the comparison of bPAC cultured under restrictive and permissive light condition more of these DAPs were found to be low abundant than high abundant for bPAC grown under restrictive conditions. Additionally, Acs2 for the Cdc48-psd^3 strain and Acs1 for the bPAC strain were found to be higher abundant for the restricted CCM both in the comparisons between restricted CCM and WT and in the comparisons of CCM grown under restrictive and permissive condition. The two acetyl-CoA synthetase isoforms provide the ergosterol biosynthesis superpathway with the initial precursor acetyl-CoA.
Furthermore, Pho8, involved in the depletion of the cordycepin precursor 3'AMP, was among the DAPs for the Cdc48-psd^3 strain. In the comparison of Cdc48-psd^3 cells grown under restrictive conditions to the WT strain, Pho8 was found to be less abundant for Cdc48-psd^3 cells, thereby potentially increasing the availability of 3'AMP for cordycepin synthesis. However, in the comparison of the Cdc48-psd^3 strain cultured under restrictive and permissive growth conditions, Pho8 was higher abundant for growth-restricted Cdc48-psd^3 cells. In the comparison of bPAC cells cultured under restrictive and permissive growth condition, Pho8 was found to be higher abundant for the growth-restricted bPAC strain.
To examine the distribution of protein ratios in the volcano plots, the average fold changes of protein abundance were calculated. Here, reciprocal values were calculated for ratios less than 1 before averaging. The average fold changes of protein abundance for all identified proteins and the total number of identified DAPs for all CCM strains examined are summarized in table 2.4.

Table 2.4: Identified DAPs for different CCM strains relative to the restricted condition of the CCM strain and average fold change of protein abundance in pairwise comparisons.

	DAPs		
comparison	high abundant	low abundant	average fold change
Cdc48-psd^3(restrictive) WT	271	233	1.25
Cdc48-psd^3(restrictive) Cdc48-psd^3(permissive)	138	56	1.18
Clb2$^{\Delta DB}$-psd^3(restrictive) WT	84	23	1.12
Clb2$^{\Delta DB}$-psd^3(restrictive) Clb2$^{\Delta DB}$-psd^3(permissive)	13	38	1.10
bPAC (restrictive) WT	420	86	1.41
bPAC (restrictive) bPAC (permissive)	237	290	1.37

As shown in table 2.4, average fold changes of protein ratios were the highest for the bPAC strain, followed by the Cdc48-psd^3 strain. For the Clb2$^{\Delta DB}$-psd^3 strain, the lowest average fold changes were calculated. For each yeast strain, the average fold change in protein ratios was similar between the two comparisons made, but slightly higher for the comparison between restrictive CCM and WT strain than for the comparison between restrictive and permissive growth condition.

In order to investigate into similarities between the different CCM strains Venn diagrams were generated comparing DAPs obtained in the comparison to the WT strain and between restrictive and permissive growth condition.

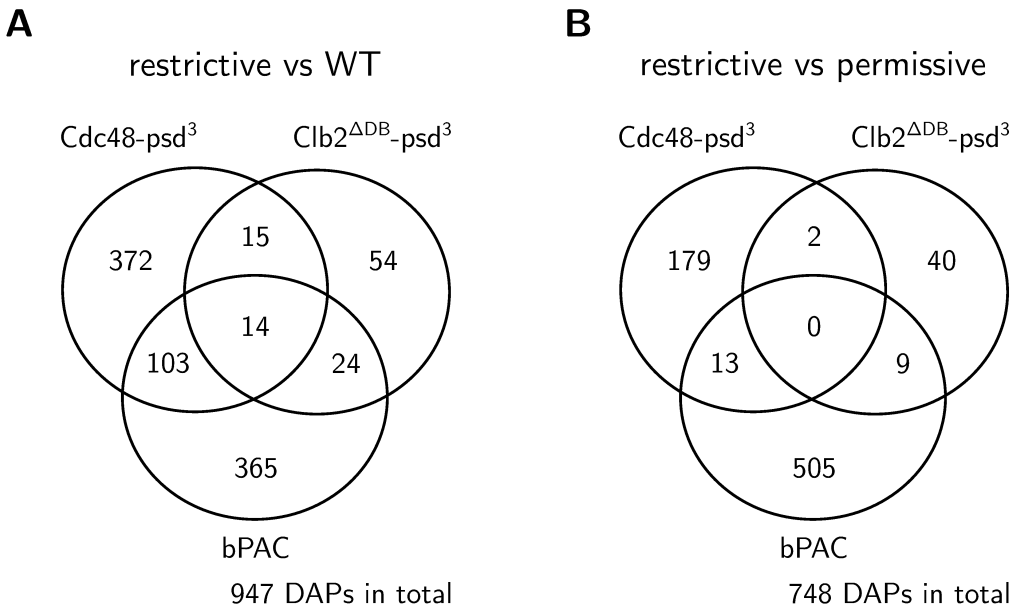

Figure 2.20: Overlapping DAPs for different CCM strains. **A** DAPs identified in comparisons of CCM strains grown under restrictive conditions and corresponding WT strains. **B** DAPs identified in comparisons of CCM strains grown under restrictive and permissive condition.

In the comparison of CCM strains grown under restrictive conditions and the WT strains, for the Cdc48-psd^3 strain $\approx 1/4$ of the identified DAPs were overlapping with the DAPs of the other strainS. Furthermore, $\approx 1/4$ of the DAPs for the bPAC strain and $\approx 1/2$ of the DAPs for the Clb2$^{\Delta DB}$-psd^3 strain were overlapping in this comparison. A total of 14 proteins were overlapping for all CCM strains, and many of these were related to ribosomal processes and translation. Interestingly Ubx1 was also among these DAPs and was found to be higher abundant for each growth-restricted CCM in comparison to the WT strain. Ubx1 is involved in Cdc48-dependent protein degradation and was found to interact with Cdc48. Furthermore, *UBX1* deletion mutants were defective in degradation of an ubiquitylated model substrate.[93] Additionally, Pfk1, the alpha subunit of the phosphofructokinase, was found to be lower abundant for every growth-restricted CCM strain in comparison to the WT strain. This observation was also made for the growth-restricted bPAC strain in comparison to the permissive growth condition. Mutations of *PFK1* and the gene for the beta subunit of the phosphofructokinase *PFK2* were found to inhibit glucose induction of *CLN3* (G1/S-specific cyclin Cg13), *BCK2* (bypass of kinase C protein Bck2) and *CDC28* (cyclin-dependent kinase Cdk1).[77] These genes need to be expressed in order to progress in the cell cycle from G1 to S phase. Among the DAPs shared only between the Cdc48-psd^3 and the Clb2$^{\Delta DB}$-psd^3 strains the ubiquitin-conjugating enzyme Ubc1 was found to be higher abundant for both growth-restricted CCM strains compared to the WT strain. Ubc1 plays a role in ER-associated protein degradation (ERAD). For the Cdc48-psd^3 and the bPAC strains, as before mentioned, Erg13 and Erg9 were higher abundant and Erg26 was lower abundant in the

comparison of the respective CCM strain grown under restrictive conditions and the WT strain. Furthermore, for the Cdc48-psd^3 and the bPAC strain the cyclin-dependent kinase Cdk1 and the fumarase Fum1 of the tricarboxylic acid (TCA) cycle were found to be higher abundant in comparison to the WT strain. Nevertheless, in the comparison of bPAC cells cultured under restrictive and permissive conditions, Cdk1 was found to be lower abundant for the growth-restricted bPAC strain. Overlapping DAPs between the Clb2$^{\Delta DB}$-psd^3 and the bPAC strain in comparison to the WT strain were strongly related to translation processes and were found to be of higher abundance for the WT strain compared to the restricted CCM strains.

The identified DAPs for the analysis of CCM strains grown under restrictive and permissive conditions showed only a small number of overlaps. As visualized by the Venn diagram in figure 2.20, no common DAPs between the analyses of all three CCM strains were identified. Nevertheless, as already mentioned above, Erg3 was higher abundant under restrictive conditions for the Cdc48-psd^3 and Clb2$^{\Delta DB}$-psd^3 strain. In the comparison of DAPs for the Cdc48-psd^3 and bPAC strain Ubx1 was higher abundant for cells grown under restrictive conditions. This finding matches the observation made for the comparison of restricted cells to the WT strain, where Ubx1 was found with higher abundance for both CCM strains cultured under restrictive growth conditions. Additionally, for both strains grown under restrictive conditions, Fum1 and Lpd1, two enzymes of the TCA cycle, were higher abundant in comparison to cells grown under permissive conditions. Whereas the catalytic subunit of the acetolactate synthase Ilv2, which is involved in fermentation processes, and the 6-phosphogluconate dehydrogenase Gnd1 of the pentose phosphate pathway were higher abundant for Cdc48-psd^3 and bPAC cells grown under permissive conditions. Ilv2 and Gnd1 were also found to be lower abundant for the bPAC strain grown under restrictive conditions in comparison to the WT strain. Furthermore, as mentioned earlier, Pho8 involved in the depletion of the cordycepin precursor 3'AMP was higher abundant for Cdc48-psd^3 and bPAC cells grown under restrictive conditions in comparison to permissive growth conditions. In the comparison of DAPs for the Clb2$^{\Delta DB}$-psd^3 and the bPAC strain, the NADH-cytochrome b_5 reductase Mcr1 involved in ergosterol production was found to be higher abundant for both strains grown under restrictive growth conditions but was found to be lower abundant for growth-restricted Cdc48-psd^3 cells in the comparison to the WT and to Cdc48-psd^3 cells grown under permissive light conditions.[63] A detailed overview of the DAPs summarized in figure 2.20 is provided by tables 5.19 and 5.20 in the appendix section. In addition to the DAPs mentioned earlier, the two PKA subunits Tpk1 and Tpk2 were low abundant for Cdc48-psd^3 cells cultured under restrictive light condition in comparison to the WT strain, whereas the third subunit was not found in the dataset. This finding might imply a lower PKA activity for Cdc48-psd^3 cells in comparison to the WT strain, which would link the Cdc48-psd^3 and the bPAC strain, where PKA activity is controlled by blue light dependent cAMP production.

2.2.2.5 Heatmaps for DAPs of Interest

Heatmaps in figure 2.21 were generated to visualize relative protein for the DAPs of interest identified above and show great homogeneity of abundance ratios among the biological triplicates for each sample group. This is reasonable because DAP criteria are demanding $p < 0.01$ for a Student's t-test comparing the abundance of the triplicates of both sample groups. In terms of abundance difference Erg1, Erg3, Erg11 and Erg25 stand in the comparison of growth-restricted Cdc48-psd^3 cells with the WT strain. In the comparison of Cdc48-psd^3 cells grown under restrictive and permissive growth condition, Erg25 and Erg3 exhibit the highest abundance differences for the DAPs of interest. For the Clb2$^{\Delta DB}$-psd^3 strain, only small abundance differences between the selected DAPs are visualized by the heatmaps. In regard to the bPAC strain Acs1 exhibits noticeably higher abundance for restricted bPAC cells in the comparisons to the WT strain and to the permissive growth condition.

In addition, abundances for proteins involved in ergosterol production were mapped on the mevalonate pathway and the ergosterol biosynthesis superpathway. Corresponding heatmaps were generated for the Cdc48-psd^3 and bPAC strains and are summarized by figure 3.1 in the appendix section in order to avoid redundance. These heatmaps also visualize relative protein abundance for non-DAP pathway proteins and will be discussed in section 3.2.

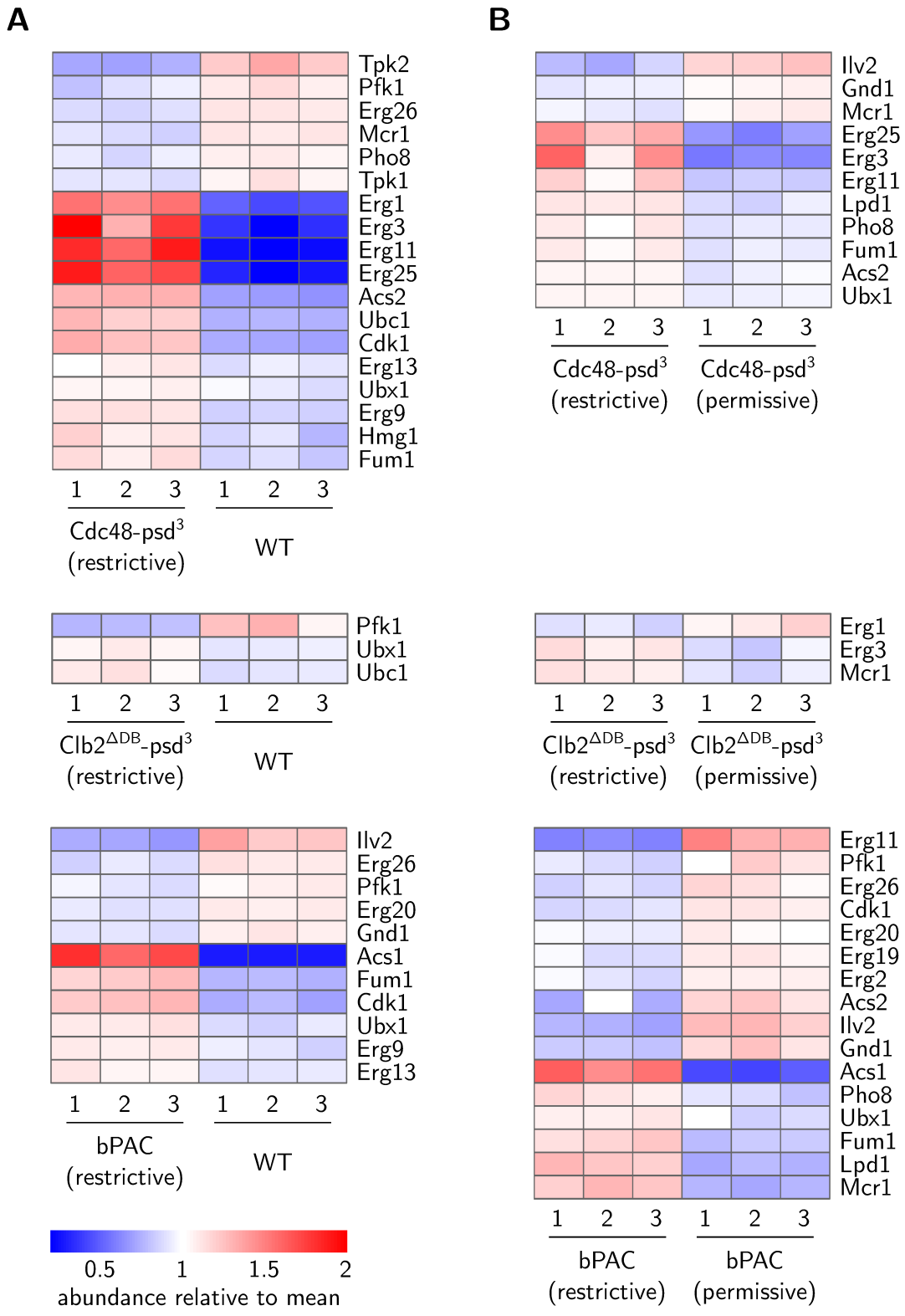

Figure 2.21: Heatmaps for selected DAPs of interest. Abundance was plotted relative to the mean abundance over both sample groups, and their three biological triplicates. **A** DAPs of interest for the comparisons of the Cdc48-psd^3, Clb2$^{\Delta DB}$-psd^3 and the bPAC CCM yeast strains cultured under restrictive growth conditions with the corresponding WT strains. **B** DAPs of interest for the comparisons of the Cdc48-psd^3, Clb2$^{\Delta DB}$-psd^3 and the bPAC CCM yeast strains cultured under restrictive and permissive growth conditions.

2.2.2.6 DAPs Involved in Pathways of the Central Metabolism

Metabolites and energy provided by the central metabolism are crucial for the metabolic capacity of the desired light-controlled production strains. Hence, the obtained proteomics data was analyzed for abundances of proteins involved in the TCA cycle, respiratory chain, glycolysis/glucose fermentation and the pentose phosphate pathway. In a first step, proteins involved in the mentioned pathways were analyzed for overlaps with identified DAPs for each CCM yeast strain and comparison. The corresponding protein targets of the central metabolism and overlaps with the respective DAPs are summarized in tables 5.21 to 5.25 in the appendix section. Obtained results were then used to identify pathways which were particularly impacted in specific comparisons. For these comparisons, heatmaps were generated in order to visualize relative abundance for all proteins involved in the specific pathway, thereby helping to understand the overall pathway regulation.

For the Cdc48-psd^3 strain, many proteins involved in glycolysis/glucose fermentation were found to be lower abundant for growth-restricted Cdc48-psd^3 in comparison to the WT strain. Nevertheless, the alcohol dehydrogenases Adh1 and Adh3 responsible for ethanol synthesis were found to be higher abundant for growth-restricted Cdc48-psd^3 in this comparison. As visualized by the heatmap in figure 2.22, moderate abundance differences were observed in the analysis. For the bPAC strain, significantly less DAPs involved glycolysis/glucose fermentation were identified. Most of them were identified in the comparison between the restrictive and the permissive growth condition. Here, the hexokinase II (Hxk2) and both subunits of the phosphofructokinase (Pfk1 and Pfk2) were found to be $\approx 20\,\%$ lower abundant for growth-restricted bPAC. Furthermore, the pyruvate decarboxylase Pdc5 was found to be less abundant, whereas the enolase Eno1 and the alcohol dehydrogenase Adh1 were found to be higher abundant for growth-restricted bPAC in comparison to the permissive condition.

In the comparison of the growth-restricted Clb2$^{\Delta DB}$-psd^3 strain to the permissive growth condition, many DAPs assigned to the TCA cycle and the respiratory chain were found to be low abundant for the growth-restricted Clb2$^{\Delta DB}$-psd^3 strain. Even though these abundance trends were clearly visible on the corresponding heatmaps visualized in figure 2.22, abundance differences between both light conditions were relatively small. However, this observation was not made comparing both light conditions of the WT strain (data not shown), which could have indicated a more general effect caused by the cultivation conditions.

For the bPAC strain, rather strong abundance differences were observed for proteins involved in the TCA cycle and the respiratory chain. Here, most DAPs were high abundant in the comparisons of the growth-restricted bPAC strain to the WT strain and the permissive growth condition. Corresponding heatmaps visualizing protein abundances for both pathways are shown in figure 2.23.

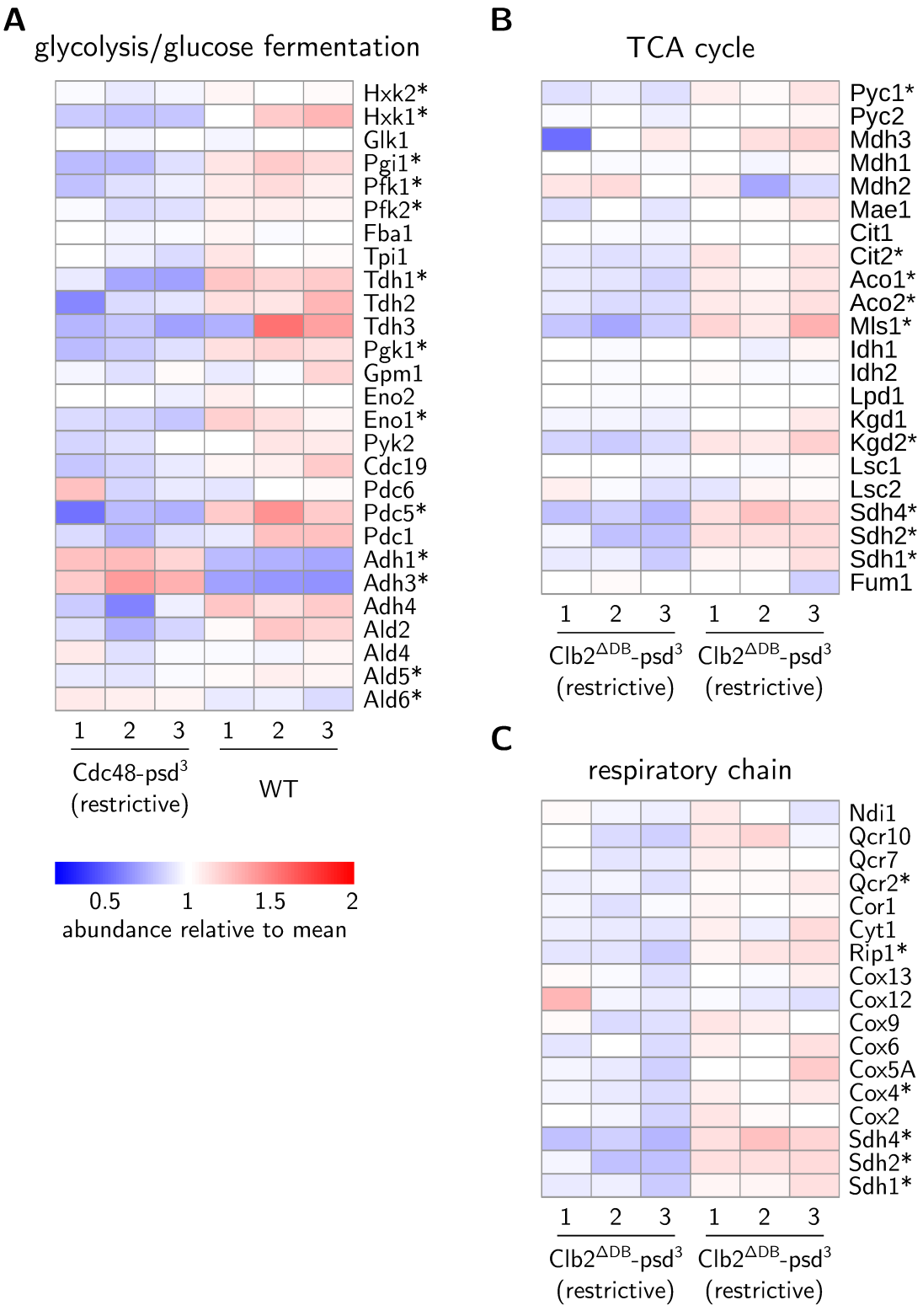

Figure 2.22: Heatmaps for selected pathways of the central metabolism. **A** Relative abundances of proteins involved in glycolysis/glucose fermentation for the comparison Cdc48-psd^3 (restrictive) vs WT strain **B** Relative abundances of proteins involved in the TCA cycle for the comparison Clb2$^{\Delta DB}$-psd^3 (restrictive) vs Clb2$^{\Delta DB}$-psd^3 (permissive). **C** Relative abundances of proteins involved in the respiratory chain for the comparison Clb2$^{\Delta DB}$-psd^3 (restrictive) vs Clb2$^{\Delta DB}$-psd^3 (permissive). * marks identified DAP for the comparison.

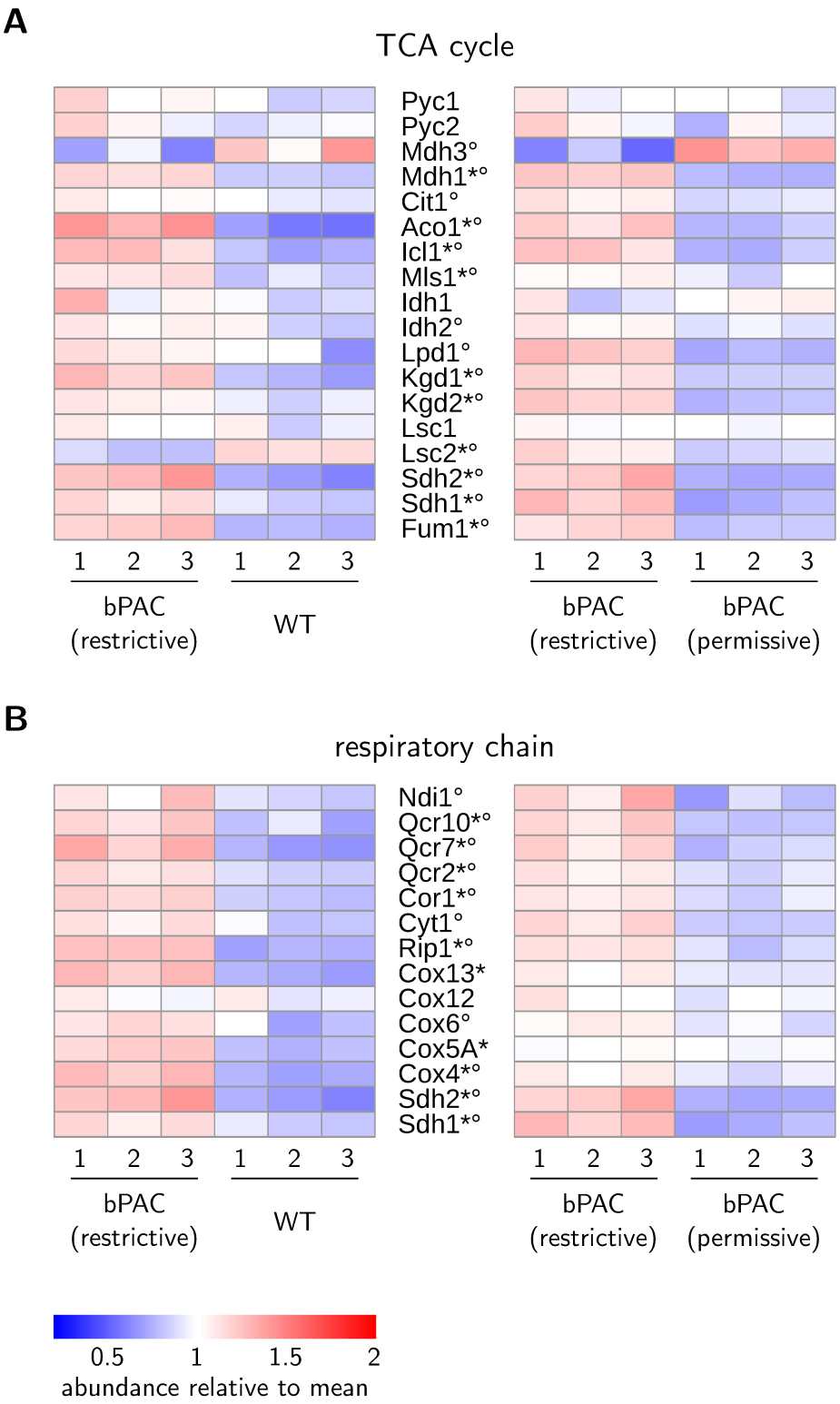

Figure 2.23: Heatmaps for selected pathways of the central metabolism. **A** Relative abundances of proteins involved in the TCA cycle for the comparison of the growth-restricted bPAC strain in comparison to the WT strain and to the permissive condition. **B** Relative abundances of proteins involved in the respiratory chain for the comparison of the growth-restricted bPAC strain in comparison to the WT strain and to the permissive condition. * marks DAP in the comparison of the bPAC strain cultured under restrictive growth conditions and the WT strain. ° marks DAP in the comparison of the bPAC strain cultured under restrictive and permissive growth conditions.

2.2.3 Gene Ontology (GO) Enrichment Analysis

The targeted DAP analysis revealed DAPs of interest for specific metabolic pathways, nevertheless the overall picture of differences between sample groups remained unclear. Each comparison of protein abundances in section 2.2.2 for Clb2$^{\Delta DB}$-psd^3 resulted in dozens and for Cdc48-psd^3 and for the bPAC strain in hundreds of identified DAPs. Corresponding lists of DAPs are almost impossible to curate manually and a Gene Ontology (GO) enrichment analysis was performed in order to statistically evaluate which processes, functions and components of the cell were affected in the comparison of both sample groups. Results of the GO enrichment analyses were plentiful and needed to be condensed. Here, representative, non redundant GO-terms were selected to visualize the overall outcome of the GO enrichment analysis.

2.2.3.1 GO-Terms – Cdc48-psd^3

For the Cdc48-psd^3 strain, a total of 109 statistically significant GO-terms were identified in the comparison of Cdc48-psd^3 cells grown under restrictive conditions and the WT strain. Corresponding representative GO-terms are summarized in figure 2.24. For the comparison of the Cdc48-psd^3 and the WT strain shifts in the abundance of proteins involved in α-amino acid metabolic processes (GO:1901605) were observed. Furthermore, the term "oxidoreductase activity, acting on the CH-OH group of donors, NAD$^+$ or NADP$^+$ as acceptor" (GO:0016616) was obtained implying changes on catabolic and anabolic activities between both sample groups. For proteins involved in alcohol biosynthesis processes (GO:0046165), relative protein abundances were found to be increased for the growth-restricted Cdc48-psd^3 strain in comparison to the WT strain. In terms of the allocation of DAPs to specific cellular components, the ribonucleoprotein granule (GO:0035770) exhibited a high enrichment factor. Proteins associated to RNA granules control the localization, stability, and translation of their RNA cargo and might imply a stress response of growth-restricted Cdc48-psd^3 cells. Furthermore, the GO-term (GO:0044432) "endoplasmic reticulum part" was identified (p-value: 0.006, enrichment: 1.80, data not shown). Here, 37 of the 53 associated DAPs were higher abundant for growth-restricted Cdc48-psd^3 cells.
In the comparison of the Cdc48-psd^3 strain grown under restrictive and permissive conditions, a total of only 37 GO-terms were identified. As in the comparison to the WT strain the term "α-amino acid metabolic processes" (GO:1901605) was identified as GO-term for the list of provided DAPs. Here, for the most part protein abundances were higher for Cdc48-psd^3 cells grown under restrictive conditions. Furthermore, the GO-term "oxidoreductase activity" (GO:0016491), a parental term of GO:0016616 (GO-term found in the comparison to the WT strain), was among the results of the GO-term enrichment analysis. In regard to the allocation of DAPs to cellular components, the GO enrichment analysis pointed towards the endoplasmic reticulum (GO:0005783). Shared

GO-terms between both comparisons for the Cdc48-psd^3 strain were to be expected as both comparisons had most of the DAPs in common.

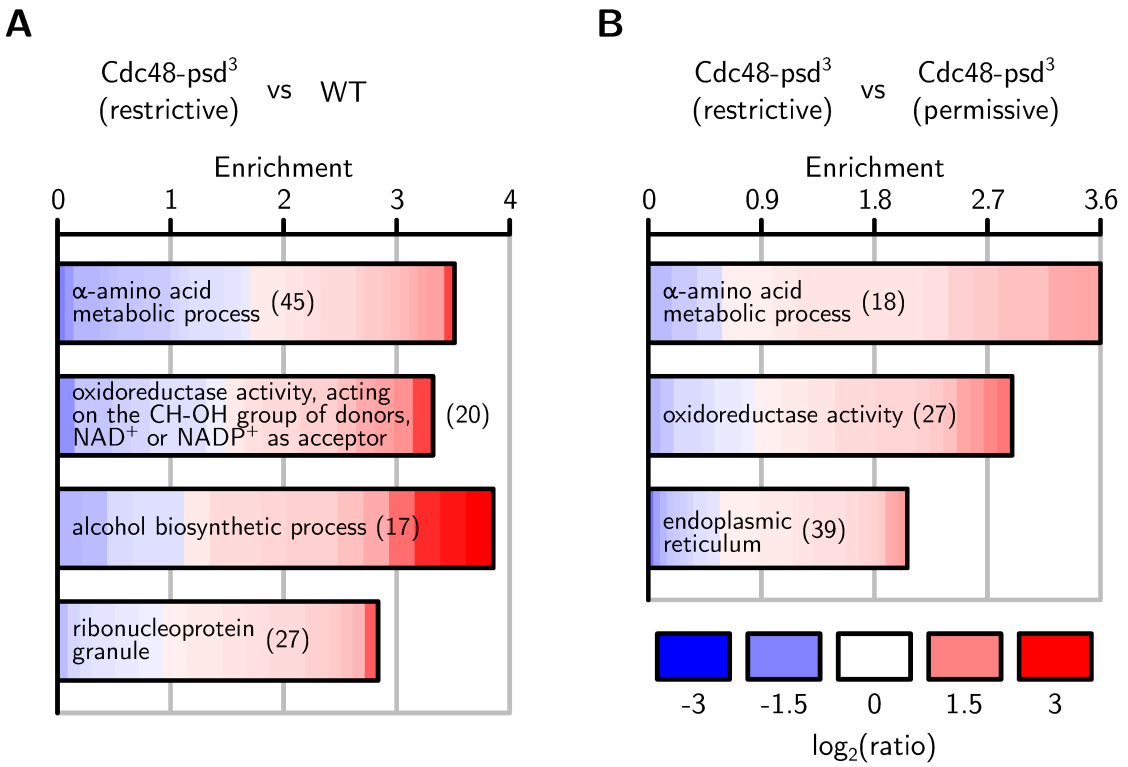

Figure 2.24: Selected GO-terms for the Cdc48-psd^3 strain with enrichment factors and abundance ratios for corresponding DAPs. The number of assigned DAPs for the GO-term is denoted in brackets. **A** GO-terms for the comparison of the Cdc48-psd^3 strain grown under restrictive conditions and the WT strain. 504 DAPs were used as input. **B** GO-terms for the comparison of the Cdc48-psd^3 strain cultured under restrictive and permissive growth conditions. 194 DAPs were used as input.

2.2.3.2 GO-Terms – Clb2$^{\Delta DB}$-psd^3

For the DAPs of the comparison between growth-restricted Clb2$^{\Delta DB}$-psd^3 cells and the WT strain, 47 GO-terms were identified in the GO enrichment analysis. Most of these terms were referring to the ribosome or to cytoplasmic translation (GO:0002181). Here, all DAPs had a slightly higher abundance for restricted Clb2$^{\Delta DB}$-psd^3 cells. Additionally, the more general GO-term "biosynthetic process" (GO:0009058) was identified.
Using the DAPs of the comparison between the Clb2$^{\Delta DB}$-psd^3 strain grown under restrictive and permissive conditions as input for the GO-term enrichment analysis 43 GO-terms were obtained. Here, the GO-terms "aerobic respiration" (GO:0009060) and "drug metabolic process" (GO:0017144) were identified and the corresponding DAPs exhibited a lower abundance for Clb2$^{\Delta DB}$-psd^3 cells grown under restrictive conditions. This result is in accordance to the findings described in section 2.2.1. Here, many proteins involved in the respiratory chain were found to be low abundant in the comparison of the Clb2$^{\Delta DB}$-psd^3 strain cultured under restrictive and permissive conditions.

Due to the limited amount of identified DAPs for both comparisons of the Clb2$^{\Delta DB}$-psd^3 strain, the variety of obtained GO-terms was rather small. It is noteworthy that, the resulting terms did not exhibit any overlap between both comparisons. Hence, results obtained for both comparisons differed greatly not only in the DAP analysis, as shown by the Venn plot in figure 2.17, but also at the level of GO-terms.

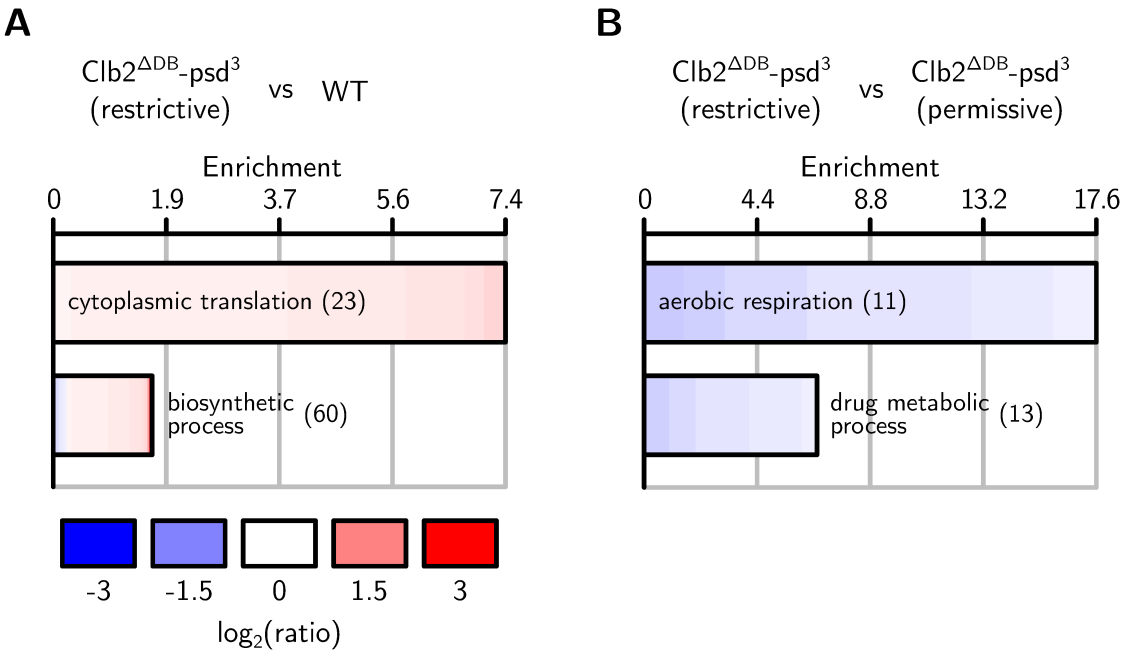

Figure 2.25: Selected GO-terms for the Clb2$^{\Delta DB}$-psd^3 strain with enrichment factors and abundance ratios for corresponding DAPs. The number of assigned DAPs for the GO-term is denoted in brackets. **A** GO-terms for the comparison of the Clb2$^{\Delta DB}$-psd^3 strain grown under restrictive conditions and the WT strain. 197 DAPs were used as input. **B** GO-terms for the comparison of the Clb2$^{\Delta DB}$-psd^3 strain cultured under restrictive and permissive growth conditions. 51 DAPs were used as input.

2.2.3.3 GO-Terms – bPAC

For the growth-restricted bPAC strain 203 GO-terms were identified in the to the WT strain. Here, the GO-term "small molecule biosynthetic process" (GO:0044283) exhibited more high abundant DAPs for bPAC in comparison to the WT strain. As observed for the Cdc48-psd^3 strain the term "oxidoreductase activity, acting on the CH-OH group of donors, NAD^+ or $NADP^+$ as acceptor" (GO:0016616) showed high enrichment, implying impacts on catabolism and anabolism in the comparison of both sample groups. Furthermore, the term "cytoplasmic translation" (GO:0002181) was obtained for the GO enrichment analysis. Here, all corresponding DAPs were higher abundant for growth-restricted bPAC cells in comparison to the WT strain. In regard to the cellular allocation of DAPs the term "ribonucleoprotein granule" (GO:0035770) was identified. This finding is in accordance with observations made for the Cdc48-psd^3 strain in comparison to the WT strain and may indicate a general stress response of growth-restricted CCM cells.

The GO enrichment analysis for the comparison of bPAC cells grown under restrictive and permissive conditions resulted in 233 identified GO-terms. As in the comparison with the WT strain the GO-term "small molecule biosynthetic process" (GO:0044283) was identified, but in contrast DAPs were found to be mostly of low abundance for the restrictive growth condition in comparison to the permissive condition. Furthermore, as observed in the comparison to the WT the term "oxidoreductase activity, acting on the CH-OH group of donors, NAD^+ or $NADP^+$ as acceptor" (GO:0016616) was identified. Another GO-term with high enrichment factors was "detoxification" (GO:0098754). Here, DAPs were of higher abundance mostly for growth-restricted bPAC cells indicating cellular stress due to the lack of cAMP supply. Nevertheless, DAPs associated to the generation of precursor metabolites and energy (GO:0006091) were found to be for the most part of higher abundance for the growth-restricted bPAC strain, which indicates a change in energy availability for growth-restricted bPAC cells in comparison to the permissive condition. This finding is in accordance to the results described in section 2.2.1. Here many proteins involved in the TCA cycle and the respiratory chain were found to be high abundant in the comparison of bPAC cells cultured under restrictive and permissive conditions. Furthermore, the term "ergosterol metabolic process" (GO:0008204) relating to the production of β-carotene and the GA_4 was obtained. Hence, for the bPAC strain, induced growth-restriction may have a direct impact on the production of valuable target molecules within the MELICOMO project. This finding is further discussed in section 3.2.

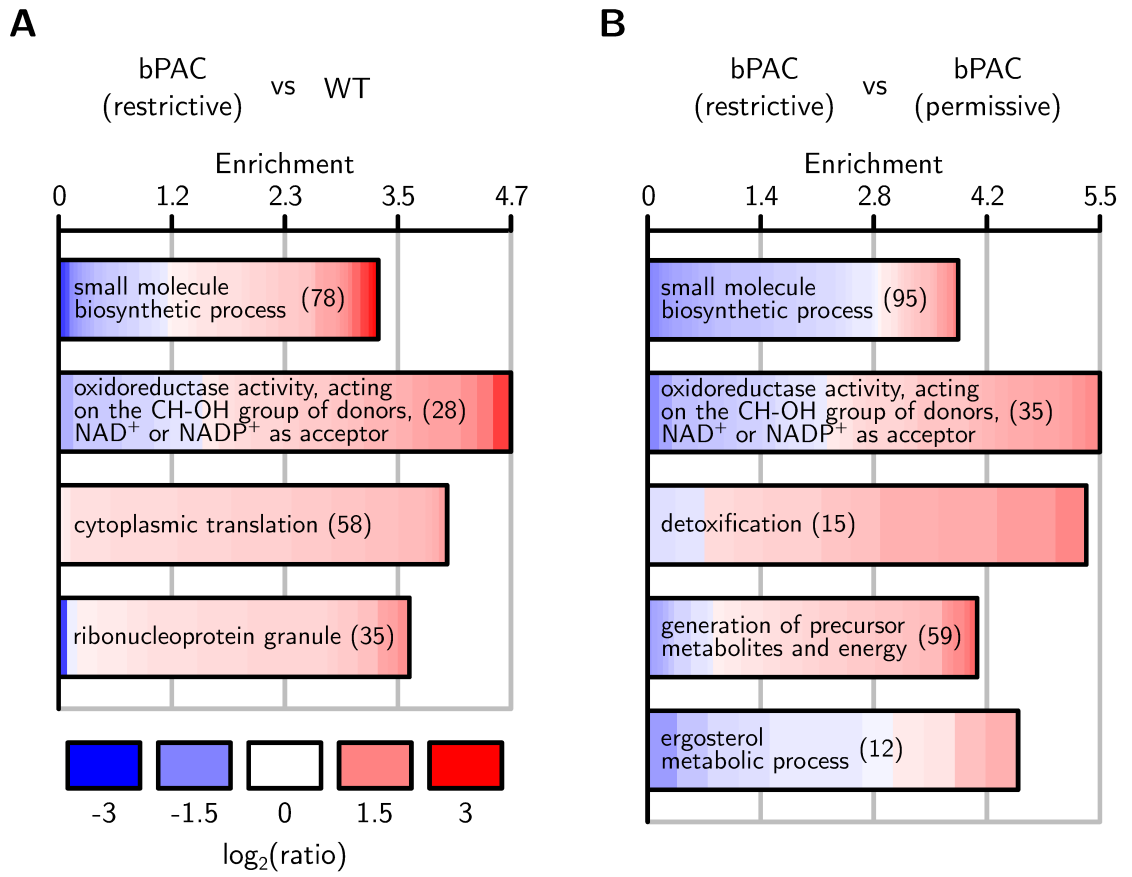

Figure 2.26: Selected GO-terms for the bPAC strain with enrichment factors and abundance ratios for corresponding DAPs. The number of assigned DAPs for the GO-term is denoted in brackets. **A** GO-terms for the comparison of the bPAC strain grown under restrictive conditions and the WT strain. 506 DAPs were used as input. **B** GO-terms for the comparison of the bPAC strain cultured under restrictive and permissive growth conditions. 527 DAPs were used as input.

2.2.4 Proteomics of Light-Controlled *S. cerevisiae* – Summary

Proteomics data obtained for the Cdc48-psd^3, Clb2$^{\Delta DB}$-psd^3 and bPAC CCM yeast strains had a good coverage in regard to the provided data base of S288c/SK1 gene products and was a solid data basis for further analysis after quality filtering. For CCM cells of the Cdc48-psd^3 and bPAC strain, a clear impact of the light condition on the proteome was observed. Furthermore, both CCM strains were clearly distinguishable from corresponding WT strains as demonstrated by the heatmaps, respectively. In contrast for the Clb2$^{\Delta DB}$-psd^3 strain differences between restrictive and permissive growth condition of Clb2$^{\Delta DB}$-psd^3 cells and in general differences between the Clb2$^{\Delta DB}$-psd^3 and the WT strain were significantly smaller.
In order to examine beneficial differences on the proteome level for the production of the target molecules within the MELICOMO project, DAPs were analyzed for the CCM yeast strains. The analysis of DAPs revealed that many proteins of the ergosterol biosynthesis superpathway were differentially abundant for the examined comparisons of Cdc48-psd^3 and the bPAC strain. This finding implies different production capacities for the CCM and the WT strains for β-carotene and GA_4, as precursors of both molecules branch off the ergosterol biosynthesis superpathway. For the Cdc48-psd^3 strain most of the pathway proteins were higher abundant for Cdc48-psd^3 cells cultured under restrictive growth condition in comparison to the WT strain and the permissive growth condition. For growth-restricted bPAC cells, identified DAPs were evenly distributed in comparison to the WT strain and slightly less abundant in comparison to the permissive light condition. These results are discussed in more detail in section 2.26. Interestingly, an acetyl-CoA synthetase isoform was of high abundance in both comparisons for Cdc48-psd^3 and bPAC grown under restrictive light conditions. This finding may imply an increased availability of acetyl-CoA as the initial precursor of the mevalonate pathway with beneficial effects on the production of β-carotene and GA_4. Furthermore, Pho8 involved in the depletion of the cordycepin precursor 3'AMP was found to be of lower abundance for growth-restricted Cdc48-psd^3 cells in comparison to the WT strain.
The analysis of relative abundances for proteins of the central metabolism revealed that enzymes involved in glycolysis/glucose fermentation were found to be overall lower abundant in the comparison of the growth-restricted Cdc48-psd^3 and the WT strain. Furthermore, many proteins involved in the TCA cycle and the respiratory chain were found to be lower abundant for growth-restricted Clb2$^{\Delta DB}$-psd^3 cells in comparison to the permissive condition. Nevertheless, differences in abundance for these comparisons were rather small. For bPAC cells cultured under restricted growth condition overall higher abundances for proteins involved in the TCA cycle and the respiratory chain were observed in the comparisons to the permissive condition and to the WT strain. These findings might indicate a in general higher energy and precursor availability for the bPAC strain under restrictive growth conditions.

In the GO-term analysis for DAPs of both analyzed comparisons for the Cdc48-psd^3 strain, abundance differences for proteins involved in the metabolic process of α-amino acids and oxidoreductase activity were observed. For the bPAC strain, small molecule biosynthetic processes and oxidoreductase activity were impacted as found in the GO-term analysis. These observations point towards a light-dependent different metabolic state for both CCM strains, which might be an explanation the increased production of the desired target molecules within the MELICOMO project.

Summarizing the results of the proteomics experiment for light-controlled *S. cerevisiae*, meaningful proteomic insights were obtained for the Cdc48-psd^3 and the bPAC strains. These findings help to explain the increased productivity for the light-controlled CCM strains in comparison to WT cells and effects of light-controlled growth-restriction for both CCM strains. For the Clb2$^{\Delta DB}$-psd^3 strain the obtained results were less convincing and the analysis of the obtained data raised the question whether the desired cell cycle arrest phenotype was induced for Clb2$^{\Delta DB}$-psd^3 cells during cultivation at all.

2.3 Bioanalysis for Production Strain Establishment

In the present work, advanced analytical tools were used for the establishment of *S. cerevisiae* strains in the context of metabolic engineering, and a selection of the analyses performed is presented below.

2.3.1 β-Carotene Production

Within the MELICOMO project various *S. cerevisiae* strains were transformed with the plasmid pUDE269 to enable β-carotene production from cellular FPP via GGPP. Alternatively, the respective genes for β-carotene production were genomically integrated in order to overcome variations in plasmid copy numbers between different clones. Just like the recombinant pathway for GA_4 production, β-carotene biosynthesis branches off the mevalonate pathway from FPP via GGPP. Hence β-carotene production was monitored to test different strains and cultivation conditions in order to transfer the obtained insights to GA_4 production. Thereby β-carotene was detected in microscopy and flow cytometric experiments by its fluorescence and from cell extracts in HPLC experiments by the absorbance of light at $\lambda = 450\,nm$.
During my doctorate I routinely performed HPLC quantifications of β-carotene from cell extracts and the obtained results are summarized by the theses of Dr. Johannes Scheffer and Dr. Jonathan Trauth.[92] [100] Figure 2.27 visualizes representative chromatograms for the separation of a β-carotene standard and cell extracts by HPLC. Furthermore, a linear regression of signal areas for β-carotene standards is shown.

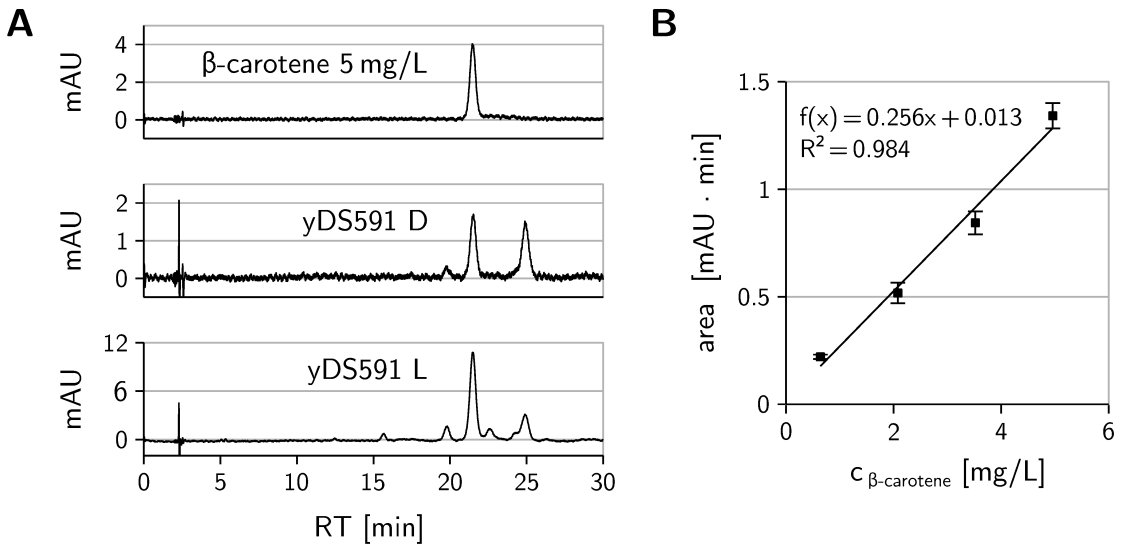

Figure 2.27: **A** Chromatograms of HPLC β-carotene analyses for a calibration standard and extracts of strain yDS591 (derivative of the Cdc48-psd[3] strain with genomically integrated β-carotene pathway) cultured in darkness (D, permissive condition) and under blue light conditions (L, 465 nm, 30 $\frac{\mu mol}{m^2 \cdot s}$, restictive condition) Absorbance was monitored at $\lambda = 450\,nm$. **B** Linear regression of peak areas for β-carotene standards measured in triplicate.

The applied LC-method allowed a good separation of β-carotene from cell extracts, while maintaining well defined peak shapes. Nevertheless, for standard solutions β-carotene showed a limited solubility in 50 % ACN 50 % MeOH ($\approx 5\,mg/L$) and powdery β-carotene precipitated under the cooled storage conditions of the autosampler for higher concentrations. Cell extracts were found to contain β-carotene concentrations of 10 mg/L and higher, presumably kept in solution by coextracted substances. As visualized by figure 2.27, beside the β-carotene peak, a fair amount of other signals were visible at $\lambda = 450\,nm$ for cell extracts, presumably caused by β-carotene precursor lycopene or *cis* and *trans* isomers.[31] [74] Intensities of these signals seemed to vary in between batches of analyzed samples and were usually not as prominent as for the shown samples.

2.3.2 3'AMP and Cordycepin Production

The potential anti-cancer drug cordycepin was one of the main target molecules to be produced in a metabolic engineering approach within the MELICOMO project. Cordycepin is produced by the fungus *Cordyceps militaris* from cellular 3'AMP, a precursor also available in limited amounts in *S. cerevisiae* due to the degradation of RNA.[107] During the MELICOMO project, Bastian Pook focused on the generation of *S. cerevisiae* strains providing an increased 3'AMP supply and on engineering strains for cordycepin production.
Within the present work, sample preparations and mass spectrometric methods were established in order to enable 3'AMP and cordycepin quantification from *S. cerevisiae* cultures and a summary of the obtained results is presented below.

2.3.2.1 LC-MS Quantification of 3'AMP

In *C. militaris* 3'AMP is generated from adenosine by the enzyme Cns3. Here, Cns3 catalyzes also the reaction of adenosine to pentostatin, a molecule regulating cellular levels of cordycepin by inhibiting adenosine deaminase activity.[107] Within the MELICOMO project, Bastian Pook generated plasmids for the expression of *CNS3* controlled by the blue light-sensitive transcription factor LexACry2/Cib1-VP16, which allowed Cns3 production in *S. cerevisiae* under blue light. Furthermore, different shortened *CNS3* variants were generated in order to eliminate pentostatin production of Cns3.
Within the present work, 3'AMP was quantified by LC-MS from strains expressing *CNS3* in full length (strain yDS495 + pDS263), different shortened constructs of *CNS3* (strains yDS495 + pBP02, yDS495 + pBP03 and yDS495 + pBP04) and the WT strain (yDS495). Culture media and cell extracts were provided by Bastian Pook. Here, 3'AMP was detected in corresponding samples of cell extracts but not in samples prepared from culture media. Figure 2.28 shows representative EICs of the separation of 3'AMP and 5'AMP and the linear regression of calibration standards for 3'AMP. Data plotted for the linear regression is summarized in table 5.28 in the appendix section.

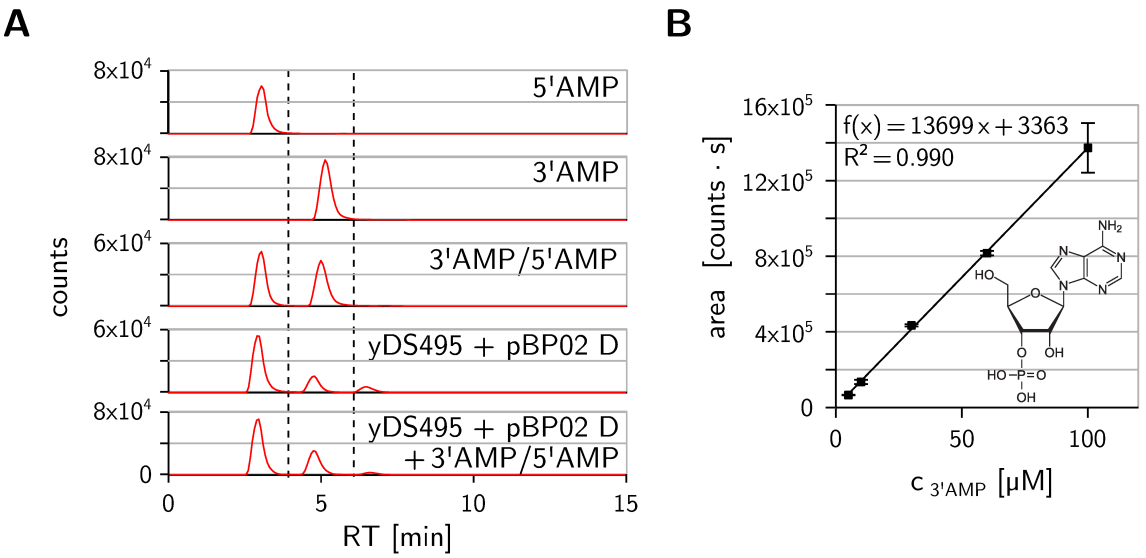

Figure 2.28: LC-MS quantification of 3'AMP from cell extracts. **A** Exemplary EICs ($m/z = 346.0558 \pm 5$ ppm) for 5'AMP, 3'AMP, 3'AMP/5'AMP and for extracts of strain yDS495 + pBP02 grown in darkness with and without 3'AMP/5'AMP spike. The retention time window for 3'AMP is indicated. **B** Linear regression for signal areas of 3'AMP calibration standards measured in triplicate.

Ion pair chromatography allowed baseline separation of the isobaric compounds 3'AMP and 5'AMP on a regular C18 reversed phase HPLC column and corresponding chromatographic peaks were assigned to both nucleotides by their retention times. As illustrated for sample generated from strain yDS495 + pBP02 D, spiked samples exhibited an increased signal intensity for 3'AMP and 5'AMP. Figure 2.29 and table 2.5 show the results of 3'AMP quantification for all examined strains cultured in darkness (D) and under blue light conditions (L).

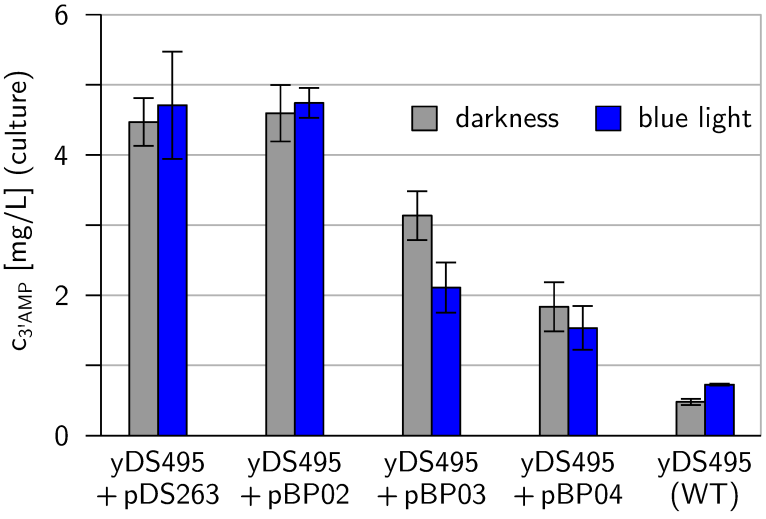

Figure 2.29: 3'AMP quantification for *S. cerevisiae* producing variants of Cns3 and the WT strain.

Table 2.5: Obtained 3'AMP concentrations determined for the cell extracts and calculated for the corresponding culture (equivalent to half of the sample concentration). Standard deviations are denoted for samples measured in triplicate.

strain	light condition	$c_{3'AMP}$ [µM] (sample)	$c_{3'AMP}$ [mg/L] (culture)
yDS495 + pDS263	D	25.7 ± 2.0	4.5 ± 0.3
	L	27.1 ± 4.4	4.7 ± 0.8
yDS495 + pBP02	D	26.5 ± 2.3	4.6 ± 0.4
	L	27.3 ± 1.2	4.7 ± 0.2
yDS495 + pBP03	D	18.1 ± 2.0	3.1 ± 0.3
	L	12.1 ± 2.1	2.1 ± 0.4
yDS495 + pBP04	D	10.6 ± 2.0	1.8 ± 0.3
	L	8.8 ± 1.8	1.5 ± 0.3
yDS495 (WT)	D	2.8 ± 0.2	0.5 ± 0.0
	L	4.2 ± 0.1	0.7 ± 0.0

As shown in table 2.5, resulting 3'AMP concentrations were very similar for samples generated from strain yDS495 + pDS263, which was expressing full length *CNS3* and for strain yDS495 + pBP02 expressing a shortened construct. These two yeast strains exhibited the highest 3'AMP concentrations measured within the experiment. Significantly less 3'AMP was found in samples for the strain yDS495 + pBP03 and even smaller concentrations were determined for samples generated from strain yDS495 + pBP04. Both strains were expressing shortened variants of *CNS3*. For samples generated from WT cells lacking Cns3, the lowest 3'AMP concentrations were determined. As visualized in figure 2.29, the light condition did not significantly influence 3'AMP production, as for most strains similar concentration ranges were obtained for cells grown in darkness and under blue light conditions. However, higher 3'AMP yields were indeed expected for the 3'AMP production strains cultured under blue light conditions, because the expression of *CNS3* was under the control of the blue light-sensitive transcription factor LexACry2/Cib1-VP16. Noteworthy, pentostatin, which is also known to be generated by Cns3, could not be detected for any strain within the analysis. Due to the usage of negative ion mode for the experiment a definitive conclusion on the absence of pentostatin can not be drawn, because positive ion mode might would have been necessary to ionize pentostatin. Furthermore, pentostatin is not charged and might get excreted from the cell, which would explain the absence in cell extracts.[52]

2.3.2.2 LC-MS/MS Quantification of Cordycepin

In *C. militaris* cordycepin is generated from 3'AMP via the deduced intermediate 2'-carbonyl-3'-deoxyadenosine by the enzymes Cns2 and Cns1.[107] The corresponding *S. cerevisiae* production strain yBP03 was generated by Bastian Pook and has *CNS2* genomically integrated, while *CNS1* is expressed from plasmid. Both genes are under

the control of the blue light-sensitive transcription factor LexACry2/Cib1-VP16. The cordycepin production strain yBP03 was further modified by his colleagues Dr. Jonathan Trauth (yJT42) and Dr. Johannes Scheffer (yJS6, yBP03 + pMB3 and yBP03 + pMB4), in order to make use of different optogenetic tools to increase the product yield. Results obtained for cordycepin quantifications using the LTQ-FT Ultra instrument are documented by the theses of Dr. Johannes Scheffer and Dr. Jonathan Trauth.[100] [92]
Within the present work, cordycepin quantification was performed using the Agilent 6470 Triple Quadrupol mass spectrometer. This instrument allows preselection of a precursor m/z-value for fragmentation and accurate identification and quantification of the target molecule via its fragment ions (qualifier and quantifier). For cordycepin, the protonated species was selected as precursor ion (m/z = 252) and its fragment ions (m/z = 119 as qualifier and m/z = 136 as quantifier) were used within the analysis. Figure 2.30 summarizes a representative mass spectrum of cordycepin after fragmentation with signals for ions used as qualifier and quantifier. Furthermore, the corresponding chromatogram for the product ion scan of the precursor is shown.

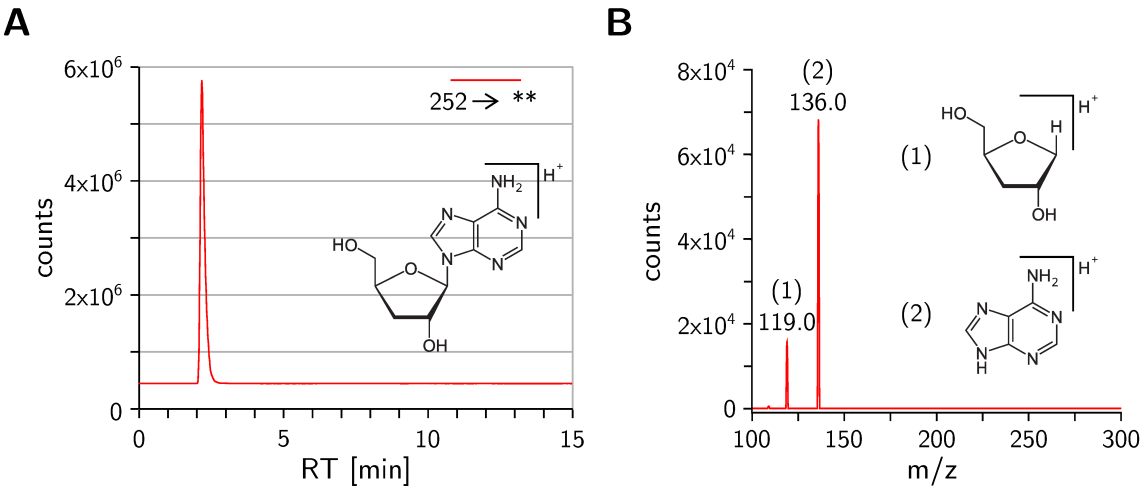

Figure 2.30: **A** TIC chromatogram of product ion scan 252 → ** for the cordycepin standard. **B** Corresponding mass spectrum for product ions of m/z = 252 as selected precursor ion.

After multiple reaction monitoring (MRM) parameter optimization, the area of the quantifier signal was about four times higher than the area of the qualifier, this characteristic quantifier/qualifier ratio was monitored in subsequent analyses. The optimized MRM settings were used for analyses of culture media obtained from the cordycepin production strains yBP03 and yJT42 grown in darkness (D, 24 h darkness) and under blue light conditions (L, 12 h darkness then 12 h blue light, 465 nm, 30 $\frac{\mu mol}{m^2 \cdot s}$). Strain yJT42 derives from the parental strain yBP03 and was generated by Dr. Jonathan Trauth within his doctorate by fusing the photosensitive degron psd^{AS} to the endogenous adenylate cyclase Cyr1, which allows blue light-induced degradation of the protein. For the yJT42 strain, cellular cAMP production and thereby protein kinase A (PKA) activity is controlled by

blue light. Here, similar to the bPAC strain grown in darkness, exposure of yJT42 to blue light leads to decreased PKA activity for the strain.

2.3.2.3 Quantification of Cordycepin by External Calibration

Within this work, cordycepin was quantified from culture media (1:100 dilution) by external calibration. Culture media were provided by Bastian Pook and were processed as described in section 4.3.2. Figure 2.31 shows chromatograms of representative MRM transitions for the separation of a cordycepin standard and culture medium sample of the cordycepin production strain yBP03. Furthermore, a linear regression of signal areas for cordycepin standards is shown.

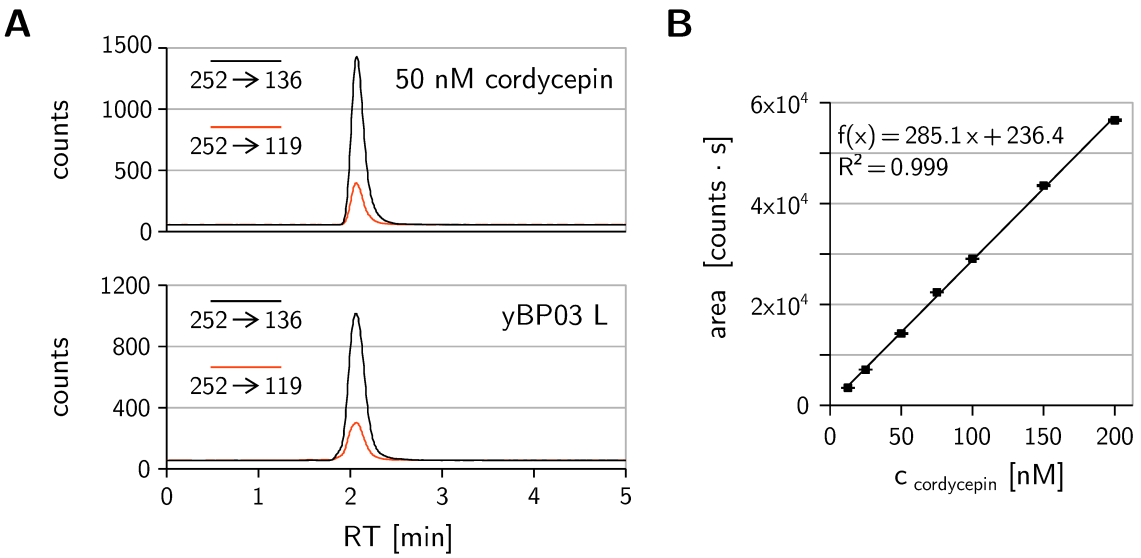

Figure 2.31: Quantification of cordycepin by external calibration. **A** Chromatograms of MRM transitions of qualifier ($252 \rightarrow 119$) and quantifier ($252 \rightarrow 136$) for the 50 nM standard and a culture medium sample for the yBP03 strain cultured under blue light conditions. **B** Linear regression for signal areas for the quantifier transition ($252 \rightarrow 136$) of cordycepin calibration standards measured in triplicate.

For the optimized separation and MRM method only a single signal was detected for the separation of cordycepin standards and media samples as shown in figure 2.31A. The linear regression of areas obtained from the quantifier transition ($252 \rightarrow 136$) exhibited a very low standard deviation and the linear regression matched the obtained mean area over the full concentration range.

Results of cordycepin quantification from culture media for the yBP03 strain, two biological replicates of the yJT42 strain and the corresponding WT strain are summarized in figure 2.32. Here, results were obtained using the external calibration shown in figure 2.31.

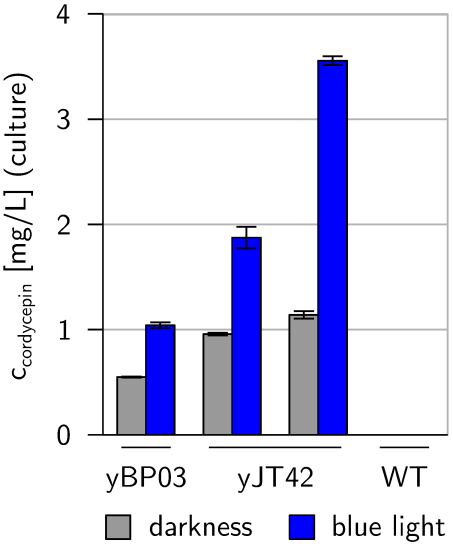

Figure 2.32: Quantification of cordycepin by external calibration for culture media of yBP03, two biological replicates of yJT42 and the corresponding WT strain.

Table 2.6: Data plotted in figure 2.32. A detailed summary of the results is provided in table 5.30 in the appendix section.

strain	biol. repl.	light condition	$c_{Cordycepin}$ (culture) [mg/L]
yBP03	1	D	0.55 ± 0.00
	1	L	1.04 ± 0.03
yJT42	1	D	0.96 ± 0.01
	1	L	1.87 ± 0.10
yJT42	2	D	1.14 ± 0.04
	2	L	3.55 ± 0.04
WT	1	D	NC
	1	L	NC

For culture media of cordycepin production strains yBP03 and yJT42, cordycepin was detected in the concentration range of mg/L for both light conditions. As expected, analyses of samples obtained from WT culture media did not result in any signal for cordycepin. For each cordycepin production strain, the quantified amount of cordycepin was significantly higher for cultures grown under blue light conditions than for cultures grown in darkness. Here, the yJT42 strain exhibited higher cordycepin yields in comparison to the yBP03 strain for both light conditions. For both biological replicates of the yJT42 strain grown in darkness, similar cordycepin concentrations were determined from the culture media. Remarkably, the resulting cordycepin concentrations for yJT42 cultures grown under blue light conditions varied strongly between both biological replicates. Here, cordycepin concentrations were found to be twice and three times the concentration of the respective biological replicate grown in darkness. Even though the blue light-sensitive transcription factor LexACry2/Cib1-VP16 should only be active under blue light conditions substantial cordycepin production was observed for both cordycepin production strains cultured in darkness. This observation is in accordance with the results discussed above where leaky *CNS3* expression controlled by LexACry2/Cib1-VP16 led to elevated 3'AMP concentrations for cells grown in darkness. Nevertheless, unlike for the experiments of 3'AMP quantification, blue light had a clear influence on cordycepin production for both examined cordycepin production strains. This applies also to strain yBP03 which was modified with the blue light-sensitive transcription factor LexACry2/Cib1-VP16 as the only optogenetic tool. The LOD calculated from the stan-

dard deviation of the linear regression (3σ threshold) was 5.7 nM and the corresponding LOQ (10σ threshold) was 19.1 nM. Each determined cordycepin concentration for the samples from culture media of cordycepin production strains was above the LOD.

2.3.2.4 Quantification of Cordycepin by Standard Addition

In order to examine matrix effects on cordycepin quantification by external calibration, the analysis was repeated using standard addition as quantification method for the same sample batch. Here, injected media samples were spiked with different concentrations of cordycepin standards in an automated process using the functionality of the HPLC multisampler. Figure 2.33 shows chromatograms of the standard addition for a representative culture medium sample and the corresponding linear regression.

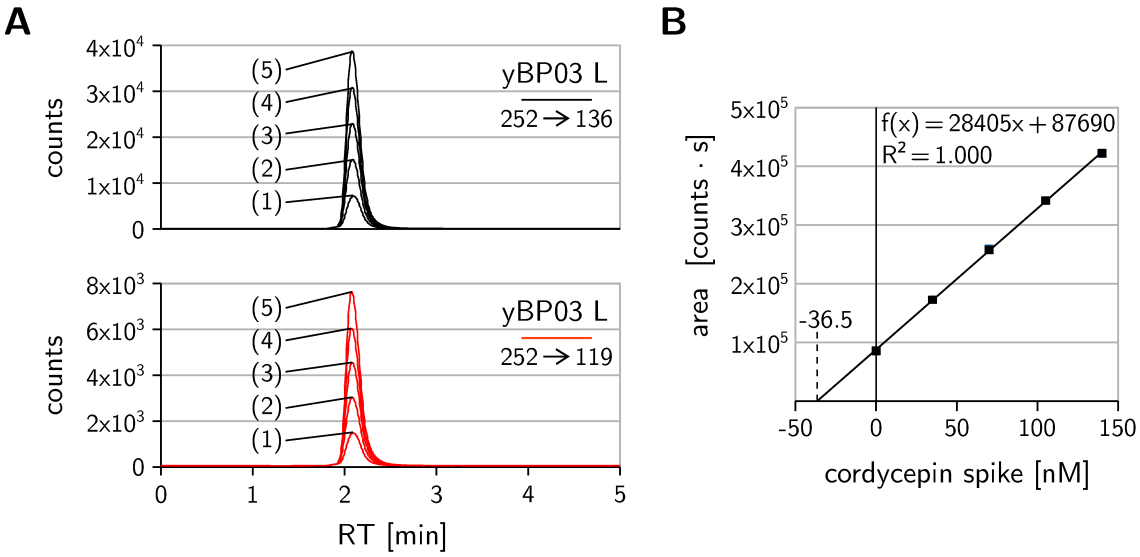

Figure 2.33: Quantification of cordycepin by standard addition. **A** Chromatograms of MRM transitions of quantifier (252 → 136) and qualifier (252 → 119) for culture medium sample for the yBP03 strain cultured exposed to blue light. The sample was spiked with 0 nM (1), 35 nM (2), 70 nM (3), 105 nM (4) and 140 nM (5) cordycepin. **B** Linear regression of signal areas for the quantifier transition (252 → 136) in the standard addition experiment measured in duplicate. The cordycepin concentration of the sample (36.5 nM) can be read off the x-axis intercept.

For cordycepin quantification by standard addition each sample was spiked with five cordycepin concentrations. Thereby 4 µL sample solution and 2 µL standard solution were drawn subsequently into the sample loop and injected afterwards. During the analysis, no split peaks or shifts in retention time were observed. Cordycepin eluted at the retention time previously observed for the LC method used for external calibration. After plotting, linear regressions provided a very good approximation of the data points (representative regression shown in figure 2.33). LODs calculated from standard deviations of the linear regressions (3σ threshold) were in the range of 2.3 - 6.9 nM and LOQs (10σ

threshold) in the range of 7.7 - 23.0 nM. Inherent to the standard addition method, a very small cordycepin concentration could have been calculated for WT samples, even though samples without a cordycepin spike were lacking any signal. Nevertheless, the resulting concentrations were below the corresponding LODs and were neglected accordingly. Summarizing the experiment, the standard addition method for cordycepin quantification was established successfully within this work.
Figure 2.34 shows the results of cordycepin quantification by standard addition from culture media samples of yBP03, two biological replicates of yJT42 and the corresponding WT strain.

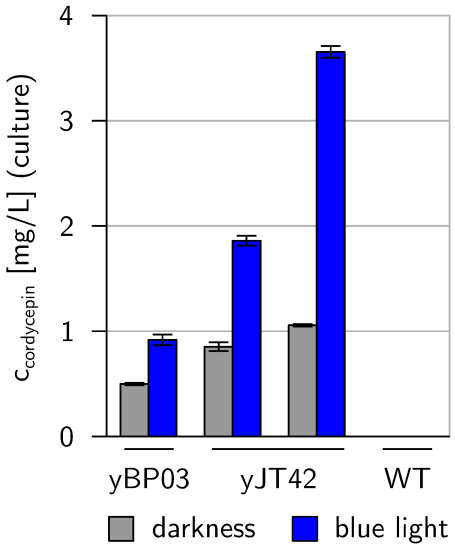

Figure 2.34: Quantification of cordycepin by standard addition for culture media of yBP03, two biological replicates of the yJT42 strain and the corresponding WT strain.

Table 2.7: Data plotted in figure 2.34. A detailed summary of the results is provided in the tables 5.31 to 5.34 in the appendix section.

strain	biol. repl.	light condition	$c_{Cordycepin}$ (culture) [mg/L]
yBP03	1	D	0.50 ± 0.01
	1	L	0.92 ± 0.05
yJT42	1	D	0.85 ± 0.04
	1	L	1.86 ± 0.05
yJT42	2	D	1.06 ± 0.01
	2	L	3.65 ± 0.06
WT	1	D	NC
	1	L	NC

Cordycepin concentrations of the culture media determined by standard addition were very similar compared to the results obtained by external calibration. For both biological replicates of the yJT42 strain, higher cordycepin concentrations were determined in comparison to the strain bBP03, independent of the light condition. Between both biological replicates of the yJT42 strain grown under restrictive blue light conditions a strong difference in cordycepin production was observed.
To facilitate comparison of the results of both quantification methods, the cordycepin concentrations determined for the culture media are summarized in table 2.8.

Table 2.8: Comparison of cordycepin concentrations for culture media obtained by external calibration and standard addition.

strain	biol. repl.	light condition	$c_{cordycepin}$ [mg/L] ext. cal.	std. add.	deviation
yBP03	1	D	0.55 ± 0.00	0.50 ± 0.01	9.1 %
	1	L	1.04 ± 0.03	0.92 ± 0.05	11.5 %
yJT42	1	D	0.96 ± 0.01	0.85 ± 0.04	11.5 %
	1	L	1.87 ± 0.10	1.86 ± 0.05	0.5 %
yJT42	2	D	1.14 ± 0.04	1.06 ± 0.01	7.0 %
	2	L	3.55 ± 0.04	3.65 ± 0.06	2.8 %
WT	1	D	NC	NC	NC
	1	L	NC	NC	NC

As shown by table 2.8, obtained results for both quantification methods deviated from each other in the range of 0.5 to 11.5 %. In the comparison, no clear trend was observed in regard to higher or lower quantification results of a respective method. Standard addition as an internal calibration method compensates for matrix effects and changes of sensitivity towards the analyte during the analysis but requires more time as for each quantification 10 measurements were necessary (5 standard additions measured in duplicate). For quantification by external calibration, 3 measurements for each sample were sufficient (measurements of calibration standards not taken into account). Summarizing the comparison, both methods have proven to be suitable for quantification of cordycepin from 1:100 diluted culture media.

2.3.3 Gibberellin A_4 Production

Gibberellin A_4 (GA_4) was one of the main target molecules within the MELICOMO project and the *S. cerevisiae* GA_4 production strain candidate yJS13 was constructed by Dr. Johannes Scheffer during his doctorate.[92] He integrated the plant genes *At*CPS, *Cm*KS, *At*KO, *Ps*KAO2, *Cm*GA20ox, *Ps*GA3ox and *At*Atr2 into the yeast genome in order to generate GA_4 from endogenous GGPP. Furthermore, the LexA-EDLL transcription factor was genomically integrated to enable constitutive expression of the recombinant genes. Unfortunately, flow cytometric analyses using a recombinant GA-reporter did not result in robust evidence for cellular GA_4 production and GA_4 was not detected in mass spectrometric analyses of cellular extracts either. As a possible explanation for this finding Dr. Johannes Scheffer observed that *Cm*KS was not clearly identified by western blot analyses, when the construct was individually expressed from plasmid. Moreover, investigations into the availability of each individual protein of the recombinant pathway for yJS13 by western blotting were troublesome, due to similar molecular weights of the pathway proteins and the usage of YFP as a fusion tag for all constructs. In order to investigate into this issue a proteomics experiment was performed for the yJS13 strain within this work. For the analysis, whole proteome digests were generated for biological

triplicates of the yJS13 and the WT strain. Samples were measured using the timsTOF Pro instrument and obtained data was analyzed via the *PEAKS* workflow. Table 2.9 summarizes obtained sequence coverage for proteins of the recombinant pathway. As each of the proteins was modified with the YFP-tag, untagged sequences were used for the database search in order to avoid cross attributions.

Table 2.9: Obtained sequence coverage for proteins of the recombinant pathway for biological triplicates of the GA_4 production strain yJS13 and the WT strain.

	sequence coverage [%]					
	WT			yJS13		
replicates	1	2	3	1	2	3
*At*CPS	0	0	0	50	50	50
*Cm*KS	0	0	0	0	0	0
*At*KO	5	5	0	56	53	52
*Ps*KAO2	0	0	0	40	40	38
*Cm*GA20ox	0	0	0	37	41	39
*At*Atr2	0	0	0	43	27	33
LexA-EDLL	0	0	0	38	33	33

As visualized by table 2.9, each protein of the recombinant pathway apart from *Cm*KS exhibited a good sequence coverage which was well distributed over the full protein sequence (data not shown). In regard to the WT no to very little coverage was obtained for the target sequences. This experimental result verifies that the yJS13 strain did not express the gene of the *ent*-kaurene synthase, thereby disrupting the pathway towards GA_4, which explains the lack of GA_4 production observed in previous experiments.
Subsequently, Dr. Christof Taxis transformed the yJS13 strain with plasmids carrying genes of *ent*-kaurene synthases originating from plants (*Oryza sativa* and *Arabidopsis thaliana*) and fungi (*Fusarium fujikuroi* and *Fusarium mangiferae*). In flow cytometric analyses using a recombinant GA-reporter, cells transformed with plasmids for the production of either *Os*KS or *At*KS, showed significantly increased fluorescence (communication with Dr. Christof Taxis, data not shown). In order to quantify the amount of GA_4 produced by the newly generated GA_4 production strains, extracts of the culture media and cells were analyzed by mass spectrometry.

2.3.3.1 LC-MS Quantification of Gibberellin A_4 from Culture Media

For GA_4 quantification, cultures of yJS13 transformed with plasmids for the production of the *ent*-kaurene synthases originating from *O. sativa* (*Os*KS, strain yGA01) and *A. thaliana* (*At*KS, strains yGA02, yGA03 and yGA04) were grown and samples of cell and media extracts were prepared as described in section 4.3.3. Furthermore, cultures of yJS13* and the wild type strain yJT23* were grown and extracted as negative controls (* negative controls carried the plasmids pRS313, pRS314 and pRS316). For the GA_4 production strain candidates yGA01, yGA02, yGA03 and yGA04 gibberellin A_4 was found in the samples of media extracts but was not detected in the methanolic cell extracts. As expected, GA_4 was not found for yJS13*, as the strain was lacking production of the *ent*-kaurene synthase and for the strain yJT23*, which did not express the genes of the recombinant pathway. Exemplary extracted ion chromatograms (EICs) for the GA_4 standard and samples prepared from media extracts are shown in figure 2.35. Furthermore, the linear regression of GA_4 calibration standards is visualized by this figure.

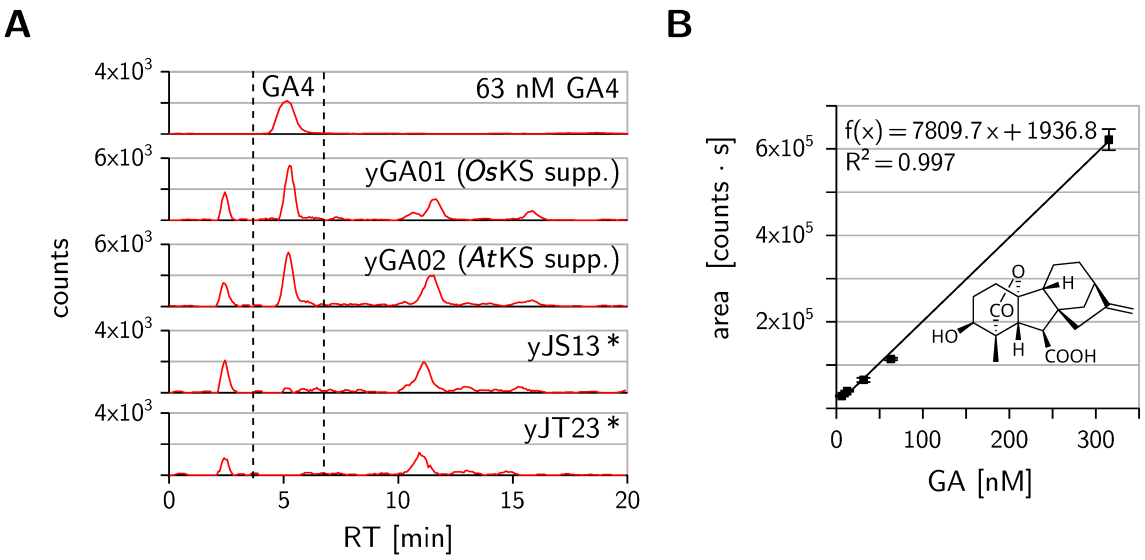

Figure 2.35: LC-MS quantification of GA_4 from media extracts. **A** Exemplary EICs ($m/z = 331.1551 \pm 3$ ppm) for the GA_4 standard and for samples of the strains yGA01 producing *Os*KS, yGA02 producing *At*KS and the WT strains yJS13* and yJT23*. The retention time window for GA_4 is indicated for the plots. Strains labeled with * were used as negative controls and carried the plasmids pRS313, pRS314 and pRS316. **B** Linear regression of signal areas of GA_4 calibration standards measured in triplicate.

As shown in figure 2.35, the obtained chromatograms for extracts of culture media were very similar but for yJS13* and the WT strain yJT23* the signal for GA_4 at ≈ 5 min was missing. Resulting GA_4 concentrations determined for the analyzed samples and GA_4 concentrations calculated for the extracted media are summarized in table 2.10.

Table 2.10: Quantification of GA_4 by LC-MS from media extracts. GA_4 concentrations are shown for the measured samples (100-fold concentrated) and for the extracted media. Standard deviations are denoted for samples measured in triplicate. Strains labeled with * were used as negative controls and carried the plasmids pRS313, pRS314 and pRS316.

strain	supplemented *ent*-kaurene synthase	c_{GA4} (sample) [nM]	c_{GA4} (medium) [ng/L]
yGA01	*Os*KS	83 ± 9	274 ± 31
yGA02	*At*KS	82 ± 18	271 ± 59
yGA03	*At*KS	51 ± 24	171 ± 80
yGA04	*At*KS	53 ± 15	175 ± 49
yJS13 *	–	ND	NC
yJT23 *	–	ND	NC

As shown in table 2.10 standard deviations of GA_4 concentrations for the measured samples were very high. This behavior was not observed for the measured calibration standards. In order to generate samples containing sufficient GA_4 for quantification, samples had to be analyzed 100-fold concentrated compared to the original extract volume. Hence, extracted contaminants were also highly concentrated in the sample, which might cause ion suppression during the LC-MS measurement and leads to an overall problematic behavior of the sample during the measurement.
Resulting GA_4 concentrations of samples for strains yGA01, yGA02, yGA03 and yGA04, producing either *Os*KS or *At*KS, were found to be similar. Corresponding GA_4 concentrations calculated for the growth media were in the range of a few hundred ng/L. Similar GA_4 concentrations were obtained in subsequent LC-MS experiments, which were performed to repeat the LC-MS analysis of growth media extracts for the same GA_4 production strains (data not shown).

2.3.3.2 Summary – Bioanalytics for Production Strain Establishment

Within this work various HPLC and LC-MS methods were established for the quantification of target molecules and a selection of exemplary analyses are presented above. Here, samples were generated from *S. cerevisiae* cells or culture media and analytes were quantified by external calibration or standard addition. The applied methods allowed quantification of target molecules in the range of ng/L to mg/L and the obtained results helped to select promising production strains for subsequent optimization cycles. In summary, instrumental analytics played an important role for the development and establishment of *S. cerevisiae* strains for the production of valuable secondary metabolites within the MELICOMO project.

Chapter 3

Discussion

Within the present work, advanced bioanalytical tools were applied for the characterization of light-controlled *S. cerevisiae* and for the quantification of target molecules in the context of metabolic engineering. Section 2.1 summarized results for biomass composition determined for light-controlled CCM yeast strains and the effect of growth restriction on the proteome of *S. cerevisiae* was further analyzed by the proteomics experiment evaluated in section 2.2. Subsequently, a representative selection of HPLC and LC-MS experiments was shown by section 2.3, which were established within this work in order to quantify β-carotene, 3'AMP, cordycepin and GA_4 from cultures of different *S. cerevisiae* production strains.
In the following chapter, the results obtained in the present work are discussed in the light of findings published in literature.

3.1 Biomass Analysis of Light-Controlled *S. cerevisiae*

The biomass composition determined for growth-restricted $Clb2^{\Delta DB}$-psd^3 cells was significantly different from the biomass composition of the WT strain and the obtained biomass compositions were used as data basis for a flux balance analysis (FBA) performed by the group of Prof. Dr. Zoran Nikoloski. Most publications discussing FBA parameters, highlight the importance of precisely adjusted biomass compositions to the respective experimental conditions,[27] [78] [79] and only few sources claim that biomass composition did not strongly impact fluxes through the central carbon metabolic network for their calculations.[111] Nevertheless, due to the laborious and error prone process of biomass analysis, research groups often rely on published data for their flux balance modeling.[111] Corresponding data on biomass composition for the model organism *S. cerevisiae* is readily available but was often generated for strain backgrounds, no longer commonly used in present laboratories. Furthermore, changes introduced into the genome, e.g. within metabolic engineering approaches, may lead to the formation of distinct phenotypes, which might not be represented by literature biomass data. Accordingly, implications

drawn from FBAs with poorly adjusted biomass composition may lead to misinterpretations in regard to fluxes through the metabolic network. Hence, for the light-controlled CCM strains used in the MELICOMO project, analyses of biomass composition prior to FBA were necessary based on the characteristic phenotypes described in the literature. Growth-restricted Clb2$^{\Delta DB}$-psd^3 and Cdc48-psd^3 cells appear mostly large budded [89] [43] and altered PKA activity due to the substitution of Cyr1 by bPAC is expected to have a broad impact on cellular processes e.g. on glycogen storage. [70] Furthermore, biomass compounds could be accumulating during cell cycle restriction, with the before mentioned consequences on the FBA calculations. In order to compare the obtained biomass data to literature, table 3.1 summarizes the determined biomass composition for the Clb2$^{\Delta DB}$-psd^3 strain and data published by Lange *et al.*

Table 3.1: Comparison of biomass composition for the Clb2$^{\Delta DB}$-psd^3 strain (S288C derivative) cultured under restrictive growth condition with literature data. Denoted ranges of literature data originate from varied dilution rates and glucose feeds applied during aerobic fermentation of the *S. cerevisiae* strain CEN.PK113-7D.

	this work		literature
	WT	Clb2$^{\Delta DB}$-psd^3	Lange *et al.* [64]
protein	23.6 $\pm$ 1.2 %	31.7 $\pm$ 1.7 %	32.3 - 45.7 %
carbohydrates	43.7 $\pm$ 3.6 %	34.1 $\pm$ 2.3 %	31.6 - 45.4 %
RNA	3.6 $\pm$ 0.4 %	5.9 $\pm$ 0.6 %	4.3 - 7.9 %
DNA	0.13 $\pm$ 0.01 %	0.11 $\pm$ 0.02 %	0.4 - 0.5 %
lipids	6.4 $\pm$ 0.3 %	7.6 $\pm$ 0.4 %	7.2 - 10.2 %

Analyzed Clb2$^{\Delta DB}$-psd^3 cells were found to contain more protein and RNA and less carbohydrates in comparison to the WT strain. Lange *et al.* observed a simultaneous increase in protein and RNA content with a decrease in carbohydrate content when the dilution rate was increased. [64] Hence, biomass composition of growth restricted Clb2$^{\Delta DB}$-psd^3 cells reflected culture conditions with high nutrient availability, while biomass composition of WT cells was similar to culture conditions with limited nutrient supply. For future experiments biomass analysis could be scaled down, focusing on the determination of protein, RNA and carbohydrate content, which were found to be significantly different in the two analyses. Excluding lipid quantification from the analysis would reduce the preparative expense significantly and allow to perform the experiment in 200 mL culture scale. Here, it would be interesting to include the analysis of Clb2$^{\Delta DB}$-psd^3 cells cultivated under permissive condition in order to distinguish between changes induced by strain-dependent differences and growth restriction. In addition, remaining glucose in the medium should be monitored to ensure that nutrient availability is similar for both strains under sampling conditions, as differences in nutrient availability would affect biomass composition. [64]

Data on biomass composition published by Lange *et al.* was chosen as a reference due to the representative range compared to other biomass compositions available in literature.[37] [79] [82] Remarkably, the percentages of the individual biomass compounds determined within the present work are all below or on the low end of the range of the reference data. Accordingly, for both analyzed strains, the sum of the determined biomass compounds did not sum up to 100 % and even if an additional 8.2 % of the dry mass was attributed to residual water, metals, inorganic phosphorus and sulfate as described by the literature,[64] the remaining undetermined biomass fraction was still $> 10\%$ for both examined strains. An explanation for this finding might be that within the present work analyte recoveries were only determined for RNA and DNA. Lange *et al.* reports recovery factors of 0.82 for protein and 0.95 for carbohydrates using highly similar biomass quantification methods. An application of these recovery factors on the results summarized by table 3.1 would reduce the undetermined biomass fraction to significantly less than 10 %. Furthermore, lyophilization for 36 h and drying for an additional 24 h at 50 °C might not have entirely removed the intracellular water from the cells and it is possible that a higher share should be attributed to remaining water. Lange *et al.* freeze-dried their cell pellets for 48 h and even dried the cells further at 70 °C for 48 h, which might have removed considerably more water from the cells. However, conclusions drawn from the direct comparison of both strains is likely to be unaffected, because Clb2$^{\Delta DB}$-psd^3 and the corresponding WT cells were treated identically and remaining undetermined fractions are highly similar in magnitude. Nevertheless, effects on FBA due to undetermined biomass can not be excluded for reasons discussed above.

3.2 Proteomics of Light-Controlled *S. cerevisiae*

The analysis of proteomics data for the Cdc48-psd^3 and bPAC yeast strains revealed deep insights into strain-dependent differences between the growth-restricted production state of CCM cells and the WT strain, as well as into differences between the restrictive and permissive light condition for both yeast strains. Unlike for the two before mentioned strains, the impact of blue light on the proteome for Clb2$^{\Delta DB}$-psd^3 cells was negligible and in the comparison to WT cells only minor differences were observed for the Clb2$^{\Delta DB}$-psd^3 strain. These observations suggest, that within sample generation the desired cell cycle arrest was not sufficiently induced for Clb2$^{\Delta DB}$-psd^3 cells and the following discussion will focus on the analysis of proteomics results obtained for the Cdc48-psd^3 and bPAC CCM strains. In the following analysis, results of the comparison between restricted CCM and the WT strain are interpreted as a combination of strain-dependent differences and differences induced by the light condition. Here, strain-dependent refers to differences already present in the comparison between the permissive growth condition of the CCM and the WT due to genetic modification. Whereas conclusions drawn

from the comparison of the CCM strain grown under restrictive and permissive growth condition point specifically at effects induced by the light condition.

Compared to WT cells, growth restriction results in an altered metabolic state for the Cdc48-psd^3 and the bPAC strain

As visualized by the heatmaps provided in section 2.2.1.1, the protein abundance profile of Cdc48-psd^3 cells grown under permissive conditions was more WT-like in comparison to cell cycle arrested Cdc48-psd^3 cells. On the other hand, growth restriction induced by cAMP depletion had a very broad impact on the proteome as visualized by the heatmaps for the bPAC strain in section 2.2.1.3. Here, protein abundances were found to be highly different between both light conditions for the bPAC strain and in comparison to the corresponding WT strains. This observation highlights that the proteome of bPAC cells cultured under permissive light conditions and the corresponding WT strain differ strongly due to the artificial cAMP level of bPAC cells, which is determined by blue light intensity and thus cannot be adapted to nutrient availability. Consequently, in contrast to the Cdc48-psd^3 strain, the permissive growth condition for bPAC does not translate into a WT-like state of the cells. It is therefore not surprising that DAPs identified in both comparisons between restrictive and permissive growth conditions for the Cdc48-psd^3 and bPAC strains overlapped only slightly, as shown by the Venn diagram in figure 2.20 B. In total, only 13 DAPs were shared by both analyses, representing 6.5 % for the Cdc48-psd^3 and 2.5 % for the bPAC strain. Nevertheless, the GO-term analysis for restrictive and permissive growth condition pointed out that both strains had an altered redox activity in common and most of the assigned DAPs were higher abundant for the growth-restricted condition compared to the permissive growth condition. This might imply a favorable metabolic state for the production of valuable molecules via recombinant pathways. On the other hand, the overlap between DAPs identified in both comparisons for the growth-restricted CCM and the WT strain was significantly higher, as shown in Figure 2.20 A. Here, 117 DAPs were shared between the two comparisons, representing 23 % of the total number of DAPs identified for each of the two comparisons. Accordingly, results of the corresponding GO enrichment analyses overlapped, indicating altered catabolic and anabolic capacity (GO:0016616, "oxidoreductase activity, acting on the CH-OH group of donors, NAD^+ or $NADP^+$ as acceptor") and an overall increased stress response (GO:0035770, "ribonucleoprotein granule") for both growth-restricted CCM strains compared to their respective WT strains. Here, in particular, the observed effects on metabolism could have a positive impact on the production of molecules via recombinant pathways for growth-restricted CCM strains.

Increased β-carotene production in growth-restricted Cdc48-psd^3 and bPAC cells could be explained by higher abundance of acetyl-CoA synthetase isoforms

In comparison to the WT strain and normalized to cell dry weight Dr. Christof Taxis observed a 18-fold increased β-carotene production for the growth-restricted Cdc48-psd^3 strain and a 5-fold increased β-carotene production compared with the permissive condition (unpublished manuscript). For the bPAC strain, Dr. Jonathan Trauth reported a 2-fold increased β-carotene production for growth-restricted bPAC cells in comparison to the WT strain normalized to dry mass and to cell culture volume.[100] Within the present work, proteomics data was analyzed for both CCM strains in order to provide possible explanations for the elevated β-carotene yields. In this section, the discussion of the data will focus on proteins involved in the biosynthesis of ergosterol (heatmap in figure 3.1 below), since the recombinant synthesis pathway for β-carotene branches off the ergosterol biosynthesis superpathway from the isoprenoid FPP, and more general insights will be discussed later in a broader context. Conclusions drawn from the analysis should be applicable to the recombinant production of GA_4, since FPP is a common precursor.
Acetyl-CoA is the initial precursor of the ergosterol biosynthetic pathway and is generated by the acetyl-CoA synthetase isoforms Acs1 and Acs2. Remarkably, for both analyzed CCM yeast strains Acs1 or respectively Acs2 was found to be high abundant for growth-restricted CCM cells in comparison to the WT strain and to the permissive growth condition. In the Cdc48-psd^3 strain, Acs2 was twice as abundant compared to the WT and was 10 % higher abundant in comparison to the permissive growth condition. For the bPAC strain Acs1 abundance was even 3.5-fold increased for the restrictive growth condition in comparison to the permissive growth condition and an impressive 6-fold increased abundance was observed when compared to the WT strain. Literature reports that overexpression of *ACS1* increases the production of the sesquiterpenoid amorphadiene in a corresponding *S. cerevisiae* production strain, which was also overproducing key enzymes of the mevalonate pathway.[95] Therefore, the observed high abundance of acetyl-CoA synthetase isoforms is likely to increase flux through the ergosterol biosynthetic pathway for growth-restricted Cdc48-psd^3 and bPAC cells, with beneficial effects on the recombinant production of isoprenoid-derived compounds.
For the growth-restricted Cdc48-psd^3 strain Hmg1 was found to be higher abundant in comparison to the WT strain. The HMG-CoA reductase isoform Hmg1 is predominantly responsible for catalytic activity in the mevalonate pathway under aerobic conditions and marks a rate-limiting step in ergosterol biosynthesis.[12] In numerous metabolic engineering approaches, a truncated construct of *HMG1* is overexpressed in order to increase the availability of FPP for sesquiterpene production.[53] [6] However, overexpression of full length Hmg1 was demonstrated to have a negative effect on ergosterol production and was found to be responsible for the formation of nucleus-associated arrays of stacked endoplasmic reticulum (ER) membranes.[69] Nevertheless, the mod-

erately increased abundance observed for Hmg1 may lead to higher fluxes through the mevalonate pathway for growth restricted Cdc48-psd^3 cells in comparison to the WT strain. However, this observation does not explain the higher β-carotene production of the growth-restricted Cdc48-psd^3 compared to the permissive growth condition, since similar Hmg1 abundances were observed for both conditions. In addition many proteins involved in ergosterol biosynthesis downstream FPP were among the DAPs for the Cdc48-psd^3 strain. For these proteins, strong abundance differences were observed in the comparison between Cdc48-psd^3 and the WT strain. In the comparison of restrictive and permissive growth condition for the Cdc48-psd^3 strain, the number of identified DAPs and overall abundance differences were significantly smaller. Nevertheless, each of the identified DAPs in the comparison to the permissive growth condition was found also in the comparison to the WT, while matching the respective abundance trend. Hence, strain-dependent abundance differences for proteins involved in ergosterol production for Cdc48-psd^3 and WT cells were further enhanced by the blue light-induced cell cycle arrest for Cdc48-psd^3. Notably, Erg9, which catalyzes the reaction of FPP to squalene and thus directly competes with isoprenoid synthesis via the recombinant pathway, was a high abundant DAP in the comparison between growth-restricted Cdc48-psd^3 and WT strain. Furthermore, Erg1 and Erg11 were found to be significantly more abundant in growth-restricted Cdc48-psd^3 cells compared to the WT strain, and for Erg11 this was also true when compared to the permissive growth condition. Erg1 and Erg11 are known to catalyze rate-limiting reactions in the synthesis of ergosterol.[54] Nevertheless, all three enzymes catalyze reactions downstream FPP and upregulation of these proteins should redirect metabolite flux towards ergosterol, but apparently did not have a negative impact on β-carotene yields for Cdc48-psd^3. Literature reports that Erg1, as well as Hmg1, is regulated by ERAD.[51] [69] For the Cdc48-psd^3 strain, ERAD is disrupted by the light-induced degradation of Cdc48-psd^3, which should lead to an accumulation of Erg1 and Hmg1. As revealed by the GO enrichment analysis, in general many proteins of the ER were highly abundant for growth-restricted Cdc48-psd^3 cells in comparison to the WT and to the permissive growth condition. This finding might also be linked to ERAD disruption under restrictive light conditions for the Cdc48-psd^3 strain.

For the bPAC strain only few proteins were identified as DAPs for the ergosterol biosynthesis superpathway in the comparison between bPAC grown under restrictive light conditions and the WT strain. As visualized by figure 3.1, abundance differences were rather small and DAPs were found to be equally distributed between high and low abundant. In the comparison of bPAC grown under restrictive and permissive light condition Erg11 was identified low abundant DAP. As mentioned above Erg11 catalyzes a rate-limiting step in the production of ergosterol and decreased abundance of this protein could lead to a upstream accumulation of FPP for growth-restricted bPAC cells. Together with the higher abundance of Acs1 mentioned above, this may indicate an increased capacity for β-carotene production for growth-restricted bPAC cells.

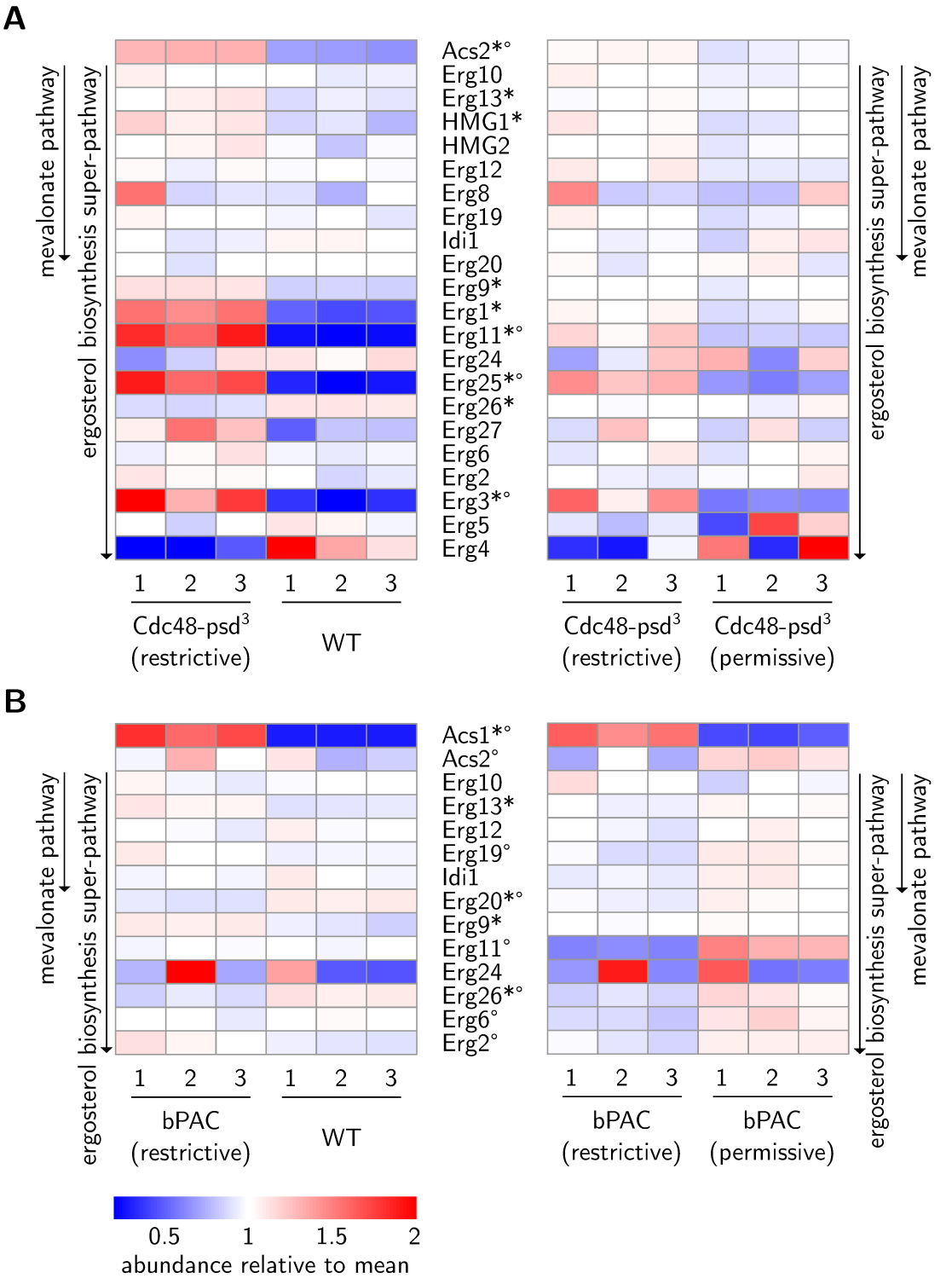

Figure 3.1: Heatmaps of protein abundances for proteins involved ergosterol biosynthesis for the Cdc48-psd^3 (**A**) and the bPAC strain (**B**). Proteins of each pathway are listed in the order of successive reactions. * DAP in the comparison of the CCM cultivated under restrictive growth conditions and the WT strain. ° DAP in the comparison of the CCM cultivated under restrictive and permissive growth conditions.

Upregulation of Acs1, TCA cycle and respiratory chain match cellular response of *S. cerevisiae* upon glucose starvation for the growth-restricted bPAC strain

Literature reports that *ACS1* expression is strongly repressed by glucose and that expression of *ACS2* is essential for growth on glucose.[62] [11] For *S. cerevisiae*, glucose sensing and cellular responses to glucose are regulated in a complex manner trough the interplay of two PKA dependent pathways regulated by cAMP, the Rgt2/Snf3-Rgt1 pathway regulating glucose uptake and the main glucose repression circuit regulated by the kinase Snf1.[18] In *S. cerevisiae*, cAMP production is activated by the availability of glucose[98] and for growth-restricted bPAC cells, glucose signaling via cAMP is disrupted by the inactivation of the light-dependent adenylate cyclase in darkness. Strikingly, thereby the observed upregulation of Acs1 matches the cellular response of *S. cerevisiae* upon glucose starvation described by literature.[62]

Expression of *ACS1* is mediated by the transcription factors Adr1 and Cat8, which are both required for derepression of the gene.[61] Although expression of *CAT8* is reported to be repressed by glucose in a cAMP dependent manner and that activity of the PKA subunit Tpk1 decreases *CAT8* expression, the authors point out that their data supports a redundant regulation mechanism in regard to glucose repression,[113] while other sources report that the protein kinase Snf1 determines Cat8 activity.[76] Furthermore, activity of Adr1 was also found to be negatively regulated by PKA during growth on glucose, although the regulation mechanism involving Snf1 remains poorly understood.[18] For bPAC grown under restrictive light conditions, most gene products for genes regulated by Cat8 or Adr1 were identified as high abundant DAPs (data shown in table 5.26 in the appendix section). This observation emphasizes the assumption that both transcription factors are active for the bPAC strain under restrictive growth conditions, which is usually only the case after diauxic shift, when glucose is depleted and energy is generated by the aerobic oxidation of nonfermentable carbon sources.[110]

Furthermore, as shown in section 2.2.2.6, the analysis of protein abundances involved in pathways of the central metabolism revealed that for the bPAC strain, almost every protein of the TCA cycle and the respiratory chain was higher abundant for growth-restricted bPAC cells in comparison to the permissive condition and to the WT strain. Remarkably, transcription of genes for both pathways is also reported to be repressed by glucose and the observed upregulation of both pathways matches the cellular state after diauxic shift, already described above.[108] [76] [40] Most of the genes are positively regulated by the transcription co-activator Hap4 but the transcription factors Cat8 and Mig1 are also reported to be involved.[14] Interestingly, literature reports that cAMP induces mitochondrial compartment biosynthesis, which is in contrast to the findings described above, as cAMP production is halted for growth-restricted bPAC cells and high abundant mitochondrial proteins were observed nevertheless.[109] However, in the experiment described by the publication, intracellular cAMP levels were artificially increased by the

addition of cAMP to the media and a cellular state of growth restriction by cAMP depletion was not examined. Furthermore, for a temperature sensitive Cyr1 mutant strain, Mitsuzawa *et al.* reported impaired growth on nonfermentable carbon sources and on low concentrations of glucose for the permissive growth condition, which already exhibited low intracellular cAMP concentrations.[75] As these findings imply low respiratory capacity for *S. cerevisiae* at decreased cAMP levels, once again respiratory capacity during growth restriction was not examined by the authors. For growth restriction induced by PKA inactivation, literature reports contradictory effects on the *S. cerevisiae* metabolism either a state with increased respiratory capacity or a quiescence-like state.[40] [39]
In regard to glycolytic proteins, hexokinase II (Hxk2) and both subunits of the phosphofructokinase (Pfk1 and Pfk2) were found to be 20 % lower abundant for growth-restricted bPAC in comparison to permissive condition, but only Pfk1 was found to be lower abundant in comparison to the WT. This finding underlines the metabolic shift towards respiratory energy generation observed for growth-restricted bPAC strain. However, at this point it should be noted that conclusions drawn within this section originate from a single proteomics experiment and a validation of these highly interesting results should be considered.

Cell cycle restricted Cdc48-psd^3 cells show downregulation of two PKA subunits in comparison to the WT strain

Growth restricted Cdc48-psd^3 cells showed a moderate downregulation of the two catalytic PKA subunits Tpk1 and Tpk2 in comparison to the WT, whereas the third subunit Tpk3 and the regulatory subunit Bcy1 were not included in the dataset of the proteomics experiment. This observation might imply a link between the Cdc48-psd^3 and the bPAC strain as PKA dependent cellular processes might be affected for Cdc48-psd^3 cells as well. Nevertheless, the outcome of the proteomics experiment did not provide evidence for this assumption for growth-restricted Cdc48-psd^3, at least in regard to the observed changes induced for the central metabolism described above. Here, Acs2 was among the high abundant DAPs in both comparisons, implying glucose repression of *ACS1*. Furthermore, the PKA subunits were only found of low abundance for growth-restricted Cdc48-psd^3 in comparison to the WT strain and not in comparison to the permissive growth condition. This finding suggests a strain-dependent effect that is independent of the proteome changes induced by growth restriction.

Increased cordycepin yields could be explained by decreased Pho8 abundance for growth-restricted Cdc48-psd^3 cells and by autophagy for cAMP-deficient yeast strains

The phosphatase Pho8 involved in depletion of the cordycepin precursor 3'AMP was identified as low abundant DAP for growth-restricted Cdc48-psd^3 in comparison to the

WT, thereby potentially increasing the availability of 3'AMP for cordycepin production.[52] However, Pho8 was also found as a high abundant DAP for growth-restricted Cdc48-psd^3 in comparison to the permissive condition. Interestingly, Pho8 was also among the 82 identified DAPs in the comparison of WT cells cultured exposed to blue light (restrictive condition for Cdc48-psd^3) and in darkness (permissive condition for Cdc48-psd^3) and was found to be higher abundant for WT cells cultured under blue light conditions. Differences in abundance between both light conditions were similar for the Cdc48-psd^3 and the WT strains (data not shown). This implies an effect caused by the cultivation/light condition, unaffected by growth restriction for the Cdc48-psd^3 strain. Nevertheless, since Pho8 abundance was still lower for the growth restricted Cdc48-psd^3 strain in comparison to the WT strain, the increased cordycepin production observed by Dr. Johannes Scheffer[92] could be explained by this finding. Here, expression of *CNS1* and *CNS2* was under the control of a blue light dependent transcription factor, which prevents a direct comparison of cordycepin yields for the permissive and restrictive condition. However, a comparison between the two light conditions would be interesting to determine whether Pho8 availability is responsible for the observed higher cordycepin yields, since even higher yields would be expected under the permissive growth condition. For the bPAC strain, Pho8 was found to be high abundant in growth-restricted bPAC cells in comparison to the permissive growth condition and no significant abundance difference was observed in the comparison of growth-restricted bPAC cells to the WT strain. This implies no beneficial effect in regard to cordycepin production for the growth-restricted bPAC strain based on Pho8 abundance. Nevertheless, for the strain yJT42 which exhibits decreased intracellular cAMP concentrations under blue light conditions, higher cordycepin production was observed within the present work in comparison to the parental cordycepin production strain yBP03. For the generation of the yJT42 strain, the photosensitive degron psd^{AS} was fused to Cyr1, which enables blue light dependent degradation of the endogenous adenylate cyclase. As reported by Sophia Hasenjäger $\approx 40\,\%$ of cellular Cyr1-psd^{AS} is degraded under blue light conditions, which results in decreased cAMP production and lower PKA activity for yJT42.[100] Accordingly, Dr. Jonathan Trauth showed that degradation of Cyr1-psd^{AS} by blue light leads to accumulation of glycogen in the cell, which is a well known response of *S. cerevisiae* to low cAMP levels.[100] [32] He also observed that cells of growth-restricted bPAC cells accumulate more glycogen than yJT42 cells, which indicates higher cAMP levels for the yJT42 strain cultured under restrictive growth conditions in comparison to the bPAC strain.[100] Interestingly, literature reports that inactivation of PKA induces autophagy, which might be an explanation for the increased cordycepin production observed for the yJT42 strain, as 3'AMP is reported to be generated by autophagy.[96]

Further remarks on the proteomics analysis

From the proteomics analysis, increased abundance of an acetyl-CoA synthetase isoform was identified as the main explanation for the increased β-carotene production observed for the growth restricted Cdc48-psd^3 strain. The increased β-carotene yields reported by Dr. Christof Taxis were obtained for the Cdc48-psd^3 strain cultured under alternating intervals of restrictive and permissive light conditions. In contrast, only a small increase in β-carotene fluorescence was observed for Cdc48-psd^3 cultured exclusively under restrictive light conditions in the production phase.[92] This finding implies, that consecutive induction of growth restriction and release from this cellular state favors the accumulation of β-carotene within the cell for the Cdc48-psd^3 strain and not only the growth-restricted condition by itself. Therefore, the analyzed state of growth restriction might only partially explain the reasons for the observed increased β-carotene yields and the transition from growth restriction to the permissive condition should be further investigated in order find explanations for the increased β-carotene production.
However, increased β-carotene yields were observed by Dr. Jonathan Trauth for the bPAC strain cultured for 24 h under restrictive light conditions.[100] Here, in addition to the increased abundance of Acs1, a shift towards higher respiratory capacity was observed at the proteome level for the growth-restricted bPAC strain. Higher abundances of proteins involved in the TCA cycle and the respiratory chain might lead to an increased energy availability for growth-restricted bPAC cells, as glucose is presumably still available in the medium and glycolytic activity could be complemented by an enhanced respiratory capacity. Nevertheless, abundances of key glycolytic enzymes were found to be lower for the bPAC strain cultured under restrictive conditions in comparison to the permissive condition. Ergosterol biosynthesis is highly energy intensive, as the synthesis of a single ergosterol molecule consumes at least 24 molecules of ATP and 16 equivalents of NADPH.[51] Many of the ATP and NADPH consuming steps are part of the mevalonate pathway, which provides the cell with FPP for β-carotene production. Hence, the observed higher β-carotene yields may result from an increased respiratory capacity for the growth-restricted bPAC strain, providing the cell with more energy for β-carotene production.
In general, the tuneable intracellular cAMP levels make the bPAC strain a very interesting tool for studying of PKA-dependent processes in *S. cerevisiae*, since cAMP concentrations can be adapted to the full range of physiological concentrations and beyond by adjusting light intensity. Here, phosphorylation of PKA targets could be examined by mass spectrometry, which would require enrichment of phosphopeptides prior to analysis. Noteworthy, observed changes of protein levels do not necessarily have to correlate with flux through corresponding pathways as posttranslational modifications, subcellular localization and feedback inhibition of enzymes play a role in regulating the metabolism.[81] [91] As an example for the ergosterol biosynthesis superpathway, many Erg enzymes down-

stream FPP (Erg1, Erg7, Erg27 and Erg6) are reported to dual localize in the ER and in lipid particles and localization was found to determine enzymatic activity.[54] Nevertheless, protein localization and the other mentioned forms of posttranslational regulation cannot be examined based on the obtained proteomics dataset.
Another explanation for the high product yields observed for the growth-restricted CCM strains might be that cell cycle arrest by itself is a favorable cellular state for the production of molecules in the context of metabolic engineering. During growth restriction, energy and precursor flux could be redirected towards the recombinant pathways, which would otherwise sustain proliferation under permissive growth conditions. In further consequence, this raises the question whether observed beneficial production capacities for growth-restricted cells have to become directly apparent from the proteomics analysis or whether energy availability and metabolic fluxes are substantially different for a given state of the proteome during cell cycle arrest in comparison to the permissive growth condition and the WT strain.

Proteomics data analysis – An interplay of several software parameters define the outcome of the LFQ experiment

The outcome of the proteomics experiment was strongly influenced by the settings applied for *Label Free Quantification* (LFQ) during *PEAKS* analysis. Manually adjusted parameters were quality and average area thresholds, which were set according to the guidelines published by the software manufacturer. Appropriate filtering removes false positives from the analysis and thereby is key for a successful outcome of the proteomics analysis. Nevertheless, for unknown reasons data quality was noticeably different for the bPAC strain in comparison to the two other CCM yeast strains, which allowed stricter filtering criteria and resulted in higher data quality for the bPAC strain.
Furthermore, obtained results were normalized by default to the total ion current (TIC) of the samples. Aside from normalizing to TIC, the *PEAKS* software package offers customized normalization e.g. to abundance of an internal standard protein. Hence, normalization of the proteomics data to a representative set of proteins could be considered. Nevertheless, abundances of the reference proteins would need to be unaffected by the optogenetic manipulation of the cell cycle and in the comparison of CCM and WT strain, or would otherwise lead to an undesirable bias during the analysis.
Within the context of a master student internship, the obtained data was reprocessed using the proteomics software *MaxQuant* with similar analysis parameters. The obtained LFQ results were compared based on relative protein abundance and it was found that both analyses were very similar, although a larger number of proteins were identified in the *MaxQuant* analysis, probably due to different filtering criteria (see figure 5.1 in the appendix section). Unlike the *PEAKS* software package, *MaxQuant* is open source, free of charge and the analysis pipeline was successfully set up on hardware operated by the

research group of Prof. Dr. Essen, which might facilitate processing of proteomics data for future experiments.
Furthermore, the applied DAP criteria were crucial for GO enrichment analyses, which rely on a representative list of DAPs in order to generate meaningful GO-terms. Accordingly, the Student's t-test (p-value < 0.01) introduced an objective DAP criterion for the identification of proteins with significantly different abundance between both sample groups. In addition, the abundance difference threshold was reasoned to eliminate proteins from the list of DAPs, which were exhibiting abundance differences of less than 10 % and were thereby unlikely to have a major impact on cellular processes. Moreover, this criterion eliminates minor systematic deviations of the analysis e.g. due to normalization. For the Cdc48-psd^3 and bPAC strain this criterion excluded only 0.4 – 2.7 % of the DAPs from the pairwise comparisons. However, for the Clb2$^{\Delta DB}$-psd^3 strain up to 24 % of the DAPs were eliminated from the analysis due to the rather small abundance differences in the comparisons for this particular strain.
The visible pattern in duplicate measurements in the heat maps is likely due to the quantity of samples measured, which meant that each technical replicate was measured four days after the first replicate. Presumably the condition of the sample or instrument has changed in the meantime, causing the abundance pattern. However, mean protein abundances between biological replicates were unaffected, and the observed artifact should not have had a major impact on the outcome of the experiment. Although no comparable artifacts were observed by the mass spectrometry facility again, precautionary measures should be taken for further measurement series. Therefore, each future sample set for separate CCM strains should be measured in separate batches to ensure comparable sample and instrument conditions. In addition, samples should only be loaded into the autosampler shortly before the measurement, since the autosampler for the timsTOF instrument cannot be cooled.

3.3 Bioanalysis for Production Strain Establishment

Advanced bioanalysis was applied for establishment of production strains within the MELICOMO project. In the following section current state and future perspective in regard to the metabolic engineering process will be discussed.

Cordycepin production in *S. cerevisiae*

As described by section 2.3.2, cordycepin and 3'AMP were successfully quantified from cultures of corresponding production strains by LC-MS. Nevertheless, strains expressing *CNS3* variants were found to increase intracellular 3'AMP concentrations in a blue light independent manner, despite *CNS3* expression was supposed to be regulated by the blue light dependent transcription factor LexACry2/Cib1-VP16. Hence, light dependent

regulation of CNS3 could be targeted in future studies, as steady 3'AMP production might impose a metabolic burden on the organism. Additionally, the truncated *CNS3* constructs, which were generated by Bastian Pook to eliminate Cns3 derived pentostatin production may be further improved. Recently, a high quality *AlphaFold* structure prediction of Cns3 became available (entry G3JF10). The 3D-model exhibits two distinct domains for Cns3 and truncation based on this model would rationalize gene editing. Accordingly, expression of a corresponding finalized *CNS3* construct in dedicated cordycepin production strains might substantially increase 3'AMP availability for cordycepin production. This should be the case, not only in terms of concentration but also in regard to spatial distribution. 3'AMP is reported to be generated during RNA autophagy in the vacuole by the RNase Rny1, where the nucleotide is exposed to dephosphorylation by Pho8.[106] Hence, a source of cytosolic 3'AMP produced by *CNS3* is likely to substantially increase the amount of cordycepin produced by the cell.

Within the present work, cordycepin was quantified from media samples and could not be detected in cell extracts. This finding implies that cordycepin is excreted from the cell in the same way as other nucleosides during bulk RNA degradation.[52] In the cytosol cordycepin is phosphorylated by the adenosine kinase Ado1 and the enzyme would be a promising target for light-induced degradation.[49] This way inactivation of Ado1 would have two main beneficial effects on the production of cordycepin. It would increase the amount of available cordycepin by preventing its conversion into cordycepin-monophosphate and would also limit the cellular toxicity of cordycepin by suppressing the downstream formation of cordycepin-triphosphate, which perturbs RNA synthesis by terminating chain elongation and disturbance of polyadenylation.[49]

As shown in section 2.3.2, cordycepin yields were higher for the yJT42 strain in comparison to the yBP03 strain and significantly more cordycepin was produced by both yeast strains under blue light conditions. Nevertheless, a considerable amount of cordycepin was already detected in darkness for each production strain, which means leaky expression of *CNS1* and *CNS2* mediated by the blue light dependent transcription factor LexACry2/Cib1-VP16. These observations are in line with the results of a corresponding LC-MS experiment reported by Dr. Jonathan Trauth.[100] For the yJT42 strain, the photosensitive degron psd^{AS} is fused to Cyr1, which enables degradation of the endogenous adenylate cyclase under the blue light conditions. Therefore exposure of yJT42 to blue light decreases intracellular cAMP levels and reduces PKA activity. Hence, the observed increased cordycepin yields could be due to the release of 3'AMP by autophagy, which is reportedly induced by PKA inactivation.[96] Furthermore, significant variations in cordycepin production were observed for biological replicates of yJT42 within the present work. As *CYR1-psd*^{AS}, *CNS2* and the blue light sensitive transcription factor are already integrated into the genome for the yJT42 strain, integration of *CNS1* might be necessary in order to decrease these variations.

For the yJT42 strain cultured under blue light conditions cordycepin concentrations in

culture media were determined in a range of 1.9 – 3.7 mg/L. As cordycepin yields are expected to increase substantially for more advanced production strains, it should be noted that cordycepin is reported to decrease growth of *S. cerevisiae* at concentrations higher than 20 mg/L.[49] Thus, as described above, blue light controlled degradation of Ado1 may be necessary in order to maintain cellular functions of *S. cerevisiae* during the production phase. However, since the analyzed *S. cerevisiae* strains demonstrate light controlled cordycepin production as proof of principle, there is still a long way to go before the process becomes commercially viable as literature reports cordycepin yields of ≈ 1 g/L in fermentations using the edible fungus *Cordyceps militaris*.[115]

GA_4 production in *S. cerevisiae*

Within the present work, GA_4 was detected in culture media of corresponding production strains at concentrations of ≈ 200 ng/L. Hence, GA_4 synthesis via the recombinant production pathway was successfully established during the MELICOMO project. However, obtained product yields were very low, which implies that there are still major obstacles to overcome during the metabolic engineering process.

However, GA_4 production as proof of concept is already a big accomplishment, as GA_4 production from GGPP in *S. cerevisiae* requires the interplay of six recombinant plant enzymes and reduction of the heme cofactor for the involved cytochrome P450 monooxygenases by a recombinant plant reductase. In plants, the nonpolar GA_4 intermediate *ent*-kaurene is synthesized in plastids, oxidized in the ER and subsequently further modified in the cytosol in order to yield GA_4.[44] As plastids are absent in yeast, targeting corresponding pathway enzymes to appropriate cell compartments is key for the reassembly of the GA_4 synthesis machinery in *S. cerevisiae*. For the present GA_4 production strains, targeting of pathway enzymes to specific cell compartments by signal peptides has not yet been addressed. Furthermore, fluorescence microscopy performed by Dr. Johannes Scheffer did not conclusively clarify the localization of all pathway proteins.[92] Clarification of the localization of the pathway enzymes and subsequent modifications of signal peptides might be worth considering especially in order to achieve co-localization of the *ent*-copalyl diphosphate synthase, the *ent*-kaurene synthase and the *ent*-kaurene oxidase, which are targeted to plastids in plants and modify highly hydrophobic GA_4 precursors.

Moreover, it is described that a specific redox partner is necessary for the full activity of P450 monooxigenases and that expression of a reductase originating from the same plant as the target P450 monooxigenase can improve product yields.[29] [22] Hence, reduction of the *Ps*KAO2 heme cofactor could be a bottleneck for GA_4 production and the *ent*-kaurenoic acid oxidase should be substituted by *At*KAO, as the expressed cytochrome P450 reductase originates from *Arabidopsis thaliana* for the current GA_4 production strain.

In the next optimization cycles, targeted metabolic analyses might help to identify bottlenecks in the recombinant GA_4 pathway, thereby rationalizing future strain optimization. However, even though state of the art instrumentation for metabolomics analyses is available at Philipps University Marburg, some of the intermediates cannot be acquired commercially, rendering accurate quantification troublesome.
In addition to further increase the availability of the GA_4 precursor GGPP, overproduction of *Xd*CrtE should be considered for the GA_4 production strain. This modification has already been established for the β-carotene strain and might further increase GA_4 yields. Dr. Jonathan Trauth also implemented two additional genetic modifications for the β-carotene strain, which are reported to increase β-carotene yields and should also have a beneficial effect on GA_4 production. He overproduced the truncated HMG-CoA reductase tHMG1 to increase the flux through the mevalonate pathway and enabled blue light dependent degradation of Erg9, which converts FPP to squalene during ergosterol biosynthesis.[100] [50] Aside from that, blue light dependent expression of the pathway genes is already envisaged and can be fairly easily implemented by substitution of the LexA-EDLL transcription factor with LexACry2/Cib1-VP16.
Recently, Kildegaard *et al.* reported GA_4 production of up to 17 mg/L for the oleaginous yeast *Yarrowia lipolytica* via a biosynthetic pathway closely related to the metabolic engineering approach described in the present work.[58] The corresponding production strain ST8602 expressed *AtCPS*, *AtKS*, *AtKO* and *AtATR2* for the synthesis of *ent*-kaurenoic acid and the *Fusarium (Gibberella) fujikuroi* genes *Gf*P450-1 and *Gf*P450-2 for the conversion of *ent*-kaurenoic acid into GA_4. In addition, the P450 auxiliary proteins *Gf*Cyb5, *Gf*CybRed, *Gf*CPR and *Yl*Cyb5 were produced by ST8602. All non-native genes were codon-optimized for the expression in *Y. lipolytica* and several modifications were applied to the production strain in order to increase the availability of the GA_4 precursor GGPP. Here, an additional copy of the native GGPP synthase *Yl*GGPPS and the *Synechococcus sp.* GGPP synthase *Ss*GGPPS7 as well as the native truncated HMG-CoA reductase tHMG were produced by the strain. Furthermore, the endogenous squalene synthase was downregulated by truncation of the promoter sequence. However, the authors were not able to detect GA_4 for the strain ST6513, which basically reassembled the biosynthetic pathway established during the MELICOMO project by the expression of *AtCPS*, *AtKS*, *AtKO*, *AtKAO*, *AtATR2*, *AtGA3ox* and *AtGA20ox*. In any case, the publication documents an impressive process of metabolic engineering not only limited to the production of GA_4, as strains for the production of GA_3, GA_7, GA_4, GA_9, and GA_{12} were also established. Here, additionally the deletion of the signal peptides for *At*CPS, *At*KS and *At*KO, as well as expression of the fusion construct *AtCPS/KS* led to significantly increased product yields.

3.4 Final Remarks

Present biochemistry and especially metabolic engineering approaches rely heavily on sensitive methods and powerful software tools in order to evaluate progress of work. State-of-the-art instrumentation provided by the mass spectrometry facility of Philipps-University Marburg enabled the corresponding analyses in the first place. Here, the Bruker timsTOF Pro mass spectrometer was used to examine the influence of cell cycle arrest on the proteome for different *S. cerevisiae* CCM strains and workflows for sample preparation, data analysis and visualization were developed within the present work. In terms of small molecules, the Agilent 6470 triple quadrupole mass spectrometer allowed precise quantification of analytes in the nM range. More recently a Thermo Scientific Q Exactive instrument was put into operation by the mass spectrometry facility, which is an major upgrade over the Thermo Scientific LTQ-FT Ultra mass spectrometer used within the present work. The new instrument is used by the service facility to process routine MS requests and should thereby provide in-depth small molecule analysis, even for users without hands on experience in mass spectrometry.

Once product yields are sufficiently increased for corresponding production strains, MS based quantification should be replaced by HPLC analysis, which would allow analyte quantification on instruments readily accessible for members of the research group of Prof. Dr. Essen. At this point upscaling of the biomass production could be considered using the Infors HT Labfors 5 Lux bioreactor, which was already successfully utilized for optogenetic experiments performed by Dr. Simona Gramazio.[38]

In summary, metabolic engineering was applied with great success in the MELICOMO project to implement recombinant metabolic pathways in *S. cerevisiae* and to establish several optogenetic tools to increase the product yields for corresponding production strains. In this context, the analytical workflows described by the present work played an important role in the characterization of modified yeast strains and in the quantification of target analytes.

Chapter 4

Methods and Materials

4.1 Biomass Analysis

4.1.1 Cell Cultivation for Biomass Analysis

Cultures of Clb2$^{\Delta DB}$-psd^3 (ESM356-1 + pDS229) grown under restrictive (dark) conditions and the corresponding WT (ESM356-1 + pRS315), were produced in 2 L scale. For each strain three biological replicates were grown and the experiment was conducted three times in order to generate sufficient material for subsequent biomass analysis. For starter cultures 3x 0.2 L LFM were inoculated with Clb2$^{\Delta DB}$-psd^3 and WT cells from agarose plate and grown overnight under blue light conditions (465 nm, 30 $\frac{\mu mol}{m^2 \cdot s}$, 100 rpm, 30 °C). The next day biological replicates were diluted 1:10 in LFM (final volume: 10x 200 mL in TC-flasks for Clb2$^{\Delta DB}$-psd^3 and 2 L for WT) and the cells were grown for 3 h (465 nm, 30 $\frac{\mu mol}{m^2 \cdot s}$, for Clb2$^{\Delta DB}$-psd^3, in darkness for WT cultures, 100 rpm, 30 °C). Afterwards Clb2$^{\Delta DB}$-psd^3 cultures of the same biological replicate were combined and Clb2$^{\Delta DB}$-psd^3 and WT were cultivated for additional 24 h in darkness (100 rpm, 30 °C). Cells were harvested in JA-10 tubes (4 °C, 2000 rpm, 20 min), resuspended in 40 mL *dd*H_2O and spun in a Falcon centrifuge (2000 rpm, 4°C, 10 min). Obtained Cell pellets were freeze dried over 36 h using a lyophilizer, further dried for 24 h at 50 °C and stored in a desiccator until usage.

4.1.2 Protein Quantification (Biuret assay)

Protein content of dry cell mass or wet cell mass was determined using the Biuret method. Here, the protocol described by Lange *et al.* was modified for usage in 96-well plates.[64] For the determination of protein content from dry mass cells were resuspended at a concentration of 8 mg/mL in *dd*H_2O. For protein determination from wet cell mass, cultures were spun using a Falcon centrifuge (2000 rpm, 4 °C, 5 min), washed with 0.9 % NaCl solution (2000 rpm, 4 °C, 5 min) and resuspended in *dd*H_2O to a concentration of 25 mg/mL. For standards, BSA dried O/N at 50 °C was dissolved in *dd*H_2O and diluted

to a range of standards from 0.2 to 5 mg/mL. The Biuret method was applied equally to cell suspensions and standards assayed in triplicate. To 200 µL sample solution 100 µL of 1 M NaOH were added and incubated for 10 min at 100 °C. The sample was cooled on ice, spun (13000 rpm, RT, 5 min) and vortexed after adding 100 µL 0.1 M $CuSO_4$. The suspension was incubated for 5 min at RT and spun (14000 rpm, 5 min, RT). From the clear supernatant 300 µL was transferred into wells of a 96-well plate and absorption at $\lambda = 550$ nm (9 nm bandwidth, 25 reads/well) was measured using a Tecan Infinite 200 microplate reader.

4.1.3 Protein Quantification (Bradford assay)

The Bradford assay is compatible with 6 M urea[1] which allows protein quantification from the supernatant after cell lysis during the proteomics workflow as described in section 4.2.2. Disadvantageous to this protocol is that only solubilized protein is determined and can not be used for full cell protein quantification, including proteins of the cell debris after lysis. Proteins are determined within a linear range for BSA of 0.05 - 0.5 mg/mL.[2]

In preparation for the assay on 96-well plates Dye Reagent Concentrate was diluted 1:5 with *dd*H_2O and protein standards from dried BSA (50 °C, O/N) were prepared in 1 M urea. 25 µL of the spun cell lysate (8 M urea) were diluted with 175 µL *dd*H_2O to a final concentration of 1 M urea. Samples and standards were assayed in triplicate. From the sample solutions 10 µL were transferred into wells of a 96-well plate and 200 µL diluted Dye Reagent were added and thoroughly mixed. After incubation for 10 min at RT absorption at $\lambda = 595$ nm (9 nm bandwidth, 25 reads/well) was measured using a Tecan Infinite 200 microplate reader.

4.1.4 Determination of Amino-acid Composition

The amino-acid composition of *S. cerevisiae* proteins was determined according to EU Commission Directive 98/64/EG via oxidative, acidic and alkaline protein hydrolysis. Experiments were performed under supervision of Jenny Ahlborn, PhD student of the group of Prof. Dr. Zorn at Justus Liebig University Giessen.

Cysteine and methionine content was determined after oxidative treatment and acidic protein hydrolysis. Here 200 mg dried cells were treated with 5 mL freshly prepared phenolic performic acid solution (4.5 mL of 88.9 % formic acid, 0.473 % phenol, activated for 1 h at RT with 0.5 mL of 30 % hydrogen peroxide and kept on ice for 15 min afterwards) and the reaction mixture was incubated for 16 h in an ice bath. Afterwards the reaction was quenched with 0.84 g sodium pyrosulfite, 25 mL of 6 M HCl, 0.1 % phenol were added and the sample was incubated for 24 h at 110 °C. After cooling the sample in an ice bath, 20 mL of 7.5 M NaOH were gently added and the pH of the suspension

was adjusted at RT with 7.5 M and 1 M NaOH to 2.2. To the suspension 0.12 M phenolic citrate buffer (pH 2.2, 0.2 % phenol) was added to obtain a final volume of 200 mL and 1 mL was filtered using a syringe filter.
Total amino-acid content was determined after acidic protein hydrolysis, without prior treatment with performic acid. Here 200 mg dried cells were resuspended in 25 mL of 6 M HCl, 0.1 % phenol and the amino-acid sample was prepared as described above.
Tryptophan content was determined after alkaline protein hydrolosis. Accordingly, 200 mg dried cells were resuspended in phenolic NaOH (5 M, 0.1 % phenol) and the suspension was incubated for 24 h at 110 °C. After cooling in a water bath, 10 mL of 0.5 M phosphoric acid were added and pH was adjusted to 2.2 using 3.75 and 1 M HCl. To the suspension 0.12 M phenolic citrate buffer (pH 2.2, 0.2% phenol) was added to obtain a final volume of 200 mL, of which 1 mL was filtered using a syringe filter.
Amino-acid samples were derivatized by ninhydrin and measured using a S 433 amino-acid analyzer (*SYKAM*) equipped with a LCA K13 cation exchange column and a LCA K04 ammonia filtration column. During analysis a gradients of 0.12 M sodium citrate, pH 3.45 (buffer A) and 0.2 M sodium citrate/borate pH 10.85 (buffer B) was used to elute the amino-acids obtained from oxidative/acidic and alkaline protein hydrolysis at a flow rate of 0.45 mL/min. Furthermore 0.5 M NaOH, 0.2 g/L EDTA was used to recondition the system. Ninhydrin reagent for the derivatization of the amino-acids after separation ($T_{reactor} = 130$ °C) was supplied at a flow rate of 0.25 mL/min. Gradient parameters of the analysis are summarized by tables 5.10 to 5.12 in the appendix section. Derivatized proline was measured at $\lambda = 440$ nm and all other amino-acid ninhydrin derivates were measured at $\lambda = 570$ nm. Amino-acids were quantified via one-point calibration. For the calculation of protein content the molar mass of amino-acids minus water was used, representing their condensation products.

4.1.5 Carbohydrate Quantification

Carbohydrates were quantified as described by Masuko *et al.*[73] Accordingly dry cells were resuspended in *dd*H_2O at a concentration of 0.3 mg/mL and standards were prepared from dried glucose (50 °C, O/N) at a concentration of 0.2 - 1.8 mM. Cell suspensions and standards were assayed in triplicate. From the samples 50 µL were pipetted into the wells of a 96-well plate, 150 µL of 96 % H_2SO_4 were added to the sample and directly afterwards 30 µL of 5 % Phenol in *dd*H_2O were added. The 96-well plate was incubated for 5 min at 90 °C in a water bath and cooled down to RT using a water bath afterwards. The 96-well plate was wiped dry and absorption at $\lambda = 490$ nm (9 nm bandwidth, 25 reads/well) was measured using a Tecan Infinite 200 microplate reader. For the calculation of carbohydrate content the molar mass of glucose minus water was used, representing its condensation product.

4.1.6 DNA and RNA Quantification

DNA and RNA were quantified using the Schmidt-Thannhauser-Schneider method as described by Herbert *et al.*[47] Here acid-soluble material is removed from the cellular material in a first step, followed by RNA extraction under alkaline conditions and the extraction of DNA by the treatment with hot acid. RNA was quantified directly from the extracts and DNA after treatment with diphenylamine reagent as described by Borton.[17]

From each aliquot of freeze dried cells 3x 20 mg were resuspended in 1.6 mL of 0.25 M $HClO_4$ respectively, briefly vortexed and incubated for 13 min on ice. Suspensions were spun (9000 rpm, 4 °C, 2 min) and after discarding the supernatant, the wash step was repeated.

In order to extract RNA 1.6 mL of 0.3 M KOH were added to the cell pellet, briefly vortexed and incubated for 2 h at 37 °C. The suspension was acidified by adding 200 µL of 4.2 M $HClO_4$ and incubated for 5 min on ice. The suspension was spun (13000 rpm, 4 °C, 3 min), 800 µL of the supernatant were transferred into a fresh reaction cup, the remaining supernatant was discarded and the pellet was kept for subsequent DNA extraction. From the extracts 360 µL were neutralized with 250 µL of 0.3 M KOH, incubated for 5 min at RT, spun (13000 rpm, RT, 2 min) and supernatants were stored for RNA quantification.

DNA was extracted by adding 1.8 mL of 0.5 M $HClO_4$ to the pellet after RNA extraction and incubating for 15 min at 70 °C. Suspensions were spun (13000 rpm, 4 °C, 1 min), 800 µL of the supernatant were transferred to fresh reaction cups and the remaining supernatant was discarded. The pellet was briefly vortexed in 800 µL ice-cold 0.25 M $HClO_4$, the suspension was spun (13000 rpm, 4 °C, 1 min) and the supernatant was discarded. DNA extraction was repeated twice and the extracts were stored for later usage.

Calibration standards for RNA quantification were prepared from a stock solution of RNA dissolved in 50 mM KOH. The stock solution was diluted with *dd*H_20 and 1 M KOH to obtain 400 µL standards of a concentration range from 150 - 600 µg/mL RNA in 0.3 M KOH. Standard solutions were incubated for 2 h at 37 °C, afterwards acidified with 50 µL of 4.2 M $HClO_4$, incubated for 5 min on ice and spun (13000 rpm, 4 °C, 3 min). Subsequently 360 µL were neutralized with 250 µL KOH, incubated for 5 min at RT, spun (13000 rpm, RT, 2 min) and the supernatant was transferred into a fresh reaction cup. Absorption of diluted calibration standards (1:10) and samples (1:20) was determined at $\lambda = 260$ nm (5 nm bandwidth, 25 reads/well) from 300 µL solution in a UV-transparent 96-well plate using a Tecan Infinite 200 microplate reader. Furthermore RNA recovery experiments were performed by analyzing yeast samples extracted with 1.6 mL of 0.3 M KOH containing 600 µg RNA and comparing the results to cells extracted following the protocol described above.

DNA was solubilized in 50 mM KOH and diluted with *dd*H_20 to obtain standards of 4 -

50 µg/mL DNA. For standards triplicates of 250 µL were supplemented with 250 µL of 1 M $HClO_4$ respectively and incubated for 15 min at 70 °C. 210 µL of each standard were treated with 210 µL diphenyl reagent (1.5 g diphenylamin and 1.5 mL H_2SO_4 in 100 mL HAc, freshly completed with 5 µL of 1.6 % aqueous acetaldehyde per mL reagent) for 20 h at 30 °C. For samples of cell extracts 70 µL of the three consecutive DNA extracts were pooled, 210 µL diphenylamin reagent were added and the mixture was incubated for 20 h at 30 °C. Afterwards the samples and standards were spun (4000 rpm, RT, 1 min), 300 µL were transferred into wells of a 96-well plate and absorption was measured at $\lambda =$ 595 nm (9 nm bandwidth, 25 reads/well) using a Tecan Infinite 200 microplate reader. Furthermore recovery of DNA was analyzed by adding 15 µL of 2 mg/mL DNA stock to the pellet before DNA extraction.

4.1.7 Lipid Quantification

Lipids were determined gravimetrically from extracts of cells digested by lyticase. To obtain sufficient biomass for each strain , 40 mg freeze dried cells were pooled for biological triplicates. The cells were thoroughly mixed, and distributed to glass tubes in 3x $\sim$100 mg aliquots for each strain. Cells were resuspended in 1 mL lyticase buffer (50 mM Tris/HCl, pH 7.5, 10 mM EDTA, 0.3 % β-mercaptoethanol) supplemented with 0.85 mg/mL lyticase (20 U/mg) and incubated in a thermo-shaker (200 rpm, 37 °C, 1.5 h). The suspension was frozen in liquid nitrogen and lyophilized over night. At the next day the lysed cells were extracted as described by Henriksen *et al.*[45] Accordingly the cell debris was resuspended in 200 µL *dd*H_20 and 1.25 mL MeOH. To the suspension 2.5 mL $CHCl_3$ were added and the mixture was treated for 1.5 h in an ultrasonic bath. To each extract 1.25 mL of 0.9 % NaCl were added and the sample was mixed to induce phase separation. Emulsions were spun (2500 rpm, 4 °C, 10 min) and the upper hydrophilic phase was discarded. The remaining cell debris and the organic phase were filtered through a cellulose filter paper (Whatmann, Grade 595 1/2) and filter and filtrate were extracted again as described above. Organic phases combined for associated samples were dried using a Concentrator plus vacuum centrifuge (45 °C, 1 h) and residues were resuspended in 1 mL of MeOH/$CHCl_3$ (1:2). The extract was transferred to weighed HPLC glass-vials and the solvent was evaporated O/N under a gentle stream of nitrogen. Afterwards lipid content of the cells was determined gravimetrically.

Lipid content of 100 mg intact cells and cells lysed by glass beads (100 mg freeze dried cells, 1 mL H_2O, 500 µL glass beads, 6x 60 s, 6.5 m/s, freeze dried O/N) was determined from extracts of two consecutive extraction steps. Here samples were resuspended in 200 µL *dd*H_20 and 1.25 mL MeOH were added. To the suspensions 2.5 mL $CHCl_3$ were added and the mixture was treated for 1.5 h in an ultrasonic bath. The suspensions were spun (2500 rpm, 4 °C, 10 min) and supernatants were transferred to fresh glass tubes.

Remaining pellets were reextracted with 4 mL MeOH/$CHCl_3$ (1:2) as described above, spun (2500 rpm, 4 °C, 10 min) and supernatants were combined with corresponding supernatants of the previous extraction. Phase separation was induced by the addition of 2.5 mL of 0.9 % NaCl and emulsions were spun (2500 rpm, 4 °C, 10 min). Upper aqueous phases were discarded and the remaining organic phase was dried using a Concentrator plus vacuum centrifuge (45 °C, 1 h). Lipids were resuspended in 1 mL MeOH/$CHCl_3$ (1:2) and transferred to weighed HPLC glass-vials, from which the solvent was evaporated O/N under a gentle stream of nitrogen.

4.2 Proteomics of *S. cerevisiae*

4.2.1 Cell Production for Proteomics Experiments

S. cerevisiae was plated from glycerol stock either on SC or LFM-Leu agar plates, depending on strain (table 4.1) and incubated for 2 to 4 days at 30 °C under growth conditions. For this and below WT strains were treated in the same way as the corresponding LCM strains. For starter cultures grown in triplicates, cell colonies from agar plate were resuspended in 3x 5 mL of LFM or LFM-Leu medium in TC flasks and incubated under growth conditions (80 rpm, 30 °C, O/N). From each starter culture 2x 50 mL main cultures in TC flasks were inoculated (OD = 0.1) and incubated for 12 h under growth conditions (30 °C, 80 rpm). Afterwards one set of cultures was shifted to arrest conditions and all cultures were incubated for an additional 12 h (30 °C, 80 rpm). *S. cerevisiae* cultures were harvested using a Falcon centrifuge (2000 rpm, 4°C, 10 min). Cell pellets were washed with ice cold 0.9% NaCl (2000 rpm, 4 °C, 10 min) and weighted. Cell production was conducted twice in order to generate samples for the proteomics experiment and for the determination of protein content from drymass.

Table 4.1: Cultivation conditions of *S. cerevisiae* used in proteomics experiments.

			blue light condition $\lambda = 465$ nm	
strain	agar plate	medium	permissive	restrictive
ESM356	SC	LFM	–	–
Cdc48-psd^3	SC	LFM	darkness	30 $\frac{\mu mol}{m^2 \cdot s}$
SK1	SC	LFM	–	–
bPAC	SC	LFM	1 $\frac{\mu mol}{m^2 \cdot s}$	darkness
ESM356 + pRS315	LFM -Leu	LFM -Leu	–	–
Clb2$^{\Delta DB}$-psd^3	LFM -Leu	LFM -Leu	30 $\frac{\mu mol}{m^2 \cdot s}$	darknsee

4.2.2 Sample Preparation for Proteomics Experiments

After resuspending pellets in 0.9% NaCl to 150 mg/mL, protein content was quantified as described in section 4.1.2 with the Biuret assay. 1mL of each suspension was transferred to FastPrep vials and spun (2800 rpm, 4°C, 10 min). To the pellets 8 M urea, 0.1 M NH_4HCO_3 was added for a total volume of 1 mL. 500µL glass beads were added and cells were lysed using a FastPrep-24 homogenizer (6.5 m/s, 60 s, 6x, 2 min on ice after each run). The samples were spun to dissolve foam (14.000 rpm, 4°C, 45min) and cell debris was gently resuspended.

Full proteome peptide samples were prepared following an adaption of a protocol applied for routine proteome analysis by the mass spectrometry facility of Philipps-University Marburg. Accordingly lysed cells equivalent to 200 µg protein were diluted with 8 M urea in 0.1 M NH_4HCO_3 to 40 µL and pH was controlled for a value between 7 and 9. Samples were reduced with 1 µL of 0.2 M TCEP in 0.1 M NH_4HCO_3 using a thermal mixer (1000 rpm, 37 °C, 1 h) and alkylated in the dark with 1 µL of 0.4 M IAA (500 rpm, 25 °C, 30 min). The reaction was quenched with 1 µL of 0.5 M NAC in 0.1 M NH_4HCO_3 (500 rpm, 25 °C, 10 min) and samples were diluted with 10.3 µL of 0.1 M NH_4HCO_3 to 6 M urea. In preparation for proteolytic digestion sample pH was controlled and adjusted to 8 - 9 if necessary.

Alkylated protein samples were treated for 4 h at 37 °C with protease Lys-C (2.5 µL, 0.2 µg/µL in 50 mM NH_4HCO_3, $m_{protease}/m_{protein} = 1/400$), diluted with 145.2 µL of 0.1 M NH_4HCO_3 and treated O/N at 37 °C with trypsin (4 µL, 0.5 µg/µL in 50 mM NH_4HCO_3, $m_{protease}/m_{protein} = 1/100$). After adjusting the pH to < 2 with TFA, the samples were spun (13000 rpm, RT, 1 min) and the supernatant was transferred to fresh reaction cups.

Peptide samples were desalted using Chromabond C_{18} spin columns (100 µg peptide capacity) equilibrated with 150 µL ACN (2000 rpm, RT, 30 s) and 3x 150 µL 0.1% TFA in ddH_2O (2400 rpm, RT, 30 s). Columns were transferred to fresh reaction cups and 100 µL sample solution diluted with 100 µL of 0.1% TFA in ddH_2O were loaded onto the column (2000 rpm, RT, 30 s). The flow-through was reapplied (2000 rpm, RT, 30 s) and bound peptides were washed with 3x 150 µL of 5% ACN, 0.1% TFA in ddH_2O (2400 rpm, RT, 30 s). Peptides were eluted into fresh reaction cups with 2x 150 µL of 50% ACN, 0.1% TFA in ddH_2O, dried at 45 °C using a Concentrator plus vacuum centrifuge and resuspended in 30µL of 10% ACN, 0.1% TFA in ddH_2O. Resulting peptide concentrations were determined using a NanoDrop spectrometer in 1 mg/mL mode and concentrations were adjusted to 0.1 mg/mL with 10% ACN, 0.1% TFA in ddH_2O for subsequent timsTOF analysis.

4.2.3 timsTOF Data Acquisition

Mass spectrometric peptide analysis was performed using a timsTOF Pro mass spectrometer coupled with a nanoElute HPLC equipped with a 25 cm x 75 µm Aurora C_{18} RP column (1.7 µm beads). 2 µL of the desalted peptide sample ($c = 0.1$ mg/mL) were injected directly on the separation column at a constant pressure of 800 bar. Peptides were separated using a sequence of linear gradients of 0.1% FA (solvent A) in ddH_2O and 0.1% FA in ACN (solvent B) at a flow rate of 400 nL/min and 50 °C column temperature. During separation the percentage of solvent B was increased from 2% to 17% within 60 min, then increased to 25% within 30 min, afterwards increased to 37% within 10 min and finally increased to 95% within 10 min where the solvent composition was hold for additional 10 min. For mass spectrometric measurement in duplicate parameters of the preinstalled method "DDA PASEF-standard_1.1sec_cycletime" developed by Bruker Daltonics were used.

4.2.4 FASTA Database Preparation

For subsequent analysis of proteomics data FASTA files were downloaded from SGD sequence database (S288c background: orf_trans_all.20150113.fasta, SK1 background: SK1_NCSL00000000_SGD_pep.fsa). Sequence files were cleared for entries labeled as "dubious" using the *FaBox* tool. Additionally, changes to the sequence files were applied representing the genotype of strains used in the respective single strain analyses or pairwise comparisons as summarized by table 4.2.

Table 4.2: Modification of FASTA databases used for proteomics analyses.

strains	background	FASTA modifications
bPAC/SK1	SK1	ΔHis3, ΔLeu2, ΔTrp1, ΔUra3, tagRFP-bPAC, hph::NT1
Clb2$^{\Delta DB}$-psd^3/ESM356 + pDS229	S288c	ΔHis3, ΔTrp1, ΔUra3, Clb2_db-psd3
Cdc48-psd^3/ESM356	S288c	ΔHis3, ΔLeu2, ΔTrp1, ΔUra3, Cdc48-mCherry-psd3, kanMX6
yJS13	S288c	*At*CPS, *Cm*KS, *At*KO, PsKAO2, *Cm*GA20ox, *Ps*GA3ox, *At*Atr2, LexA-EDLL

4.2.5 *PEAKS Studio Xpro* Data Analysis Workflow

Analysis of datasets with *PEAKS Studio Xpro* involves a database independent *Denovo Search*, which matches MS/MS spectra to possible peptide sequences, a *PEAKS Search*, mapping *Denovo* peptides onto protein sequences of a provided FASTA database and *Label Free Quantification* (LFQ) visualizing the results. LFQ normalizes data and generates protein abundances by summing up peak areas of up to three peptides with the highest area meeting the filter criteria. Furthermore LFQ provides the feature ID-transfer, which matches MS1 spectra to peptides identified by MS/MS in other samples based on retention time and trapped ion mobility. In addition to the *UniProt* contaminant database, FASTA files used for database search were prepared as described in section 4.2.4 and validated by the software. Threshold values for peptide LFQ filters were set to match a fold change of about 8 in the respective plots for quality and average area as suggested by the manual. If applicable LFQ was normalized to TIC of a WT sample with light conditions of arrested CCM. In order to export raw data in .csv format the protein significance filter was set to ≥ 0 and the fold change filter was set to ≥ 1. Other Program parameters used for *PEAKS* analysis are summarized by the tables 4.4 to 4.3.

Table 4.3: PTMs settings.

strain	PTM		site
general	fixed	Carbamidomethylation	C
	variable	Deamidation	N, Q
	variable	Oxidation	M
	variable	Carbamylation	K
bPAC + Clb2$^{\Delta DB}$-psd[3]	variable	Phosphorylation	S, T, Y
Cdc48-psd[3]	variable	Ubiquitylation	K
yJS13	variable	Acetylation	N-term

Table 4.4: Denovo/PEAKS parameters.

parameter	value
parent mass error tolerance	10.0 ppm
fragment mass error tolerance	0.03 Da
enzyme	trypsin
max missed cleavages	3
contaminant database	yes
FDR threshold	1 %

Table 4.5: LFQ parameters (bPAC).

parameter	value
mass error tolerance	10.0 ppm
ion mobility tolerance	0.05
FDR threshold	1 %
quality	≥ 5
average area	≥ 3000
charge	1 - 10
peptide ID / group	≥ 0
in samples / group	≥ 0
significance	≥ 0
fold change	≥ 1
used peptides	≥ 2

Table 4.6: LFQ parameters (Cdc48-psd^3 and Clb2$^{\Delta DB}$-psd^3).

parameter	value
mass error tolerance	10.0 ppm
ion mobility tolerance	0.05
FDR threshold	1 %
quality	≥ 3
average area	≥ 1000
charge	1 - 10
peptide ID / group	≥ 0
in samples / group	≥ 0
significance	≥ 0
fold change	≥ 1
used peptides	≥ 2

4.2.6 Selection of Proteins from Protein Abundance Exports

From raw protein abundance exports, lists of targets with significant abundance differences between two sample groups were extracted. Therefore protein abundance was calculated from mean values of technical replicates. Afterwards protein abundances of biological replicates from two sample groups were tested with a two tailored, homoscedastic Student's t-test for p-value < 0.01 and mean abundance difference $> 10\,\%$ and the resulting list of protein targets passing this criteria was exported.

4.2.7 Protein Heatmaps

Heat maps were generated from protein abundance ratios of at least two sample groups. Here protein abundance of each sample was visualized relative to the mean protein abundance over all samples which were calculated relative to mean abundance of all samples for the scale a data dependent cutoff was chosen. Data was visualized using the *pheatmap* package in *RStudio*.

4.2.8 GO-term analysis

Gene Ontology (GO)[7] [19] allows analysis of large lists of protein targets for statistical clustering in regard to biological processes, molecular functions and cellular components. In this work list of protein targets were analyzed using the GO term finder tool provided by SGD (p-value < 0.01). Results for the ontology aspects process, function and component were exported and enrichment of each GO term was calculated from the ratio of $\frac{hits_{target}}{list_{target}}$ and $\frac{hits_{total}}{list_{total}}$ with $hits$ defined as the protein subset $list$ annotated for the corresponding GO term. GO term enrichment and relative abundance ratios (section 4.2.7) between

two sample groups were visualized using the *CellPlot* package in *RStudio* for selected GO terms.

4.3 Product Quantification

4.3.1 β-Carotene Quantification from Cell Extracts by HPLC

To *S. cerevisiae* cell pellets obtained from 20 mL culture medium by centrifugation (2400 rpm, 3 min), 200 µL glass beads and 1 mL 50 % MeOH, 50 % ACN (v/v) were added and the cells were lysed using a FastPrep-24 homogenizer (6.5 m/s, 40 s). Suspensions were spun (13000 rpm, RT, 5 min) and the yellow colored supernatants were transferred to fresh reaction cups. This process was repeated until the supernatant was colorless and extracts of the same sample were pooled. Cell extracts were analyzed using either an Agilent 1260 HPLC Infinity system equipped with degasser, autosampler, binary pump, column compartment, MWD and an EC 250/4 NUCLEOSIL 100-5 C18 column (*MACHEREY-NAGEL*) or a Thermo Dionex Ultimate 3000 HPLC equipped with degasser, autosampler, quaternary pump, column compartment, DAD and an EC 250/4 NUCLEOSIL 100-5 C18 column (*MACHEREY-NAGEL*). From each sample 25 µL were injected onto the column and separated using 50 % MeOH and 50 % ACN (v/v) as eluent (1 mL/min, 25 °C). β-Carotene was detected at $\lambda = 450$ nm and quantified using β-carotene standards solubilized in 50 % MeOH, 50 % ACN (v/v). Obtained chromatograms were processed with OpenLab CDS ChemStation Edition or Chromeleon 7.2.

4.3.2 Cordycepin Quantification from Culture Media Samples by LC-MS/MS

Cordycepin concentration was determined for culture media of the cordycepin production strains yBP03 and yJT42. Furthermore culture media for the corresponding WT strain yDS495 were analyzed as negative control. For each strain and biological replicate 6 x 50 mL LFM main cultures were prepared by inoculation with starter culture to OD = 0.1. Cultures were grown for 12 h in darkness, then half of the cultures were shifted to blue light (465 nm, 30 $\frac{\mu mol}{m^2 \cdot s}$) and each culture was grown for an additional 12 h. From each culture 1 mL was spun (2800 rpm, RT, 1 min) and 500 µL of the supernatant were transferred to fresh reaction cups. From the culture media samples 20 µL were added to 180 µL ACN + 0.0555 % formic acid and incubated for 10 min at RT. The solution was spun (14.000 rpm, 4 °C, 10 min) and 111 µL of the supernatant were added to 1 mL of 1.11 % ACN in H_2O + 0.05 % formic acid (final dilution 1:100). After incubating 10 min at RT the sample was filtered using syringe filters (RC, 0.2 µL pore size) and 200 µL were transferred to sample vials. For standards solutions cordycepin was solubilized in 10 % ACN in H_2O + 0.05 % formic acid.

Samples were analyzed using a Agilent 6470 triple quadrupol mass spectrometer coupled to a quaternary bioinert Agilent 1260 HPLC system, which was equipped with a bioinert 100 x 2.1 mm Triart C18 column (YMC, 12 nm pores, 3 µm particles). Samples were isocratically separated at 30 °C using 10 % ACN in $H_2O + 0.05$ % formic acid as eluent at a flow rate of 0.2 mL/min. After each measurement the column was reconditioned by increasing the percentage of ACN + 0.05 % formic acid to 90 % within 5 min, the eluent composition was kept constant for 2 min and afterwards the percentage of ACN was decreased to the initial eluent composition of 10 % ACN in $H_2O + 0.05$ % formic acid within 3 min. Subsequently the column was reequilibrated for another 10 min before the next analysis was started. Cordycepin was quantified in positive ion mode (capillary voltage = 3000 V, gas temperature = 300 °C, gas flow = 7 L/min, nebulizer pressure = 55 psi, sheath gas temperature = 250 °C, sheath gas flow = 11, charging voltage = 500 V). After an initial product ion screening for cordycepin precursor transitions $252 \rightarrow **$ the transitions $252 \rightarrow 119$ and $252 \rightarrow 136$ were selected as qualifier and quantifier. For this transitions the MS parameters were further optimized (cell acceleration= 5 V, fragmentor voltage= 80 V). For multiple reaction monitoring (MRM) collision energy was set to 55 V for the transition of the qualifier $252 \rightarrow 119$ and to 20 V for the quantifier transition $252 \rightarrow 136$. Obtained chromatograms were analyzed using the Agilent MassHunter Quantitative Analysis software.

For quantification by external calibration 4 µL of the sample were injected onto the column. For standard addition experiments 4 µL sample solution were drawn into the sample loop, subsequently 0.5, 1.0, 1.5, and 2.0 µL were drawn from a 280 nM cordycepin standard and the sample was supplemented with 10 % ACN in $H_2O + 0.05$ % formic acid to a total sample loop load volume of 6 µL. In between each draw step the injection needle was washed in order to avoid cross contamination. Finally the 6 µL sample were injected onto the column.

4.3.3 Quantification of GA_4 from Cell and Media Extracts

For the quantification of GA_4 corresponding *S. cerevisiae* production strains were grown for 24 h in 20 mL of WM8+ -his -trp -ura media. The cultures were spun (2.000 rpm, 5 min), the media were separated from the cell pellets and stored at 4 °C for later usage. To the cell pellets 200 µL glass beads and 1 mL MeOH were added and the cells were lysed using a FastPrep-24 homogenizer (6.5 m/s, 40 s). The suspension was spun (13.000 rpm, 5 min) and the supernatant was filtered (RC, 0.2 µL pore size) and 200 µL were transferred to sample vials (cell extract samples). The pH of the stored culture media was adjusted to 3 and ethyl acetate was added in a ratio of 1:1. Media were extracted by shaking for 10 min and mixtures were spun (13.000 rpm, 5 min). Afterwards the upper organic phases was separated. Of each ethyl acetate extract 10 mL were evaporated using a Concentrator plus vacuum centrifuge (45 °C, 8 h) and residues

were resuspended in 1 mL methanol. The samples were filtered using syringe filters (RC, 0.2 µL pore size) and 200 µL of the filtrate were transferred to sample vials (media samples, 10-fold concentrated, GA_4 detected but concentrations outside the calibration range, data not shown). 500 µL of the filtrate were dried using a Concentrator plus vacuum centrifuge (45 °C, 1.5 h) and resuspended in 50 µL MeOH (media samples, 100-fold concentrated). Standards of GA_4 were prepared in MeOH.
Samples were analyzed using the Thermo Scientific LTQ FT Ultra mass spectrometer coupled to an Agilent 1100 quaternary HPLC, which was equipped with a EC125/2 Nucleodur 100-3 C18ec column (MACHEREY-NAGEL). From each sample 5 µL were injected onto the column and analytes were separated at 25 °C using 60 % MeOH, 40 % $H_2O + 0.02$ % acetic acid (0.2 mL/min, 20 min). GA_4 was detected in ESI negative mode at -3600 V by FTMS (m/z = 200 - 500, res = 100 000). GA_4 was quantified at m/z = 331.1551 $\pm$ 3 ppm using the Xcalibur QuanBrowser software package.

4.3.4 Quantification of 3'AMP from Cell Extracts

In order to quantify 3'AMP from *S. cerevisiae* cell extracts, cultures for strains expressing *CNS3* and a corresponding WT strain were inoculated to OD = 0.1 from ONC in duplicate. The cells were grown for 6 h in darkness and afterwards for each strain one replicate was shifted to blue light conditions (465 nm, 30 $\frac{\mu mol}{m^2 \cdot s}$), while the other remained in darkness. The cultures were incubated for another 6 h and the OD was normalized (OD = 0.54 for the experiment in section **??**). From the cultures 1 mL was spun (2800 rpm, RT, 1 min) and the supernatant was discarded. The cell pellet were extracted with 1.5 mL 50% isopropanol, 50% 100mM NH_4HCO_3 in H_2O at 70 °C for 10 min as described by Castaño *et al.*[21] Extracts were filtered using syringe filters (RC, 0.2 µL pore size) and for each filtrate 1.2 mL were evaporated using a Concentrator plus vacuum centrifuge at 45 °C. The residual substance was resuspended in 400 µL of 1.25 mM dibutylammonium acetate (DBAA) and 10 mM NH_4HCO_2 in H_2O, pH 5.2. Samples were analyzed using the Thermo Scientific LTQ FT Ultra mass spectrometer coupled to an Agilent 1100 quaternary HPLC equipped with a EC 150/2 NUCLEODUR 100-3 C18 column (MACHEREY-NAGEL). From each sample 5 µL were injected on the column and analytes were separated by ion pair chromatography at 40 °C at a flow rate of 0.2 mL/min using the gradient program shown by table 4.7. Here 1.25 mM DBAA and 10 mM NH_4HCO_2 in H_2O, pH 5.2 (buffer A) and 1.25 mM DBAA and 10 mM NH_4HCO_2 in 90 % ACN, 10 % H_2O (buffer B) were used as eluents.

Analytes were detected in negative ESI mode (-3600 V) by FTMS (m/z = 250 - 400, res = 100 000) for the first 15 min of the experiment. 3'AMP was quantified at m/z = 346.0558 ± 5 ppm using the Xcalibur QuanBrowser software package.

Table 4.7: LC gradient for the analysis of 3'AMP.

t [min]	buffer [%] A	B
0	95	5
2	95	5
10	83	17
15	5	95
18	5	95
23	95	5
35	95	5

4.4 Materials

	Description	Manufacturer
Photometer	NanoDrop 2000	Thermo Scientific
	Microplate reader	Tecan Infinite 200 Pro
	Glass beads ø 0.25 - 0.5 mm	Carl Roth
Vacuum concentrator	Concentrator plus	Eppendorf
Homogenizer	FastPrep-24	MP Biomedicals
Columns	EC 250/4 NUCLEOSIL 100-5 C18 column	MACHEREY-NAGEL
	Triart C18, metal-free Narrowbore, 12 nm, S-3 µm, 100x2.1 mm	YMC
	Aurora C_{18} RP column (25 cm x 75 µm, 1.7 µm beads)	IonOpticks
	Chromabond, 20 mg C_{18} wide pore spin columns	MACHEREY-NAGEL
Mass spectrometer	LTQ-FT Ultra	Thermo Scientific
	timsTOF Pro mass spectrometer	Bruker Daltonics
	G6470A QqQ mass spectrometer	Agilent Technologies
HPLCs	1100 Series	Agilent Technologies
	1260 Series	Agilent Technologies
	1260 Series (bioinert)	Agilent Technologies
	nanoElute	Bruker Daltonics
Freeze-dryer	Alpha 2-4 LSC	Martin Christ
96-well plates	UV-STAR (UV-transparent) 96-well plates	Greiner Bio-One
Syringe Filters	SPARTAN HPLC Syringe Filter, 13 mm, Regenerated Cellulose, 0.2 µm	Whatman
Microscope	SZ60	Olympus
Bioreactor	Labfors 5 Lux (3.6 L)	Infors HT
Centrifuge	Benchtop Centrifuge 5810 R	Eppendorf

Substance	Manufacturer
β-Carotene	Tokyo Chemical Industry
yeast RNA	Merck
herring sperm DNA	Sigma-Aldrich
Lyticase Zymolyase 20 U/mg	Carl Roth
glucose	Sigma-Aldrich
BSA, globulin free	Sigma-Aldrich
GA_4	Sigma-Aldrich
cordycepin	Cayman Chemicals
protein assay dye reagent concentrate	Bio-Rad
sequencing grade modified trypsin	Serva

The chemicals used in this work for the production of media, buffers and solutions were purchased from Carl Roth GmbH + Co. KG.

Table 4.8: Low flourescent medium (LFM) composition

LFM	10 % (v/v) LFM salt stock 0.1 % (v/v) LFM trace element stock 0.1 % (v/v) LFM vitamin stock 0.2 % (w/v) amino acid mix 2 % (w/v) glucose
LFM salt stock	5 % (w/v) $(NH_4)_2SO_4$ 1 % (w/v) KH_2PO_4 0.5 % (w/v) $MgSO_4$ 0.1 % (w/v) NaCl 0.1 % (w/v) $CaCl_2$
LFM trace element stock	0.05 % (w/v) H_3BO_4 0.004 % (w/v) $CuSO_4$ 0.01 % (w/v) KI 0.02 % (w/v) $FeCl_3$ 0.04 % (w/v) $MnSO_4$
LFM vitamin stock	0.0002 % (w/v) biotin 0.04 % (w/v) calcium Pantothenate 0.2 % (w/v) inositol 0.04 % (w/v) niacin 0.02 % (w/v) para-amino benzoate 0.04 % (w/v) pyridoxin HCl 0.04 % (w/v) thiamine HCl
amino acid mix	adenine 5 g, alanine 20 g, arginine 20 g, aspartic acid 20 g, cystein 20 g, glutamine 20 g, glutamic acid 20 g, glycin 20 g, inositol 20 g, isoleucine 20 g, lysine 20 g, methionine 20 g, para-amino benzoic acid 2 g, phenylalanine 20 g, proline 20 g, serine 20 g, threonine 20 g, tyrosine 20 g, valine 20 g +/- histidine 2 g, leucine 4 g, uracil 2 g, tryptophan 2 g / 36.7 g of the mix above

Table 4.9: WM8+ medium

WM8	10 % (v/v) WM8+ salt stock 1 % (v/v) WM8+ trace element stock 1 % (v/v) WM8+ vitamin stock 0.2 % (w/v) amino acid mix 5 % (w/v) glucose 1 % (w/v) sodium glutamate
WM8+ salt stock	5 % (w/v) $(NH_4)_2SO_4$ 1 % (w/v) KH_2PO_4 0.25 % (w/v) $MgCl_2$ 6xH_2O 0.01 % (w/v) NaCl 0.01 % (w/v) $CaCl_2$ 2.8 % (w/v) NH_4Cl
WM8+ trace element stock	0.01 % (w/v) H_3BO_4 0.004 % (w/v) $CuSO_4$ 5xH_2O 0.003 % $CoCl_2$ 6xH_2O 0.001 % (w/v) KI 0.0035 % (w/v) $FeSO_4$ 7xH_2O 0.02 % (w/v) $MnCl_2$ 4xH_2O 0.005 % (w/v) Na_2MoO_4 2xH_2O 0.0625 % (w/v) $ZnSO_4$ 7xH_2O
WM8+ vitamin stock	0.0255 % (w/v) biotin 0.51 % (w/v) calcium Pantothenate 0.001 % (w/v) myo-inositol 0.11 % (w/v) niacin 0.002 % (w/v) para-amino benzoate 0.26 % (w/v) pyridoxin HCl 0.11 % (w/v) thiamine HCl
amino acid mix	adenine 5 g, alanine 20 g, arginine 20 g, aspartic acid 20 g, cystein 20 g, glutamine 20 g, glutamic acid 20 g, glycin 20 g, inositol 20 g, isoleucine 20 g, lysine 20 g, methionine 20 g, para-amino benzoic acid 2 g, phenylalanine 20 g, proline 20 g, serine 20 g, threonine 20 g, tyrosine 20 g, valine 20 g +/- histidine 2 g, leucine 4 g, uracil 2 g, tryptophan 2 g / 36.7 g of the mix above

4.4.1 Software

Description	Source
PEAKS Studio Xpro v10.6	Bioinformatics Solutions Inc.
MaxQuant v2.0.3.0	Jürgen Cox, Matthias Mann[26]
RStudio v1.4.1106	RStudio, Inc.
OpenLab CDS ChemStation Edition	Agilent Technologies
Xcalibur v3.0	Thermo Scientific
MassHunter Qualitative Analysis v10.0	Agilent Technologies
MassHunter Quantitiative Analysis v10.1	Agilent Technologies
TeXstudio v4.0.4	B. Zander, J. Sundermeyer, D. Braun, T. Hoffmann
Inkscape v1.1	open source
Mendeley Reference Manager v2.79.0	Mendeley Ltd.

R-package	Source
CellPlot	Sven E. Templer, Robert Sehlke
pheatmap	Raivo Kolde
EnhancedVolcano	Kevin Blighe

4.4.2 Databases and Tools

Description	Source
FaBox v1.61[103]	birc.au.dk/∼palle/php/fabox
SGD fasta database	sgd-archive.yeastgenome.org/sequence
SGD GO term finder	yeastgenome.org/goTermFinder
Revigo[97]	revigo.irb.hr
SGD YeastPathways[55]	pathway.yeastgenome.org
DeepL Übersetzer	www.deepl.com/translator
dict.cc	www.dict.cc

Bibliography

[1] Bio-Rad Reagent Compatibility Chart for Bio-Rad Protein Assays, Bulletin 6852, . URL https://www.bio-rad.com/sites/default/files/webroot/web/pdf/lsr/literature/Bulletin_6852.pdf.

[2] Bio-Rad Protein Assay, Bulletin LIT33, . URL https://www.bio-rad.com/sites/default/files/webroot/web/pdf/lsr/literature/LIT33.pdf.

[3] Bioinformatics Solutions, PEAKS Xpro User Manual, 2020. URL www.bioinfor.com/wp-content/uploads/2020/11/peaks106help.pdf.

[4] L. Alberghina, G. Mavelli, G. Drovandi, P. Palumbo, S. Pessina, F. Tripodi, P. Coccetti, and M. Vanoni. Cell growth and cell cycle in Saccharomyces cerevisiae: Basic regulatory design and protein–protein interaction network. *Biotechnology Advances*, 30:52–72, 1 2012. doi: 10.1016/J.BIOTECHADV.2011.07.010.

[5] M. R. Antoniewicz. A guide to metabolic flux analysis in metabolic engineering: Methods, tools and applications. *Metabolic Engineering*, 63:2–12, 1 2021. doi: 10.1016/J.YMBEN.2020.11.002.

[6] M. A. Asadollahi, J. Maury, M. Schalk, A. Clark, and J. Nielsen. Enhancement of farnesyl diphosphate pool as direct precursor of sesquiterpenes through metabolic engineering of the mevalonate pathway in Saccharomyces cerevisiae. *Biotechnology and Bioengineering*, 2010. doi: 10.1002/bit.22668.

[7] M. Ashburner, C. A. Ball, J. A. Blake, D. Botstein, H. Butler, J. M. Cherry, A. P. Davis, K. Dolinski, S. S. Dwight, J. T. Eppig, M. A. Harris, D. P. Hill, L. Issel-Tarver, A. Kasarskis, S. Lewis, J. C. Matese, J. E. Richardson, M. Ringwald, G. M. Rubin, and G. Sherlock. Gene ontology: tool for the unification of biology. The Gene Ontology Consortium. *Nature Genetics*, 25:25–29, 5 2000. doi: 10.1038/75556.

[8] M. Avalos, P. Garbeva, L. Vader, G. P. V. Wezel, J. S. Dickschat, and D. Ulanova. Biosynthesis, evolution and ecology of microbial terpenoids. *Natural Product Reports*, 39:249–272, 2 2022. doi: 10.1039/D1NP00047K.

[9] S. L. Baptista, C. E. Costa, J. T. Cunha, P. O. Soares, and L. Domingues. Metabolic engineering of Saccharomyces cerevisiae for the production of top value chemicals from biorefinery carbohydrates. *Biotechnology Advances*, 47:107697, 3 2021. doi: 10.1016/J.BIOTECHADV.2021.107697.

[10] J. Beekwilder, H. M. van Rossum, F. Koopman, F. Sonntag, M. Buchhaupt, J. Schrader, R. D. Hall, D. Bosch, J. T. Pronk, A. J. van Maris, and J.-M. Daran. Polycistronic expression of a β-carotene biosynthetic pathway in Saccharomyces cerevisiae coupled to β-ionone production. *Journal of Biotechnology*, 192:383–392, 12 2014. doi: 10.1016/j.jbiotec.2013.12.016.

[11] M. A. Berg and H. Y. Steensma. ACS2, a Saccharomyces Cerevisiae Gene Encoding Acetyl-Coenzyme A Synthetase, Essential for Growth on Glucose. *European Journal of Biochemistry*, 231:704–713, 8 1995. doi: 10.1111/j.1432-1033.1995.0704d.x.

[12] S. Bhattacharya, B. D. Esquivel, and T. C. White. Overexpression or Deletion of Ergosterol Biosynthesis Genes Alters Doubling Time, Response to Stress Agents, and Drug Susceptibility in Saccharomyces cerevisiae. *mBio*, 9, 7 2018. doi: 10.1128/MBIO.01291-18.

[13] J. Bloom and F. R. Cross. Multiple levels of cyclin specificity in cell-cycle control. *Nature Reviews Molecular Cell Biology 2007 8:2*, 8:149–160, 2 2007. doi: 10.1038/nrm2105.

[14] N. Bonander, C. Ferndahl, P. Mostad, M. D. Wilks, C. Chang, L. Showe, L. Gustafsson, C. Larsson, and R. M. Bill. Transcriptome analysis of a respiratory Saccharomycescerevisiae strain suggests the expression of its phenotype is glucose insensitive and predominantly controlled by Hap4, Cat8 and Mig1. *BMC Genomics*, 9:1–17, 7 2008. doi: 10.1186/1471-2164-9-365/FIGURES/4.

[15] C. M. Bond and Y. Tang. Engineering Saccharomyces cerevisiae for production of simvastatin. *Metabolic Engineering*, 51:1–8, 1 2019. doi: 10.1016/J.YMBEN.2018.09.005.

[16] E. S. Boyden, F. Zhang, E. Bamberg, G. Nagel, and K. Deisseroth. Millisecond-timescale, genetically targeted optical control of neural activity. *Nature Neuroscience 2005 8:9*, 8:1263–1268, 8 2005. doi: 10.1038/nn1525.

[17] K. BURTON. A study of the conditions and mechanism of the diphenylamine reaction for the colorimetric estimation of deoxyribonucleic acid. *Biochemical Journal*, 62:315–323, 2 1956. doi: 10.1042/BJ0620315.

[18] S. Busti, P. Coccetti, L. Alberghina, and M. Vanoni. Glucose Signaling-Mediated Coordination of Cell Growth and Cell Cycle in Saccharomyces Cerevisiae. *Sensors*, 10:6195–6240, 6 2010. doi: 10.3390/s100606195.

[19] S. Carbon, E. Douglass, B. M. Good, D. R. Unni, N. L. Harris, C. J. Mungall, S. Basu, R. L. Chisholm, R. J. Dodson, E. Hartline, P. Fey, P. D. Thomas, L. P. Albou, D. Ebert, M. J. Kesling, H. Mi, A. Muruganujan, X. Huang, T. Mushayahama, S. A. LaBonte, D. A. Siegele, G. Antonazzo, H. Attrill, N. H. Brown, P. Garapati, S. J. Marygold, V. Trovisco, G. dos Santos, K. Falls, C. Tabone, P. Zhou, J. L. Goodman, V. B. Strelets, J. Thurmond, P. Garmiri, R. Ishtiaq, M. Rodríguez-López, M. L. Acencio, M. Kuiper, A. Lægreid, C. Logie, R. C. Lovering, B. Kramarz, S. C. Saverimuttu, S. M. Pinheiro, H. Gunn, R. Su, K. E. Thurlow, M. Chibucos, M. Giglio, S. Nadendla, J. Munro, R. Jackson, M. J. Duesbury, N. Del-Toro, B. H. Meldal, K. Paneerselvam, L. Perfetto, P. Porras, S. Orchard, A. Shrivastava, H. Y. Chang, R. D. Finn, A. L. Mitchell, N. D. Rawlings, L. Richardson, A. Sangrador-Vegas, J. A. Blake, K. R. Christie, M. E. Dolan, H. J. Drabkin, D. P. Hill, L. Ni, D. M. Sitnikov, M. A. Harris, S. G. Oliver, K. Rutherford, V. Wood, J. Hayles, J. Bähler, E. R. Bolton, J. L. de Pons, M. R. Dwinell, G. T. Hayman, M. L. Kaldunski, A. E. Kwitek, S. J. Laulederkind, C. Plasterer, M. A. Tutaj, M. Vedi, S. J. Wang, P. D'Eustachio, L. Matthews, J. P. Balhoff, S. A. Aleksander, M. J. Alexander, J. M. Cherry, S. R. Engel, F. Gondwe, K. Karra, S. R. Miyasato, R. S. Nash, M. Simison, M. S. Skrzypek, S. Weng, E. D. Wong, M. Feuermann, P. Gaudet, A. Morgat, E. Bakker, T. Z. Berardini, L. Reiser, S. Subramaniam, E. Huala, C. N. Arighi, A. Auchincloss, K. Axelsen, G. Argoud-Puy, A. Bateman, M. C. Blatter, E. Boutet, E. Bowler, L. Breuza, A. Bridge, R. Britto, H. Bye-A-Jee, C. C. Casas, E. Coudert, P. Denny, A. Es-Treicher, M. L. Famiglietti, G. Georghiou, A. N. Gos, N. Gruaz-Gumowski, E. Hatton-Ellis, C. Hulo, A. Ignatchenko, F. Jungo, K. Laiho, P. L. Mercier, D. Lieberherr, A. Lock, Y. Lussi, A. MacDougall, M. Ma-Grane, M. J. Martin, P. Masson, D. A. Natale, N. Hyka-Nouspikel, S. Orchard, I. Pedruzzi, L. Pourcel, S. Poux, S. Pundir, C. Rivoire, E. Speretta, S. Sundaram, N. Tyagi, K. Warner, R. Zaru, C. H. Wu, A. D. Diehl, J. N. Chan, C. Grove, R. Y. Lee, H. M. Muller, D. Raciti, K. van Auken, P. W. Sternberg, M. Berriman, M. Paulini, K. Howe, S. Gao, A. Wright, L. Stein, D. G. Howe, S. Toro, M. Westerfield, P. Jaiswal, L. Cooper, and J. Elser. The Gene Ontology resource: enriching a GOld mine. *Nucleic Acids Research*, 49:D325–D334, 1 2021. doi: 10.1093/NAR/GKAA1113.

[20] R. D. Carlson and A. J. Crovetti. Commercial Uses of Gibberellins and Cytokinins and New Areas of Applied Research. *Plant Growth Substances 1988*, pages 604–610, 1990. doi: 10.1007/978-3-642-74545-4_69.

[21] S. Castaño-Cerezo, H. Kulyk-Barbier, P. Millard, J. C. Portais, S. Heux, G. Truan, and F. Bellvert. Functional analysis of isoprenoid precursors biosynthesis by quantitative metabolomics and isotopologue profiling. *Metabolomics*, 15:1–10, 9 2019. doi: 10.1007/S11306-019-1580-8.

[22] M. C. Chang, R. A. Eachus, W. Trieu, D. K. Ro, and J. D. Keasling. Engineering Escherichia coli for production of functionalized terpenoids using plant P450s. *Nature Chemical Biology 2007 3:5*, 3:274–277, 4 2007. doi: 10.1038/nchembio875.

[23] S. Cheng, X. Liu, G. Jiang, J. Wu, J. L. Zhang, D. Lei, Y. J. Yuan, J. Qiao, and G. R. Zhao. Orthogonal Engineering of Biosynthetic Pathway for Efficient Production of Limonene in Saccharomyces cerevisiae. *ACS Synthetic Biology*, 8: 968–975, 5 2019. doi: 10.1021/ACSSYNBIO.9B00135.

[24] Y. L. Cheng and R. H. Chen. The AAA-ATPase Cdc48 and cofactor Shp1 promote chromosome bi-orientation by balancing Aurora B activity. *Journal of cell science*, 123:2025–2034, 6 2010. doi: 10.1242/JCS.066043.

[25] C. Y. Chien and R. H. Chen. Cdc48 chaperone and adaptor Ubx4 distribute the proteasome in the nucleus for anaphase proteolysis. *Journal of Biological Chemistry*, 288:37180–37191, 12 2013. doi: 10.1074/jbc.M113.513598.

[26] J. Cox and M. Mann. MaxQuant enables high peptide identification rates, individualized p.p.b.-range mass accuracies and proteome-wide protein quantification. *Nature Biotechnology 2008 26:12*, 26:1367–1372, 11 2008. doi: 10.1038/nbt.1511.

[27] D. Dikicioglu, B. Kırdar, and S. G. Oliver. Biomass composition: the "elephant in the room" of metabolic modelling. *Metabolomics*, 11:1690–1701, 12 2015. doi: 10.1007/s11306-015-0819-2.

[28] A. A. Duina, M. E. Miller, and J. B. Keeney. Budding Yeast for Budding Geneticists: A Primer on the Saccharomyces cerevisiae Model System. 2014. doi: 10.1534/genetics.114.163188.

[29] P. Durairaj, E. Jung, H. H. Park, B. G. Kim, and H. Yun. Comparative functional characterization of a novel benzoate hydroxylase cytochrome P450 of Fusarium oxysporum. *Enzyme and Microbial Technology*, 70:58–65, 3 2015. doi: 10.1016/J.ENZMICTEC.2014.12.013.

[30] L. Favaro, T. Jansen, and W. H. van Zyl. Exploring industrial and natural Saccharomyces cerevisiae strains for the bio-based economy from biomass: the case of bioethanol. *Critical Reviews in Biotechnology*, 39:800–816, 8 2019. doi: 10.1080/07388551.2019.1619157.

[31] L. Feltl, V. Pacakova, K. Stulik, and K. Volka. Reliability of Carotenoid Analyses: A Review. *Current Analytical Chemistry*, 1:93–102, 3 2006. doi: 10.2174/1573411052948424.

[32] I. Fernández-Bañares, J. Clotet, J. Ariño, and J. J. Guinovart. Glycogen hyperaccumulation in Saccharomyces cerevisiae ras2 mutant A biochemical study. *FEBS Letters*, 290:38–42, 9 1991. doi: 10.1016/0014-5793(91)81220-3.

[33] T. Fujisawa and S. Masuda. Light-induced chromophore and protein responses and mechanical signal transduction of BLUF proteins. *Biophysical Reviews*, 10: 327–337, 4 2018. doi: 10.1007/S12551-017-0355-6.

[34] R. P. Galao, N. Scheller, I. Alves-Rodrigues, T. Breinig, A. Meyerhans, and J. Díez. Microbial Cell Factories Saccharomyces cerevisiae: a versatile eukaryotic system in virology. 2007. doi: 10.1186/1475-2859-6-32.

[35] G. Giaever, A. M. Chu, L. Ni, C. Connelly, L. Riles, S. Véronneau, S. Dow, A. Lucau-Danila, K. Anderson, B. André, A. P. Arkin, A. Astromoff, M. E. Bakkoury, R. Bangham, R. Benito, S. Brachat, S. Campanaro, M. Curtiss, K. Davis, A. Deutschbauer, K.-D. Entian, P. Flaherty, F. Foury, D. J. Garfinkel, M. Gerstein, D. Gotte, U. Güldener, J. H. Hegemann, S. Hempel, Z. Herman, D. F. Jaramillo, D. E. Kelly, S. L. Kelly, P. Kötter, D. LaBonte, D. C. Lamb, N. Lan, H. Liang, H. Liao, L. Liu, C. Luo, M. Lussier, R. Mao, P. Menard, S. L. Ooi, J. L. Revuelta, C. J. Roberts, M. Rose, P. Ross-Macdonald, B. Scherens, G. Schimmack, B. Shafer, D. D. Shoemaker, S. Sookhai-Mahadeo, R. K. Storms, J. N. Strathern, G. Valle, M. Voet, G. Volckaert, C. yun Wang, T. R. Ward, J. Wilhelmy, E. A. Winzeler, Y. Yang, G. Yen, E. Youngman, K. Yu, H. Bussey, J. D. Boeke, M. Snyder, P. Philippsen, R. W. Davis, and M. Johnston. Functional profiling of the Saccharomyces cerevisiae genome. *Nature*, 418:387–391, 7 2002. doi: 10.1038/nature00935.

[36] A. Goffeau, G. Barrell, H. Bussey, R. W. Davis, B. Dujon, H. Feldmann, F. Galibert, J. D. Hoheisel, C. Jacq, M. Johnston, E. J. Louis, H. W. Mewes, Y. Murakami, P. Philippsen, H. Tettelin, and S. G. Oliver. Life with 6000 Genes. *Science*, 274: 546–567, 10 1996. doi: 10.1126/SCIENCE.274.5287.546.

[37] A. K. Gombert, M. M. D. Santos, B. Christensen, and J. Nielsen. Network identification and flux quantification in the central metabolism of Saccharomyces cerevisiae under different conditions of glucose repression. *Journal of Bacteriology*, 183:1441–1451, 2001. doi: 10.1128/JB.183.4.1441-1451.2001.

[38] S. Gramazio, J. Trauth, F. Bezold, L. O. Essen, C. Taxis, and R. Spadaccini. Light-induced fermenter production of derivatives of the sweet protein monellin is maximized in prestationary Saccharomyces cerevisiae cultures. *Biotechnology Journal*, 17:2100676, 8 2022. doi: 10.1002/BIOT.202100676.

[39] J. V. Gray, G. A. Petsko, G. C. Johnston, D. Ringe, R. A. Singer, and M. Werner-Washburne. "Sleeping Beauty": Quiescence in Saccharomyces cerevisiae. *Microbiology and Molecular Biology Reviews*, 68:187–206, 6 2004. doi: 10.1128/MMBR.68.2.187-206.2004.

[40] N. Guaragnella, L. P. Coyne, X. J. Chen, and S. Giannattasio. Mitochondria–cytosol–nucleus crosstalk: learning from Saccharomyces cerevisiae. *FEMS Yeast Research*, 18:88, 12 2018. doi: 10.1093/FEMSYR/FOY088.

[41] G. Guntas, R. A. Hallett, S. P. Zimmerman, T. Williams, H. Yumerefendi, J. E. Bear, and B. Kuhlman. Engineering an improved light-induced dimer (iLID) for controlling the localization and activity of signaling proteins. *Proceedings of the National Academy of Sciences of the United States of America*, 112:112–117, 1 2015. doi: 10.1073/PNAS.1417910112.

[42] S. B. Haase and C. Wittenberg. Topology and Control of the Cell-Cycle-Regulated Transcriptional Circuitry. *Genetics*, 196:65–90, 1 2014. doi: 10.1534/GENETICS.113.152595.

[43] S. Hasenjäger, J. Trauth, S. Hepp, J. Goenrich, L. O. Essen, and C. Taxis. Optogenetic Downregulation of Protein Levels with an Ultrasensitive Switch. *ACS Synthetic Biology*, 8:1026–1036, 5 2019. doi: 10.1021/ACSSYNBIO.8B00471.

[44] P. Hedden and V. Sponsel. A Century of Gibberellin Research. *Journal of Plant Growth Regulation 2015 34:4*, 34:740–760, 10 2015. doi: 10.1007/S00344-015-9546-1.

[45] C. M. Henriksen, L. H. Christensen, J. Nielsen, and J. Villadsen. Growth energetics and metabolic fluxes in continuous cultures of Penicillium chrysogenum. *Journal of Biotechnology*, 45:149–164, 2 1996. doi: 10.1016/0168-1656(95)00164-6.

[46] S. Hepp, J. Trauth, S. Hasenjäger, F. Bezold, L. O. Essen, and C. Taxis. An Optogenetic Tool for Induced Protein Stabilization Based on the Phaeodactylum tricornutum Aureochrome 1a Light–Oxygen–Voltage Domain. *Journal of Molecular Biology*, 432:1880–1900, 3 2020. doi: 10.1016/J.JMB.2020.02.019.

[47] D. Herbert, P. J. Phipps, and R. E. Strange. Chapter III Chemical Analysis of Microbial Cells. *Methods in Microbiology*, 5:209–344, 1 1971. doi: 10.1016/S0580-9517(08)70641-X.

[48] J. Herrou and S. Crosson. Function, structure, and mechanism in bacterial photosensory LOV proteins. *Nature Reviews. Microbiology*, 9:713, 10 2011. doi: 10.1038/NRMICRO2622.

[49] S. Holbein, A. Wengi, L. Decourty, F. M. Freimoser, A. Jacquier, and B. Dichtl. Cordycepin interferes with 3' end formation in yeast independently of its potential to terminate RNA chain elongation. *RNA*, 15:837–849, 5 2009. doi: 10.1261/RNA.1458909.

[50] K. K. Hong and J. Nielsen. Metabolic engineering of Saccharomyces cerevisiae: a key cell factory platform for future biorefineries. *Cellular and Molecular Life Sciences*, 69:2671–2690, 8 2012. doi: 10.1007/S00018-012-0945-1.

[51] Z. Hu, B. He, L. Ma, Y. Sun, Y. Niu, and B. Zeng. Recent Advances in Ergosterol Biosynthesis and Regulation Mechanisms in Saccharomyces cerevisiae. *Indian Journal of Microbiology*, 57:270, 9 2017. doi: 10.1007/S12088-017-0657-1.

[52] H. Huang, T. Kawamata, T. Horie, H. Tsugawa, Y. Nakayama, Y. Ohsumi, and E. Fukusaki. Bulk RNA degradation by nitrogen starvation-induced autophagy in yeast. *The EMBO Journal*, 34:154–168, 1 2015. doi: 10.15252/EMBJ.201489083.

[53] B. E. Jackson, E. A. Hart-Wells, and S. P. T. Matsuda. Metabolic Engineering to Produce Sesquiterpenes in Yeast. *Organic Letters*, 5:1629–1632, 5 2003. doi: 10.1021/ol034231x.

[54] T. Jordá and S. Puig. Regulation of Ergosterol Biosynthesis in Saccharomyces cerevisiae. *Genes*, 11:1–18, 7 2020. doi: 10.3390/GENES11070795.

[55] P. D. Karp, R. Billington, R. Caspi, C. A. Fulcher, M. Latendresse, A. Kothari, I. M. Keseler, M. Krummenacker, P. E. Midford, Q. Ong, W. K. Ong, S. M. Paley, and P. Subhraveti. The BioCyc collection of microbial genomes and metabolic pathways. *Briefings in bioinformatics*, 20:1085–1093, 3 2019. doi: 10.1093/BIB/BBX085.

[56] M. S. Kaushik, R. Sharma, S. K. Veetil, S. K. Srivastava, and S. Kateriya. Modular Diversity of the BLUF Proteins and Their Potential for the Development of Diverse Optogenetic Tools. *Applied Sciences 2019, Vol. 9, Page 3924*, 9:3924, 9 2019. doi: 10.3390/APP9183924.

[57] F. Kawano, Y. Aono, H. Suzuki, and M. Sato. Fluorescence Imaging-Based High-Throughput Screening of Fast- and Slow-Cycling LOV Proteins. *PLOS ONE*, 8: e82693, 12 2013. doi: 10.1371/JOURNAL.PONE.0082693.

[58] K. R. Kildegaard, J. A. Arnesen, B. Adiego-Pérez, D. Rago, M. Kristensen, A. K. Klitgaard, E. H. Hansen, J. Hansen, and I. Borodina. Tailored biosynthesis of gibberellin plant hormones in yeast. *Metabolic Engineering*, 66:1–11, 7 2021. doi: 10.1016/J.YMBEN.2021.03.010.

[59] J. Kirby and J. D. Keasling. Biosynthesis of plant isoprenoids: perspectives for microbial engineering. *Annual review of plant biology*, 60:335–355, 6 2009. doi: 10.1146/ANNUREV.ARPLANT.043008.091955.

[60] K. Kolar, C. Knobloch, H. Stork, M. Žnidarič, and W. Weber. OptoBase: A Web Platform for Molecular Optogenetics. *ACS Synthetic Biology*, 7:1825–1828, 7 2018. doi: 10.1021/ACSSYNBIO.8B00120.

[61] S. Kratzer and H. Schüller. Transcriptional control of the yeast acetyl-CoA synthetase gene, ACS1 , by the positive regulators CAT8 and ADR1 and the pleiotropic repressor UME6. *Molecular Microbiology*, 26:631–641, 11 1997. doi: 10.1046/j.1365-2958.1997.5611937.x.

[62] S. Kratzer and H.-J. Schüller. Carbon source-dependent regulation of the acetyl-coenzyme A synthetase-encoding gene ACSI from saccharomyces cerevisiae. *Gene*, 161:75–79, 1 1995. doi: 10.1016/0378-1119(95)00289-I.

[63] D. C. Lamb, D. E. Kelly, N. J. Manning, M. A. Kaderbhai, and S. L. Kelly. Biodiversity of the P450 catalytic cycle: yeast cytochrome b 5/NADH cytochrome b 5 reductase complex efficiently drives the entire sterol 14-demethylation (CYP51) reaction. *FEBS Letters*, 462:283–288, 12 1999. doi: 10.1016/S0014-5793(99)01548-3.

[64] H. C. Lange and J. J. Heijnen. Statistical reconciliation of the elemental and molecular biomass composition of Saccharomyces cerevisiae. *Biotechnology and Bioengineering*, 75:334–344, 11 2001. doi: 10.1002/BIT.10054.

[65] C. E. Lawson, J. M. Martí, T. Radivojevic, S. V. R. Jonnalagadda, R. Gentz, N. J. Hillson, S. Peisert, J. Kim, B. A. Simmons, C. J. Petzold, S. W. Singer, A. Mukhopadhyay, D. Tanjore, J. G. Dunn, and H. G. Martin. Machine learning for metabolic engineering: A review. *Metabolic Engineering*, 63:34–60, 1 2021. doi: 10.1016/J.YMBEN.2020.10.005.

[66] J.-L. LEGRAS, D. MERDINOGLU, J.-M. CORNUET, and F. KARST. Bread, beer and wine: Saccharomyces cerevisiae diversity reflects human history. *Molecular Ecology*, 16:2091–2102, 5 2007. doi: 10.1111/j.1365-294X.2007.03266.x.

[67] J. Lian, S. Mishra, and H. Zhao. Recent advances in metabolic engineering of Saccharomyces cerevisiae: New tools and their applications. *Metabolic Engineering*, 50:85–108, 11 2018. doi: 10.1016/J.YMBEN.2018.04.011.

[68] R. Lindner, E. Hartmann, M. Tarnawski, A. Winkler, D. Frey, J. Reinstein, A. Meinhart, and I. Schlichting. Photoactivation Mechanism of a Bacterial Light-Regulated Adenylyl Cyclase. *Journal of Molecular Biology*, 429:1336–1351, 5 2017. doi: 10.1016/J.JMB.2017.03.020.

[69] J. Loertscher, L. L. Larson, C. K. Matson, M. L. Parrish, A. Felthauser, A. Sturm, C. Tachibana, M. Bard, and R. Wright. Endoplasmic reticulum-associated degradation is required for cold adaptation and regulation of sterol biosynthesis in the yeast Saccharomyces cerevisiae. *Eukaryotic Cell*, 5:712–722, 4 2006. doi: 10.1128/EC.5.4.712-722.2006.

[70] V. D. Longo. The Ras and Sch9 pathways regulate stress resistance and longevity. *Experimental Gerontology*, 38:807–811, 7 2003. doi: 10.1016/S0531-5565(03)00113-X.

[71] A. Losi, K. H. Gardner, and A. Möglich. Blue-Light Receptors for Optogenetics. *Chemical Reviews*, 118:10659–10709, 11 2018. doi: 10.1021/ACS.CHEMREV.8B00163/ASSET.

[72] X. Luo, M. A. Reiter, L. d'Espaux, J. Wong, C. M. Denby, A. Lechner, Y. Zhang, A. T. Grzybowski, S. Harth, W. Lin, H. Lee, C. Yu, J. Shin, K. Deng, V. T. Benites, G. Wang, E. E. Baidoo, Y. Chen, I. Dev, C. J. Petzold, and J. D. Keasling. Complete biosynthesis of cannabinoids and their unnatural analogues in yeast. *Nature 2019 567:7746*, 567:123–126, 2 2019. doi: 10.1038/s41586-019-0978-9.

[73] T. Masuko, A. Minami, N. Iwasaki, T. Majima, S. I. Nishimura, and Y. C. Lee. Carbohydrate analysis by a phenol–sulfuric acid method in microplate format. *Analytical Biochemistry*, 339:69–72, 4 2005. doi: 10.1016/J.AB.2004.12.001.

[74] A. J. Meléndez-Martínez, C. M. Stinco, and P. Mapelli-Brahm. Skin Carotenoids in Public Health and Nutricosmetics: The Emerging Roles and Applications of the UV Radiation-Absorbing Colourless Carotenoids Phytoene and Phytofluene. *Nutrients 2019, Vol. 11, Page 1093*, 11:1093, 5 2019. doi: 10.3390/NU11051093.

[75] H. Mitsuzawa, I. Uno, T. Oshima, and T. Ishikawa. Isolation and characterization of temperature-sensitive mutations in the RAS2 and CYR1 genes of Saccharomyces cerevisiae. *Genetics*, 123:739–748, 12 1989. doi: 10.1093/genetics/123.4.739.

[76] Ömur Kayikci and J. Nielsen. Glucose repression in Saccharomyces cerevisiae. *FEMS Yeast Research*, 15:68, 9 2015. doi: 10.1093/FEMSYR/FOV068.

[77] L. L. Newcomb, J. A. Diderich, M. G. Slattery, and W. Heideman. Glucose regulation of Saccharomyces cerevisiae cell cycle genes. *Eukaryotic Cell*, 2:143–149, 2 2003. doi: 10.1128/EC.2.1.143-149.2003.

[78] T. L. Nissen, U. Schulze, J. Nielsen, and J. Villadsen. Flux Distributions in Anaerobic, Glucose-Limited Continuous Cultures of Saccharomyces Cerevisiae. *Microbiology*, 143:203–218, 1 1997. doi: 10.1099/00221287-143-1-203.

[79] I. Nookaew, M. C. Jewett, A. Meechai, C. Thammarongtham, K. Laoteng, S. Cheevadhanarak, J. Nielsen, and S. Bhumiratana. The genome-scale metabolic model iIN800 of Saccharomyces cerevisiae and its validation: a scaffold to query lipid metabolism. *BMC Systems Biology*, 2:71, 12 2008. doi: 10.1186/1752-0509-2-71.

[80] C. P. O'Banion and D. S. Lawrence. Optogenetics: A Primer for Chemists. *ChemBioChem*, 19:1201–1216, 6 2018. doi: 10.1002/CBIC.201800013.

[81] A. P. Oliveira and U. Sauer. The importance of post-translational modifications in regulating Saccharomyces cerevisiae metabolism. *FEMS Yeast Research*, 12: 104–117, 3 2012. doi: 10.1111/J.1567-1364.2011.00765.X.

[82] S. B. Onofre, I. C. Bertoldo, D. Abatti, and D. Refosco. Chemical Composition of the Biomass of Saccharomyces cerevisiae - (Meyen ex E. C. Hansen, 1883) Yeast obtained from the Beer Manufacturing Process. *International Journal of Environment, Agriculture and Biotechnology*, 2:558–562, 2017. doi: 10.22161/IJEAB/2.2.2.

[83] C. J. Paddon, P. J. Westfall, D. J. Pitera, K. Benjamin, K. Fisher, D. McPhee, M. D. Leavell, A. Tai, A. Main, D. Eng, D. R. Polichuk, K. H. Teoh, D. W. Reed, T. Treynor, J. Lenihan, H. Jiang, M. Fleck, S. Bajad, G. Dang, D. Dengrove, D. Diola, G. Dorin, K. W. Ellens, S. Fickes, J. Galazzo, S. P. Gaucher, T. Geistlinger, R. Henry, M. Hepp, T. Horning, T. Iqbal, L. Kizer, B. Lieu, D. Melis, N. Moss, R. Regentin, S. Secrest, H. Tsuruta, R. Vazquez, L. F. Westblade, L. Xu, M. Yu, Y. Zhang, L. Zhao, J. Lievense, P. S. Covello, J. D. Keasling, K. K. Reiling, N. S. Renninger, and J. D. Newman. High-level semi-synthetic production of the potent antimalarial artemisinin. *Nature 2013 496:7446*, 496:528–532, 4 2013. doi: 10.1038/nature12051.

[84] S. Y. Park and J. R. Tame. Seeing the light with BLUF proteins. *Biophysical Reviews*, 9:169–176, 4 2017. doi: 10.1007/S12551-017-0258-6.

[85] A. B. Parsons, R. Geyer, T. R. Hughes, and C. Boone. Yeast genomics and proteomics in drug discovery and target validation. *Progress in Cell Cycle Research*, 5:159–166, 1 2003.

[86] G. Pereira, T. U. Tanaka, K. Nasmyth, and E. Schiebel. Modes of spindle pole body inheritance and segregation of the Bfa1p–Bub2p checkpoint protein complex. *The EMBO Journal*, 20:6359–6370, 11 2001. doi: 10.1093/EMBOJ/20.22.6359.

[87] B. Pouvreau, T. Vanhercke, and S. Singh. From plant metabolic engineering to plant synthetic biology: The evolution of the design/build/test/learn cycle. *Plant Science*, 273:3–12, 8 2018. doi: 10.1016/J.PLANTSCI.2018.03.035.

[88] W. Rademacher. Chemical regulators of gibberellin status and their application in plant production. *Annual Plant Reviews: The Gibberellins*, 49:359–404, 4 2016. doi: 10.1002/9781119210436.CH12.

[89] C. Renicke, D. Schuster, S. Usherenko, L.-O. Essen, and C. Taxis. A LOV2 Domain-Based Optogenetic Tool to Control Protein Degradation and Cellular Function. *Chemistry & Biology*, 20:619–626, 4 2013. doi: 10.1016/j.chembiol.2013.03.005.

[90] I. M. Ribeiro, W. Eßbauer, R. Kutlesa, and A. Borst. Spatial and temporal control of expression with light-gated LOV-LexA. *G3 Genes Genomes Genetics*, 12, 9 2022. doi: 10.1093/G3JOURNAL/JKAC178.

[91] I. Schaaff, J. Heinisch, and F. K. Zimmermann. Overproduction of glycolytic enzymes in yeast. *Yeast*, 5:285–290, 7 1989. doi: 10.1002/yea.320050408.

[92] J. Scheffer. Etablierung der Biosynthese von Gibberellinsäurederivaten in Saccharomyces cerevisiae und Anwendung optogenetischer Module in der Grundlagenforschung und Biotechnologie, Dissertation, 2020.

[93] C. Schuberth, H. Richly, S. Rumpf, and A. Buchberger. Shp1 and Ubx2 are adaptors of Cdc48 involved in ubiquitin-dependent protein degradation. *EMBO reports*, 5:818–824, 8 2004. doi: 10.1038/SJ.EMBOR.7400203.

[94] S. Seifert and S. Brakmann. LOV Domains in the Design of Photoresponsive Enzymes. *ACS Chemical Biology*, 13:1914–1920, 8 2018. doi: 10.1021/ACSCHEMBIO.8B00159.

[95] Y. Shiba, E. M. Paradise, J. Kirby, D. K. Ro, and J. D. Keasling. Engineering of the pyruvate dehydrogenase bypass in Saccharomyces cerevisiae for high-level production of isoprenoids. *Metabolic Engineering*, 9:160–168, 3 2007. doi: 10.1016/J.YMBEN.2006.10.005.

[96] J. S. Stephan, Y. Y. Yeh, V. Ramachandran, S. J. Deminoff, and P. K. Herman. The Tor and PKA signaling pathways independently target the Atg1/Atg13 protein kinase complex to control autophagy. *Proceedings of the National Academy of Sciences of the United States of America*, 106:17049–17054, 10 2009. doi: 10.1073/PNAS.0903316106.

[97] F. Supek, M. Bošnjak, N. Škunca, and T. Šmuc. REVIGO Summarizes and Visualizes Long Lists of Gene Ontology Terms. *PLOS ONE*, 6:e21800, 2011. doi: 10.1371/JOURNAL.PONE.0021800.

[98] H. Tamaki. Glucose-stimulated cAMP-protein kinase a pathway in yeast Saccharomyces cerevisiae. *Journal of Bioscience and Bioengineering*, 104:245–250, 10 2007. doi: 10.1263/JBB.104.245.

[99] S. D. Tetali. Terpenes and isoprenoids: a wealth of compounds for global use. *Planta*, 249:1–8, 1 2019. doi: 10.1007/S00425-018-3056-X/FIGURES/2.

[100] J. Trauth. MELICOMO - Metabolic Engineering mit lichtkontrollierten Modulen, Dissertation, 2020.

[101] E. Vergés, N. Colomina, E. Garí, C. Gallego, and M. Aldea. Cyclin Cln3 Is Retained at the ER and Released by the J Chaperone Ydj1 in Late G1 to Trigger Cell Cycle Entry. *Molecular Cell*, 26:649–662, 6 2007. doi: 10.1016/j.molcel.2007.04.023.

[102] C. E. Vickers, T. C. Williams, B. Peng, and J. Cherry. Recent advances in synthetic biology for engineering isoprenoid production in yeast. *Current Opinion in Chemical Biology*, 40:47–56, 10 2017. doi: 10.1016/J.CBPA.2017.05.017.

[103] P. Villesen. FaBox: an online toolbox for fasta sequences. *Molecular Ecology Notes*, 7:965–968, 11 2007. doi: 10.1111/J.1471-8286.2007.01821.X.

[104] J. H. Vogt and J. H. Schippers. Setting the PAS, the role of circadian PAS domain proteins during environmental adaptation in plants. *Frontiers in Plant Science*, 6: 513, 7 2015. doi: 10.3389/FPLS.2015.00513/BIBTEX.

[105] Z. Wang. Regulation of Cell Cycle Progression by Growth Factor-Induced Cell Signaling. *Cells 2021, Vol. 10, Page 3327*, 10:3327, 11 2021. doi: 10.3390/CELLS10123327.

[106] E. Welter and Z. Elazar. Autophagy mediates nonselective RNA degradation in starving yeast. *The EMBO Journal*, 34:131–133, 1 2015. doi: 10.15252/EMBJ.201490621.

[107] Y. Xia, F. Luo, Y. Shang, P. Chen, Y. Lu, and C. Wang. Fungal Cordycepin Biosynthesis Is Coupled with the Production of the Safeguard Molecule Pentostatin. *Cell Chemical Biology*, 24:1479–1489.e4, 12 2017. doi: 10.1016/j.chembiol.2017.09.001.

[108] Z. Yin, S. Wilson, N. C. Hauser, H. Tournu, J. D. Hoheisel, and A. J. Brown. Glucose triggers different global responses in yeast, depending on the strength of the signal, and transiently stabilizes ribosomal protein mRNAs. *Molecular Microbiology*, 48:713–724, 5 2003. doi: 10.1046/J.1365-2958.2003.03478.X.

[109] E. D. Yoboue, E. Augier, A. Galinier, C. Blancard, B. Pinson, L. Casteilla, M. Rigoulet, and A. Devin. cAMP-induced Mitochondrial Compartment Biogenesis. *Journal of Biological Chemistry*, 287:14569–14578, 4 2012. doi: 10.1074/jbc.M111.302786.

[110] E. T. Young, K. M. Dombek, C. Tachibana, and T. Ideker. Multiple Pathways Are Co-regulated by the Protein Kinase Snf1 and the Transcription Factors Adr1 and Cat8. *Journal of Biological Chemistry*, 278:26146–26158, 7 2003. doi: 10.1074/jbc.M301981200.

[111] H. Yuan, C. Y. M. Cheung, P. A. J. Hilbers, and N. A. W. van Riel. Flux Balance Analysis of Plant Metabolism: The Effect of Biomass Composition and Model Structure on Model Predictions. *Frontiers in Plant Science*, 7, 4 2016. doi: 10.3389/fpls.2016.00537.

[112] S. Zaman, I. Lippman, X. Zhao, and J. R. Broach. How Saccharomyces Responds to Nutrients. 2008. doi: 10.1146/annurev.genet.41.110306.130206.

[113] O. Zaragoza and J. M. Gancedo. Elements from the cAMP signaling pathway are involved in the control of expression of the yeast gluconeogenic gene FBP1. *FEBS Letters*, 506:262–266, 10 2001. doi: 10.1016/S0014-5793(01)02922-2.

[114] J. P. Zayner, C. Antoniou, and T. R. Sosnick. The Amino-Terminal Helix Modulates Light-Activated Conformational Changes in AsLOV2. *Journal of Molecular Biology*, 419:61–74, 5 2012. doi: 10.1016/J.JMB.2012.02.037.

[115] H. Zhang, P. Chen, L. Xu, D. Xu, W. Hu, Y. Cheng, and S. Yang. Construction of Cordycepin High-Production Strain and Optimization of Culture Conditions. *Current Microbiology*, 80:1–13, 1 2023. doi: 10.1007/S00284-022-03110-1.

Chapter 5

Appendix

5.0.1 Biomass Analysis

Table 5.1: Absorbance and standard deviations of BSA standards measured in triplicate.

c_{BSA} [mg/mL]	Abs.
0	0.040 ±0.001
0.51	0.085 ±0.002
1.01	0.139 ±0.001
1.51	0.191 ±0.004
2.02	0.238 ±0.007
2.52	0.296 ±0.006
3.03	0.340 ±0.012
3.53	0.397 ±0.015

Table 5.2: Absorbance, and protein content of dry mass for samples measured in triplicate.

			Abs.	protein % of dry mass
WT	batch 1	1	0.23	23.37 ±0.36
		2	0.23	23.56 ±0.31
		3	0.24	25.40 ±0.52
	batch 2	1	0.23	23.71 ±0.55
		2	0.21	21.90 ±0.88
		3	0.24	25.08 ±0.78
	batch 3	1	0.23	24.51 ±0.25
		2	0.22	22.08 ±0.57
		3	0.22	22.94 ±0.11
Clb2	batch 1	1	0.30	32.30 ±0.73
		2	0.28	30.21 ±0.47
		3	0.28	29.47 ±0.79
	batch 2	1	0.31	33.77 ±0.46
		2	0.29	30.85 ±0.53
		3	0.32	34.32 ±0.48
	batch 3	1	0.28	29.68 ±0.24
		2	0.29	31.03 ±0.22
		3	0.31	33.25 ±0.30

Table 5.3: Absorbance and standard deviations of glucose standards measured in triplicate.

c_{glu} [mM]	Abs.
0.196	0.333 ±0.010
0.403	0.591 ±0.009
0.599	0.882 ±0.001
0.794	0.991 ±0.004
1.002	1.152 ±0.007
1.198	1.510 ±0.006
1.405	1.749 ±0.012
1.601	1.996 ±0.015

Table 5.4: Absorbance and carbohydrate content of dry mass for samples measured in triplicate.

			Abs.	carbohydrate % of dry mass
WT	batch 1	1	1.03	42.88 ±3.40
		2	1.06	44.09 ±3.48
		3	1.04	43.40 ±2.36
	batch 2	1	0.97	40.29 ±3.39
		2	1.14	47.63 ±3.04
		3	1.20	50.48 ±3.92
	batch 3	1	1.05	43.51 ±0.82
		2	0.90	37.06 ±3.36
		3	1.05	43.60 ±3.39
Clb2	batch 1	1	0.77	30.76 ±2.48
		2	0.83	33.80 ±1.51
		3	0.85	34.38 ±0.83
	batch 2	1	0.87	35.31 ±5.79
		2	0.81	32.90 ±4.23
		3	0.94	38.67 ±2.73
	batch 3	1	0.86	34.84 ±2.74
		2	0.77	31.12 ±2.87
		3	0.86	35.17 ±5.02

Table 5.5: Absorbance and standard deviations of RNA standards measured in triplicate.

c_{RNA} [mg/mL]	Abs.
0	0.043 ±0.002
0.138	0.187 ±0.004
0.206	0.269 ±0.001
0.275	0.330 ±0.004
0.344	0.400 ±0.007
0.413	0.466 ±0.006
0.482	0.530 ±0.012
0.619	0.668 ±0.015

Table 5.6: Absorbance and RNA content of dry mass for samples measured in triplicate. RNA content was corrected for recovery of 85.3 %.

			Abs.	RNA % of dry mass
WT	batch 1	1	0.23	3.21 ±0.06
		2	0.22	4.03 ±0.06
		3	0.22	3.57 ±0.14
	batch 2	1	0.28	3.10 ±0.17
		2	0.27	3.95 ±0.07
		3	0.28	3.74 ±0.08
	batch 3	1	0.25	3.15 ±0.12
		2	0.26	4.06 ±0.04
		3	0.27	3.89 ±0.08
Clb2	batch 1	1	0.33	5.26 ±0.23
		2	0.33	6.35 ±0.09
		3	0.32	6.22 ±0.08
	batch 2	1	0.41	5.12 ±0.07
		2	0.38	6.08 ±0.02
		3	0.39	5.98 ±0.09
	batch 3	1	0.39	5.02 ±0.05
		2	0.37	5.97 ±0.11
		3	0.40	6.71 ±0.07

Table 5.7: Absorbance and standard deviations of DNA standards measured in triplicate.

c_{DNA} [mg/mL]	Abs.
0	0.071 ±0.001
2.028	0.088 ±0.001
3.068	0.101 ±0.001
4.019	0.112 ±0.004
6.408	0.140 ±0.007
12.742	0.212 ±0.006
19.074	0.284 ±0.012
25.111	0.354 ±0.015

Table 5.8: Absorbance and DNA content of dry mass for samples measured in triplicate.

			Abs.	DNA % of dry mass
WT	batch 1	1	0.125	0.132 ±0.007
		2	0.129	0.129 ±0.005
		3	0.125	0.119 ±0.004
	batch 2	1	0.125	0.143 ±0.006
		2	0.125	0.130 ±0.003
		3	0.127	0.132 ±0.006
	batch 3	1	0.124	0.133 ±0.002
		2	0.127	0.132 ±0.002
		3	0.130	0.134 ±0.014
Clb2	batch 1	1	0.118	0.121 ±0.002
		2	0.115	0.134 ±0.005
		3	0.116	0.092 ±0.005
	batch 2	1	0.128	0.114 ±0.001
		2	0.126	0.134 ±0.003
		3	0.126	0.097 ±0.002
	batch 3	1	0.111	0.115 ±0.005
		2	0.114	0.129 ±0.003
		3	0.111	0.091 ±0.003

Table 5.9: Lipid content of samples extracted in triplicate.

		lipids % of dry mass
WT	1	6.7
	2	6.3
	3	6.1
Clb2	1	7.2
	2	8.1
	3	7.6

Table 5.10: LC gradient for the analysis of amino-acids after oxidative and acidic protein hydrolysis.

t	buffer [%]		
[min]	A	B	C
0	100	0	0
5	100	0	0
11	95	5	0
13	80	20	0
25	70	30	0
29	30	70	0
31	20	80	0
33	10	90	0
41	0	100	0
49	0	100	0
49.1	0	0	100
52	0	0	100
52.1	100	0	0
55	100	0	0

Table 5.11: Temperature gradient of the IEC column during the analysis of amino-acids after oxidative and acidic protein hydrolysis.

t	$T_{\text{IEC column}}$
[min]	[°C]
0	49
5	49
10	56
26	56
31	74
55	74
60	50

Table 5.12: LC gradient for the analysis of amino-acids after oxidative and acidic protein hydrolysis. IEC column temperature was kept at 74 °C during the analysis.

t	buffer [%]		
[min]	A	B	C
0	30	70	0
5	30	70	0
7	10	90	0
15	0	100	0
20	0	100	0
20.1	0	0	100
23	0	0	100
23.1	30	70	0
32	30	70	0

Table 5.13: amino-acid determined from cell dry mass for samples measured in triplicate.

	WT batch 1 c [mmol/100g]	WT batch 2 c [mmol/100g]	Clb2 batch 1 c [mmol/100g]	Clb2 batch 2 c [mmol/100g]
Cys	8.10 ±0.07	6.34 ±0.09	6.98 ±0.11	6.26 ±0.10
Met	3.53 ±0.20	3.80 ±0.02	4.83 ±0.11	5.24 ±0.07
Asp/Asn	25.99 ±0.05	26.04 ±0.04	30.38 ±1.11	30.81 ±0.77
Thr	12.78 ±0.03	12.26 ±0.00	15.02 ±0.51	14.61 ±0.37
Ser	15.38 ±0.05	15.03 ±0.07	18.18 ±0.60	19.08 ±0.36
Glu/Gln	38.47 ±0.23	38.34 ±0.14	40.19 ±1.69	43.75 ±1.23
Gly	23.75 ±0.10	20.62 ±0.12	26.83 ±1.05	24.00 ±0.80
Ala	35.08 ±0.10	31.93 ±0.15	32.84 ±1.22	31.30 ±0.92
Val	14.77 ±0.05	14.56 ±0.03	18.03 ±0.53	18.02 ±0.54
Ile	10.37 ±0.07	10.16 ±0.04	12.79 ±0.45	12.39 ±0.48
Leu	14.97 ±0.09	14.76 ±0.04	18.61 ±0.68	18.73 ±0.52
Tyr	6.21 ±0.19	5.80 ±0.01	7.27 ±0.21	7.08 ±0.35
Phe	7.47 ±0.05	7.33 ±0.03	9.26 ±0.30	9.47 ±0.51
His	7.26 ±0.22	7.22 ±0.07	10.08 ±0.42	9.32 ±0.14
Lys	32.14 ±0.10	26.44 ±0.09	31.65 ±1.04	31.33 ±0.82
Arg	22.39 ±0.06	20.17 ±0.08	20.84 ±0.77	20.38 ±0.61
Pro	14.84 ±0.51	14.58 ±0.64	16.94 ±1.40	18.08 ±0.63
Trp	1.49 ±0.04	1.45 ±0.04	1.83 ±0.08	1.77 ±0.05

5.0.2 Proteomics of S. cerevisiae

Table 5.14: OD_{600} values, wet masses and corresponding standard deviations for cultures grown for the proteomics experiment. * indicates the measurement of a single culture.

	light condition	OD_{600} ONC	OD_{600} t(12h)	OD_{600} t(24h)	wet mass [mg]
Cdc48-psd^3	D (permissive)	8.5 ±0.4	2.2*	6.4 ±0.6	348 ±14
Cdc48-psd^3	L (restrictive)	8.5 ±0.4	2.2*	5.5 ±0.2	301 ±11
ESM356	D	10.7 ±0.4	3.3*	8.1 ±0.5	352 ±5
ESM356	L	10.7 ±0.4	3.3*	7.6 ±0.3	330 ±12
Clb2$^{\Delta DB}$-psd^3	D (restricitive)	6.5 ±0.5	2.1*	4.1 ±0.2	241 ±4
Clb2$^{\Delta DB}$-psd^3	L (permissive)	6.5 ±0.5	2.1*	4.1 ±0.2	230 ±5
ESM356 + pRS315	D	6.3 ±1.2	2.3*	4.7 ±0.4	285 ±7
ESM356 + pRS315	L	6.3 ±1.2	2.3*	4.7 ±0.2	279 ±3
bPAC	D (restrictive)	6.0 ±0.4	1.1 ±0.1	2.8 ±0.1	322 ±18
bPAC	L (permissive)	6.0 ±0.4	1.2 ±0.2	3.0 ±0.1	373 ±14
SK1	D	5.2 ±0.5	1.7 ±0.1	3.1 ±0.3	395 ±7
SK1	L	5.2 ±0.5	1.8 ±0.2	2.8 ±0.1	405 ±19

Table 5.15: OD_{600} values, wet masses and corresponding standard deviations for cultures grown for protein determination from dry-mass for the proteomics experiment. * indicates the measurement of a single culture.

	light condition	OD_{600} t(12h)	OD_{600} t(24h)	dry mass [mg]	protein [%]
Clb2$^{\Delta DB}$-psd^3	D (restrictive)	1.8*	4.2 ±0.2	9.2 ±0.6	21.3 ±0.4
Clb2$^{\Delta DB}$-psd^3	L (permissive)	–	4.1 ±0.1	8.6 ±1.1	20.0 ±0.8
ESM356 + pRS315	D	2.0*	4.7 ±0.2	11.3 ±0.7	19.8 ±0.4
ESM356 + pRS315	L	–	4.5 ±0.1	10.4 ±0.5	19.9 ±0.3
Cdc48-psd^3	D (permissive)	1.6*	5.1 ±0.1	11.0 ±0.2	20.1 ±0.2
Cdc48-psd^3	L (restrictive)	–	3.9 ±0.2	9.5 ±0.4	20.1 ±0.5
ESM356	D	1.8*	5.7 ±0.2	11.7 ±0.2	22.2 ±0.4
ESM356	L	–	5.4 ±0.0	11.4 ±0.1	22.5 ±0.3
bPAC	D (restrictive)	0.9*	1.9 ±0.1	7.8 ±0.4	18.3 ±0.1
bPAC	L (permissive)	–	2.0 ±0.0	7.6 ±0.5	21.0 ±0.3
SK1	D	1.1*	1.7 ±0.5	7.5 ±1.9	18.8 ±1.0
SK1	L	–	1.6 ±0.4	6.6 ±1.4	18.8 ±1.0

5.0.2.1 Volcano Plots

Table 5.16: Plotted data for proteins emphasized in volcano plot of section 2.2.2 for the Cdc48-psd^3 strain. Proteins of the mevalonate pathway upstream GGPP are highlighted in orange and proteins downstream FPP towards ergosterol are emphasized in black. Pho8, which affects the concentration of the cordycepin precursor 3'AMP is highlighted in pink in the corresponding volcano plot.

		Cdc48-psd^3 (restricted) vs WT		Cdc48-psd^3 (restricted) vs Cdc48-psd^3 (permissive)	
protein	color	$\log_2$(ratio)	-$\log_{10}$(t-test)	$\log_2$(ratio)	-$\log_{10}$(t-test)
Acs1	orange	NA	NA	NA	NA
Acs2		0.94	5.97	0.18	2.30
Erg10		0.12	1.11	0.10	1.01
Erg13		0.25	2.24	0.05	0.54
HMG1		0.43	2.25	0.18	1.12
HMG2		0.23	1.22	0.08	0.55
Erg12		0.05	0.43	0.21	1.80
Erg8		0.34	0.42	0.18	0.19
Erg19		0.13	1.43	0.15	1.10
Idi1		-0.15	1.60	-0.07	0.19
Erg20		-0.08	0.63	-0.04	0.15
Bts1		NA	NA	NA	NA
Erg9	black	0.41	5.55	0.08	1.12
Erg1		1.70	4.91	0.14	0.83
Erg7		NA	NA	NA	NA
Erg11		2.99	4.14	0.47	2.24
Erg24		-0.34	0.73	-0.14	0.13
Erg25		2.74	4.16	1.03	3.23
Erg26		-0.35	4.95	-0.02	0.15
Erg27		0.89	1.58	0.16	0.29
Erg2		0.22	1.55	-0.12	0.87
Erg3		2.48	2.61	1.17	2.06
Erg5		-0.15	0.67	-0.36	0.26
Erg4		-2.69	1.40	-1.47	0.64
Pho8	pink	-0.25	2.53	0.24	2.36

Table 5.17: Plotted data for proteins emphasized in volcano plot of section 2.2.2 for the Clb2$^{\Delta DB}$-psd^3 strain. Proteins of the mevalonate pathway upstream GGPP are highlighted in orange and proteins downstream FPP towards ergosterol are emphasized in black. Pho8, which affects the concentration of the cordycepin precursor 3'AMP is highlighted in pink in the corresponding volcano plot.

		Clb2$^{\Delta DB}$-psd^3 (restricted) vs WT		Clb2$^{\Delta DB}$-psd^3 (restricted) vs Clb2$^{\Delta DB}$-psd^3 (permissive)	
protein	color	$\log_2$(ratio)	-$\log_{10}$(t-test)	$\log_2$(ratio)	-$\log_{10}$(t-test)
Acs1	orange	NA	NA	NA	NA
Acs2		0.09	0.53	-0.07	0.68
Erg10		0.05	0.73	-0.05	0.92
Erg13		-0.05	0.55	-0.01	0.05
HMG1		0.08	0.51	-0.08	0.18
HMG2		0.01	0.02	0.02	0.06
Erg12		-0.11	1.41	-0.11	1.43
Erg8		-0.18	1.85	0.06	0.20
Erg19		-0.01	0.18	-0.08	0.60
Idi1		0.00	0.03	-0.06	0.56
Erg20		0.03	0.33	0.02	0.13
Bts1		NA	NA	NA	NA
Erg9	black	0.01	0.15	0.04	0.46
Erg1		-0.18	1.30	-0.33	2.06
Erg7		NA	NA	NA	NA
Erg11		-0.04	0.39	-0.26	1.03
Erg24		NA	NA	NA	NA
Erg25		NA	NA	NA	NA
Erg26		0.07	0.60	0.07	0.40
Erg27		0.18	0.39	0.08	0.36
Erg2		0.04	0.39	0.09	0.50
Erg3		-0.24	0.48	0.33	2.12
Erg5		-0.03	0.19	0.02	0.09
Erg4		-0.10	0.47	-0.82	0.34
Pho8	pink	-0.04	0.49	-0.15	1.46

Table 5.18: Plotted data for proteins emphasized in volcano plot of section 2.2.2 for the bPAC strain. Proteins of the mevalonate pathway upstream GGPP are highlighted in orange and proteins downstream FPP towards ergosterol are emphasized in black. Pho8, which affects the concentration of the cordycepin precursor 3'AMP is highlighted in pink in the corresponding volcano plot.

		bPAC (restricted) vs WT		bPAC (restricted) vs bPAC (permissive)	
protein	color	$\log_2$(ratio)	-$\log_{10}$(t-test)	$\log_2$(ratio)	-$\log_{10}$(t-test)
Acs1	orange	2.6	4.8	1.8	10.1
Acs2		0.28	0.52	-0.52	3.16
Erg10		-0.04	0.21	0.18	0.70
Erg13		0.25	2.78	-0.13	3.06
HMG1		NA	NA	NA	NA
HMG2		NA	NA	NA	NA
Erg12		-0.06	0.38	-0.12	1.42
Erg8		NA	NA	NA	NA
Erg19		0.13	1.16	-0.27	4.46
Idi1		-0.07	0.48	-0.18	1.85
Erg20		-0.28	4.01	-0.15	2.38
Bts1		NA	NA	NA	NA
Erg9	black	0.28	2.53	-0.02	0.31
Erg1		NA	NA	NA	NA
Erg7		NA	NA	NA	NA
Erg11		-0.02	0.18	-1.15	5.63
Erg24		0.67	0.33	0.18	0.09
Erg25		NA	NA	NA	NA
Erg26		-0.35	3.12	-0.36	2.58
Erg27		NA	NA	NA	NA
Erg2		0.23	1.75	-0.24	4.38
Erg3		NA	NA	NA	NA
Erg5		NA	NA	NA	NA
Erg4		NA	NA	NA	NA
Pho8	pink	0.13	1.52	0.38	4.46

5.0.2.2 Venn Diagrams

Table 5.19: Overlapping DAPs for the Cdc48-psd^3, Clb2$^{\Delta DB}$-psd^3 and bPAC strain in the comparison of restricted CCM and WT strain.

Cdc48-psd^3 and Clb2$^{\Delta DB}$-psd^3:
YPL111W (Car1), YMR083W (Adh3), YJL026W (Rir2), YDR025W (Rps11a), YDR177W (Ubc1), YAR007C (Rfa1), YEL037C (Rad23), YOR184W (Ser1), YDR390C (Uba2), YLR244C (Map1), YMR192W (Gyl1), YLR276C (Dbp9), YLL028W (Tpo1), YDR033W (Mrh1), YLR080W (Emp46)
Cdc48-psd^3 and bPAC:
YEL020W-A (Tim9), YBR160W (Cdk1), YCL030C (His2), YNL098C (Ras2), YFL038C (Ypt1), YHR018C (Arg4), YDR172W (Erf3), YLR061W (Rpl22a), YDR064W (Rps13), YOR361C (Prt1), YLR303W (Met17), YGR204W (Ade3), YPR191W (Qcr2), YBR115C (Lys2), YPL262W (Fum1), YDR127W (Aro1), YPL237W (Sui3), YML124C (Tub3), YBL027W (Rpl19b), YLR180W (Sam1), YKL104C (Gfa1), YLL015W (Bpt1), YKL103C (Ape1), YLR060W (Frs1), YOL058W (Arg1), YLR027C (Aat2), YJR077C (Mir1), YCR020C (Pet18), YNL064C (Mas5), YFR014C (Cmk1), YHR190W (Erg9), YMR271C (Ura10), YAL012W (Cys3), YGR144W (Thi4), YER025W (Gcd11), YGR285C (Zuo1), YGR155W (Cys4), YDL168W (Sfa1), YPL232W (Sso1), YKL065C (Yet1), YMR120C (Ade17), YBR222C (Pcs60), YBR079C (Rpg1), YBR106W (Pho88), YHR096C (Hxt5), YHR019C (Ded81), YHR027C (Rpn1), YHR064C (Ssz1), YHR068W (Dys1), YDL198C (Ggc1), YNR050C (Lys9), YDL143W (Cct4), YOR209C (Npt1), YAL044C (Gcv3), YEL071W (Dld3), YER004W (Fmp52), YER036C (Arb1), YER063W (Tho1), YER073W (Ald5), YER080W (Aim9), YER081W (Ser3), YDL007W (Rpt2), YIL109C (Sec24), YIL108W (Yik8), YIL074C (Ser33), YNL061W (Nop2), YPL214C (Thi6), YDR002W (Yrb1), YJL060W (Bna3), YJL020C (Bbc1), YJR025C (Bna1), YDR019C (Gcv1), YDR092W (Ubc13), YLR200W (Yke2), YGL106W (Mlc1), YGL001C (Erg26), YGR178C (Pbp1), YGR189C (Crh1), YGR284C (Erv29), YNL036W (Nce103), YLR216C (Cpr6), YNL274C (Gor1), YNL247W, YNL173C (Mdg1), YML126C (Erg13), YHR005C-A (Tim10), YER007C-A (Tma20), YMR178W, YML072C (Tcb3), YDR098C (Grx3), YDR190C (Rvb1), YDR399W (Hpt1), YMR196W, YMR305C (Scw10), YDR294C (Dpl1), YLR231C (Bna5), YLR179C (Ylr179c), YDR378C (Lsm6), YPR148C, YLR380W (Csr1), YOL055C (Thi20), YPL199C, YDL100C (Get3)
Clb2$^{\Delta DB}$-psd^3 and bPAC:
YGL026C (Trp5), YLR029C (Rpl15a), YOL121C (Rps19a), YLR264W (Rps28b), YML026C (Rps18b), YGL030W (Rpl30), YFL014W (Hsp12), YGL123W (Rps2), YGR159C (Nsr1), YKL035W (Ugp1), YLR441C (Rps1a), YPR163C (Tif3), YJL191W (Rps14b), YJR064W (Cct5), YLR048W (Rps0B), YNL096C (Rps7b), YML022W (Apt1), YML004C (Glo1), YOL040C (Rps15), YML073C (Rpl6a), YLR186W (Emg1), YDL223C (Hbt1), YOR007C (Sgt2), YOR222W (Odc2)
Cdc48-psd^3, Clb2$^{\Delta DB}$-psd^3 and bPAC:
YLR340W (Rpp0), YPR033C (Hts1), YHR010W (Rpl27a), YGR240C (Pfk1), YLR300W (Exg1), YNL069C (Rpl16b), YKL216W (Ura1), YEL047C (Frd1), YBL058W (Ubx1), YHR020W, YLR150W (Stm1), YJL055W, YGR180C (Rnr4), YLR192C (Hcr1)

Table 5.20: Overlapping DAPs for the Cdc48-psd^3, Clb2$^{\Delta DB}$-psd^3 and bPAC strain in the comparison of the CCM strain grown under restrictive and permissive conditions.

Cdc48-psd^3 and Clb2$^{\Delta DB}$-psd^3:
YLR056W (Erg3), YFR041C (Erj5)
Cdc48-psd^3 and bPAC:
YMR108W (Ilv2), YPL262W (Fum1), YFL018C (Lpd1), YDR481C (Pho8), YHL021C (Aim17), YBL058W (Ubx1), YHR183W (Gnd1), YNR050C (Lys9), YER004W (Fmp52), YFL041W (Fet5), YDR092W (Ubc13), YLR237W (Thi7), YDL171C (Glt1)
Clb2$^{\Delta DB}$-psd^3 and bPAC:
YJR010W (Met3), YKL150W (Mcr1), YFR030W (Met10), YIL074C (Ser33), YJR148W (Bat2), YNL220W (Ade12), YMR096W (Snz1), YPL223C (Gre1), YOR230W (Wtm1)
Cdc48-psd^3, Clb2$^{\Delta DB}$-psd^3 and bPAC:
none

Table 5.21: Protein targets used for DAP analysis of the central metabolism. Pathway proteins were obtained from SGD YeastPathways, last accessed 27th of November 2022. Corresponding identifiers were "superpathway of TCA cycle and glyoxylate cycle", "aerobic respiration, electron transport chain", "superpathway of glucose fermentation" and "pentose phosphate pathway".

TCA cycle, 27 targets:
YGL062W (Pyc1), YBR218C (Pyc2), YDL078C (Mdh3), YKL085W (Mdh1), YOL126C (Mdh2), YKL029C (Mae1), YPR001W (Cit3), YNR001C (Cit1), YCR005C (Cit2), YLR304C (Aco1), YJL200C (Aco2), YER065C (Icl1), YNL117W (Mls1), YIR031C (Dal7), YNL037C (Idh1), YOR136W (Idh2), YFL018C (Lpd1), YIL125W (Kgd1), YDR148C (Kgd2), YOR142W (Lsc1), YGR244C (Lsc2), YDR178W (Sdh4), YKL141W (Sdh3), YLL041C (Sdh2), YJL045W (Sdh9), YKL148C (Sdh1), YPL262W (Fum1)
respiratory chain, 27 targets:
YML120C (Ndi1), YHR001W-A (Qcr10), YGR183C (Qcr9), YJL166W (Qcr8), YDR529C (Qcr7), YFR033C (Qcr6), YPR191W (Qcr2), YBL045C (Cor1), YOR065W (Cyt1), YEL024W (Rip1), Q0105 (Cob), YGL191W (Cox13), YLR038C (Cox12), YDL067C (Cox9), YLR395C (Cox8), YMR256C (Cox7), YHR051W (Cox6), YNL052W (Cox5A), YGL187C (Cox4), Q0275 (Cox3), Q0250 (Cox2), Q0045 (Cox1), YDR178W (Sdh4), YKL141W (Sdh3), YLL041C (Sdh2), YJL045W (Sdh9), YKL148C (Sdh1)
glycolysis, glucose fermentation, 30 targets:
YGL253W (Hxk2), YFR053C (Hxk1), YCL040W (Glk1), YBR196C (Pgi1), YGR240C (Pfk1), YMR205C (Pfk2), YLR377C (Fbp1), YKL060C (Fba1), YDR050C (Tpi1), YJL052W (Tdh1), YJR009C (Tdh2), YGR192C (Tdh3), YCR012W (Pgk1), YKL152C (Gpm1), YHR174W (Eno2), YGR254W (Eno1), YOR347C (Pyk2), YAL038W (Cdc19), YGR087C (Pdc6), YLR134W (Pdc5), YLR044C (Pdc1), YOL086C (Adh1), YMR303C (Adh2), YMR083W (Adh3), YGL256W (Adh4), YBR145W (Adh5), YMR170C (Ald2), YOR374W (Ald4), YER073W (Ald5), YPL061W (Ald6)
pentose phosphate pathway, 10 targets:
YNL241C (Zwf1), YGR248W (Sol4), YHR163W (Sol3), YGR256W (Gnd2), YHR183W (Gnd1), YOR095C (Rki1), YJL121C (Rpe1), YPR074C (Tkl1), YBR117C (Tkl2), YLR354C (Tal1)

Table 5.22: DAPs involved in the TCA cycle for pairwise comparisons. Total numbers of targets: 27. DAP abundance was denoted relative to the growth restricted CCM condition. * Comparison visualized by heatmaps in figure 2.22 and 2.23.

comparison	high abundant DAPs	low abundant DAPs
Cdc48-psd^3 (restrictive) WT	Cit2 Mdh2 Fum1	Pyc2 Mls1
Cdc48-psd^3 (restrictive) Cdc48-psd^3 (permissive)	Cit2 Lpd1 Mdh2 Fum1	–
Clb2$^{\Delta DB}$-psd^3 (restrictive) WT	Sdh4 Pyc1 Idh2	–
Clb2$^{\Delta DB}$-psd^3 (restrictive) Clb2$^{\Delta DB}$-psd^3 (permissive)*	–	Cit2 Kgd2 Sdh4 Pyc1 Aco2 Sdh1 Sdh2 Aco1 Mls1
bPAC (restrictive) WT*	Kgd2 Icl1 Kgd1 Mdh1 Sdh1 Sdh2 Aco1 Mls1 Fum1	Lsc2
bPAC (restrictive) bPAC (permissive)*	Kgd2 Icl1 Lpd1 Lsc2 Kgd1 Mdh1 Sdh1 Sdh2 Aco1 Mls1 Cit1 Idh2 Fum1	Mdh3

Table 5.23: DAPs involved in the respiratory chain for pairwise comparisons. Total numbers of targets: 27. DAP abundance was denoted relative to the growth restricted CCM condition. * Comparison visualized by heatmaps in figure 2.22 and 2.23.

comparison	high abundant DAPs	low abundant DAPs
Cdc48-psd^3 (restrictive) WT	Qcr2	Cox2
Cdc48-psd^3 (restrictive) Cdc48-psd^3 (permissive)	–	–
Clb2$^{\Delta DB}$-psd^3 (restrictive) WT	Sdh4	–
Clb2$^{\Delta DB}$-psd^3 (restrictive) Clb2$^{\Delta DB}$-psd^3 (permissive)*	–	Sdh4 Rip1 Cox4 Sdh1 Sdh2 Qcr2
bPAC (restrictive) WT*	Cor1 Qcr7 Rip1 Cox4 Cox13 Qcr10 Sdh1 Sdh2 Cox5a Qcr2	–
bPAC (restrictive) bPAC (permissive)*	Cor1 Cox4 Cyt1 Ndi1 Qcr10 Qcr2 Qcr7 Rip1 Sdh1 Sdh2	–

Table 5.24: DAPs involved in glycolysis/glucose fermentation for pairwise comparisons. Total numbers of targets: 30. DAP abundance was denoted relative to the growth restricted CCM condition. * Comparison visualized by heatmap in figure 2.22.

comparison	high abundant DAPs	low abundant DAPs
Cdc48-psd^3 (restrictive) WT*	Adh3 Adh1 Ald6	Pgi1 Pgk1 Ald5 Hxk1 Hxk2 Pfk1 Eno1 Tdh1 Pdc5 Pfk2
Cdc48-psd^3 (restrictive) Cdc48-psd^3 (permissive)	–	Pdc6
Clb2$^{\Delta DB}$-psd^3 (restrictive) WT	Adh3	Pfk1 Gpm1
Clb2$^{\Delta DB}$-psd^3 (restrictive) Clb2$^{\Delta DB}$-psd^3 (permissive)	–	–
bPAC (restrictive) WT	Gpm1	Ald5 Pfk1
bPAC (restrictive) bPAC (permissive)	Eno1 Adh1	Hxk2 Pfk1 Pdc5 Pfk2

Table 5.25: DAPs involved in the pentose phosphate pathway for pairwise comparisons. Total numbers of targets: 10. DAP abundance was denoted relative to the growth restricted CCM condition.

comparison	high abundant DAPs	low abundant DAPs
Cdc48-psd^3 (restrictive) WT	Rpe1	Tkl2 Tal1
Cdc48-psd^3 (restrictive) Cdc48-psd^3 (permissive)	–	Tkl2 Gnd1
Clb2$^{\Delta DB}$-psd^3 (restrictive) WT	–	–
Clb2$^{\Delta DB}$-psd^3 (restrictive) Clb2$^{\Delta DB}$-psd^3 (permissive)	–	–
bPAC (restrictive) WT	Tkl2 Sol4 Gnd2	Sol3 Gnd1 Zwf1
bPAC (restrictive) bPAC (permissive)	Tkl2 Sol4 Gnd2	Sol3 Gnd1 Tkl1

Table 5.26: Relative abundance of DAPs for corresponding genes regulated by the transcription factors (TFs) Cat8 and Adr1. Regulated genes were obtained from SGD, last accessed 27th of November 2022. ND means that the protein was not available in the dataset of the proteomics experiment. Abundance is denoted relative to the bPAC strain grown under restrictive conditions.

TF	protein	bPAC (restrictive) vs WT	bPAC (restrictive) vs bPAC (permissive)
Cat8	Aro10	ND	ND
	Aro9	ND	ND
	Fbp1	ND	ND
	Icl1	high	high
	Pck1	high	not a DAP
	Aim17	not a DAP	high
	Fre1	ND	ND
	Hsp104	not a DAP	not a DAP
	Hsp30	ND	ND
	Met17	ND	ND
	Pho89	high	low
	Tsl1	high	high
	YKL177W	ND	ND
Adr1	Usv1	ND	ND
	Atg32	ND	ND
	Atp7	high	high
	Cmk2	not a DAP	high
	Cyk3	ND	ND
	Fun26	ND	ND
	Glc7	not a DAP	not a DAP
	Gld1	ND	ND
	Hem25	ND	ND
	Hir3	ND	ND
	Ipa1	ND	ND

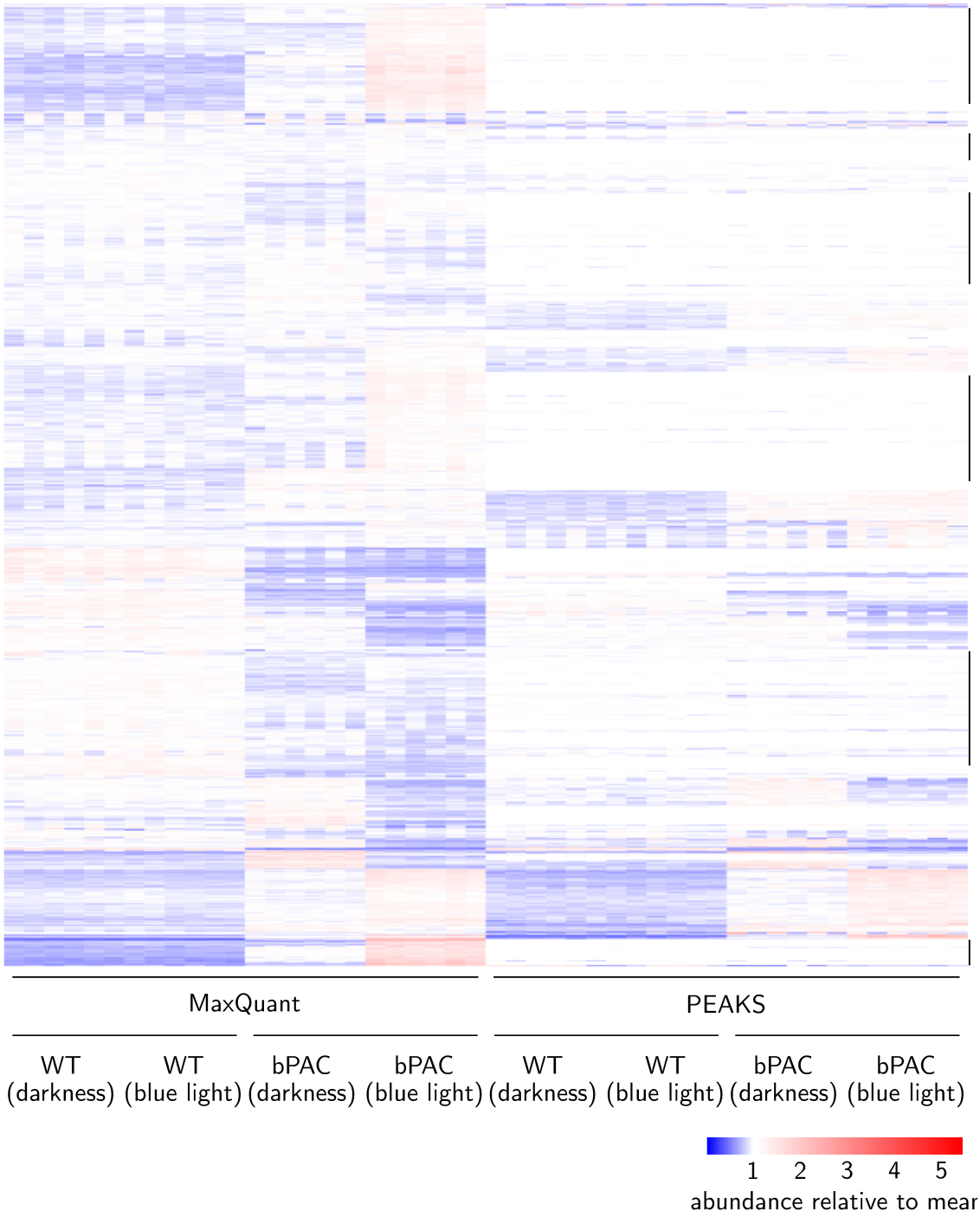

Figure 5.1: Comparison of relative protein abundances obtained after *MaxQuant* and *PEAKS* analysis. The determined protein abundance was normalized to the average protein abundance for samples analyzed by each software package before comparison, because the obtained raw values were not comparable. Large white areas for *PEAKS* analysis marked right of the heat map stand for unavailable data, likely due to more stringent filtering criteria for *PEAKS* analysis. For a detailed discussion of the comparison see the research report of Mohamed Watad.

5.0.3 Product Quantification

5.0.3.1 LC-MS Quantification of GA_4

Table 5.27: Results for GA_4 quantification of GA_4 production strains no. 1 - 6 from 100-fold concentrated media extracts. Data visualized in table 2.10 was converted to ng/L. Strains labeled with * were used as negative controls and carried the plasmids pRS313, pRS314 and pRS316. ($M_{GA4} = 332.4\,g/mol$).

	area (counts · s)			c_{GA4} [nM]	c_{GA4} [nM]
sample	rep. 1	rep. 2	rep. 3	(sample)	(culture)
6.3 nM GA_4	26903	29669	28726	NC	NC
12.6 nM GA_4	39265	38890	41166	NC	NC
31.5 nM GA_4	70190	60518	66349	NC	NC
63.0 nM GA_4	115032	110971	116291	NC	NC
315.2 nM GA_4	593979	628721	641050	NC	NC
yGA01	158089	98167	65764	83 ± 9	0.83 ± 0.09
yGA02	76942	122657	129309	82 ± 18	0.82 ± 0.18
yGA03	182813	172148	147880	51 ± 24	0.51 ± 0.24
yGA04	200450	165572	131613	53 ± 15	0.53 ± 0.15
yJS13*	2713	7267	2430	ND	NC
yJT23*	5251	2366	3263	ND	NC

5.0.3.2 LC-MS Quantification of 3'AMP

Table 5.28: Results of 3'AMP quantification for strains yDS495 + pDS264, yDS495 + pBP02, yDS495 + pBP03, yDS495 + pBP04 and the corresponding WT (yDS495) strain grown in darkness (D) and under blue light (L, 465 nm, 30 $\frac{\mu mol}{m^2 \cdot s}$) condition. Data visualized in figure 2.29 was converted to mg/L ($M_{3'AMP} = 347.2\,g/mol$).

sample	light cond.	area (counts · s) rep. 1	rep. 2	rep. 3	$c_{3'AMP}$ [µM] (sample)	$c_{3'AMP}$ [µM] (culture)
5 µM 3'AMP	–	65158	67317	64954	NC	NC
10 µM 3'AMP	–	146627	134402	124100	NC	NC
30 µM 3'AMP	–	426944	438367	437557	NC	NC
60 µM 3'AMP	–	804870	829058	815913	NC	NC
100 µM 3'AMP	–	1393944	1493058	1232732	NC	NC
yDS495 + pDS263	D	344314	386597	336792	25.7 ± 2.0	12.9 ± 1.0
	L	444001	333387	347139	27.1 ± 4.4	13.6 ± 2.2
yDS495 + pBP02	D	343430	351843	402034	26.5 ± 2.3	13.2 ± 1.2
	L	358311	390230	383800	27.3 ± 1.2	13.7 ± 0.6
yDS495 + pBP03	D	280759	244648	226621	18.1 ± 2.0	9.0 ± 1.0
	L	156726	202157	150276	12.1 ± 2.1	6.1 ± 1.0
yDS495 + pBP04	D	176730	121749	146218	10.6 ± 2.0	5.3 ± 1.0
	L	136893	140136	95917	8.8 ± 1.8	4.4 ± 0.9
yDS495 (WT)	D	37287	43480	42875	2.8 ± 0.2	1.4 ± 0.1
	L	61943	60462	59686	4.2 ± 0.1	2.1 ± 0.0
yDS495 + pBP02 + 3'AMP/5'AMP	D	781586	845296	942332	62.3 ± 5.9	31.1 ± 3.0

5.0.3.3 LC-MS/MS Quantification of Cordycepin

Table 5.29: Description of cordycepin production strains and the WT strain mentioned within this work.

strain	arrest mechanism	reference
yBP03	–	Bastian Pook
yJT42	blue light induced degradation of Cyr1-psd^{AS}	Dr. Jonathan Trauth
yJS6	blue light induced degradation of Cdc48-psd^{3}	Dr. Johannes Scheffer
yBP03 + pMB3	blue light induced accumulation of Clb2$^{\Delta DB}$	Dr. Johannes Scheffer
yBP03 + pMB4	blue light induced accumulation of $^{\Delta N}$Sic1	Dr. Johannes Scheffer
yDS495 (WT)	–	Dr. Christof Taxis

Table 5.30: Results of cordycepin quantification by external calibration for strain yBP03, two biological replicates of yJT42 and the corresponding WT strain grown in darkness (D) and under blue light (L, 465 nm, 30 $\frac{\mu mol}{m^2 \cdot s}$) condition. For each strain, condition and biological replicate three main cultures were grown and measured in triplicate. From the standard deviation of the linear regression σ the LOD was calculated to 5.7 nM (3σ) and the LOQ to 19.1 nM (10σ). Culture medium samples were measured diluted in the ratio 1:100. Data visualized in figure 2.32 was converted to mg/L ($M_{cordycepin} = 251.24$ g/mol).

sample	light cond.	area (counts · s) rep. 1	rep. 2	rep. 3	$c_{cordycepin}$ [nM] (sample)	$c_{cordycepin}$ [µM] (culture)
12.5 nM cordycepin	–	3489	3454	3448	NC	NC
25 nM cordycepin	–	7045	7056	7062	NC	NC
50 nM cordycepin	–	14343	14249	14119	NC	NC
75 nM cordycepin	–	22366	22408	22423	NC	NC
100 nM cordycepin	–	29068	29108	29003	NC	NC
150 nM cordycepin	–	43694	43589	43414	NC	NC
200 nM cordycepin	–	56744	56384	56440	NC	NC
yBP03	D	6603	6678	6667	21.7 ± 0.1	2.17 ± 0.01
		6681	6832	6785	22.1 ± 0.3	2.21 ± 0.03
		6720	6610	6706	21.8 ± 0.2	2.18 ± 0.02
					mean	2.19 ± 0.02
	L	12498	12336	12378	41.8 ± 0.3	4.18 ± 0.03
		12018	11661	11844	39.8 ± 0.6	3.98 ± 0.06
		12660	12681	12541	42.6 ± 0.3	4.26 ± 0.03
					mean	4.14 ± 0.14
yJT42-1	D	11142	11319	11411	42.6 ± 0.3	4.26 ± 0.03
		11206	11240	11112	37.5 ± 0.2	3.75 ± 0.02
		11514	11567	11553	38.8 ± 0.1	3.88 ± 0.01
					mean	3.96 ± 0.26
	L	21308	21020	20789	72.0 ± 0.9	7.20 ± 0.09
		23515	23402	23342	80.3 ± 0.3	8.03 ± 0.03
		20914	20703	21061	71.5 ± 0.6	7.15 ± 0.06
					mean	7.46 ± 0.50
yJT42-2	D	12978	13066	13207	44.2 ± 0.4	4.42 ± 0.04
		13254	13274	13074	44.6 ± 0.4	4.46 ± 0.04
		13962	14049	13973	47.4 ± 0.2	4.74 ± 0.02
					mean	4.54 ± 0.17
	L	40325	40229	40304	139.3 ± 0.2	13.93 ± 0.02
		41273	40835	40952	141.8 ± 0.8	14.18 ± 0.08
		41435	41419	41447	143.3 ± 0.0	14.33 ± 0.00
					mean	14.15 ± 0.20
WT	D	261	324	267	ND	NC
		277	254	263	ND	NC
		278	285	273	ND	NC
					mean	NC
	L	295	274	291	ND	NC
		281	274	277	ND	NC
		299	290	274	ND	NC
					mean	NC

Table 5.31: Results of cordycepin quantification by standard addition for strain yBP03 grown in darkness (D) and under blue light (L, 465 nm, 30 $\frac{\mu mol}{m^2 \cdot s}$) condition. For each condition three main cultures were grown and and samples were measured in duplicate. From the standard deviation of the linear regression σ the LOD (3σ) the LOQ (10σ) were calculated. Data visualized in figure 2.34 was converted to mg/L ($M_{cordycepin} = 251.24\,g/mol$).

sample	light cond.	cordycepin spike	area (counts · s) rep. 1	area (counts · s) rep. 2	$c_{cordycepin}$ [nM] (sample 1:100 dilution)	$c_{cordycepin}$ [µM] (culture)
yBP03	D	0 nM	56962	58317		
		35 nM	153968	157659		
		70 nM	265897	267365		
		105 nM	367230	368365		
		140 nM	455207	461491	20.2	2.02
					LOD = 5.7, LOQ = 18.9	
		0 nM	57120	56150		
		35 nM	154674	161015		
		70 nM	260902	265615		
		105 nM	369449	359027		
		140 nM	469456	463401	19.3	1.93
					LOD = 3.8, LOQ = 12.8	
		0 nM	57767	56174		
		35 nM	150969	150482		
		70 nM	253549	250245		
		105 nM	349001	349539		
		140 nM	445773	444657	20.0	2.00
					LOD = 2.0, LOQ = 6.8	
					mean	1.98 ± 0.07
yBP03	L	0 nM	83106	83930		
		35 nM	174160	174798		
		70 nM	261708	262226		
		105 nM	345966	350276		
		140 nM	434596	434133	34.2	3.42
					LOD = 2.3, LOQ = 7.6	
		0 nM	86144	84901		
		35 nM	172612	172856		
		70 nM	259669	257276		
		105 nM	341541	341400		
		140 nM	421615	422506	36.5	3.65
					LOD = 2.8, LOQ = 9.4	
		0 nM	94528	91577		
		35 nM	178738	178687		
		70 nM	267047	266971		
		105 nM	347722	349553		
		140 nM	430363	432296	39.1	3.91
					LOD = 2.8, LOQ = 9.2	
					mean	3.66 ± 0.16

Table 5.32: Results of cordycepin quantification by standard addition for strain yJT42-1 grown in darkness (D) and under blue light (L, 465 nm, 30 $\frac{\mu mol}{m^2 \cdot s}$) condition. For each condition three main cultures were grown and and samples were measured in duplicate. From the standard deviation of the linear regression σ the LOD (3σ) the LOQ (10σ) were calculated. Data visualized in figure 2.34 was converted to mg/L ($M_{cordycepin} = 251.24\,g/mol$).

sample	light cond.	cordycepin spike	area (counts · s) rep. 1	area (counts · s) rep. 2	$c_{cordycepin}$ [nM] (sample 1:100 dilution)	$c_{cordycepin}$ [µM] (culture)
yJT42-1	D	0 nM	84960	89868		
		35 nM	183092	183634		
		70 nM	283061	285575		
		105 nM	380852	379818		
		140 nM	471149	469695	32.2	3.22
					LOD = 3.5, LOQ = 11.7	
		0 nM	89418	87360		
		35 nM	179550	180510		
		70 nM	280587	279131		
		105 nM	371699	369988		
		140 nM	458097	459613	33.5	3.35
					LOD = 3.6, LOQ = 12.1	
		0 nM	89550	89930		
		35 nM	181379	180572		
		70 nM	276640	275466		
		105 nM	365731	363030		
		140 nM	446226	444327	36.2	3.62
					LOD = 5.0, LOQ = 16.5	
					mean	3.40 ± 0.09
yJT42-1	L	0 nM	158929	159524		
		35 nM	242983	237966		
		70 nM	329447	327477		
		105 nM	404738	403310		
		140 nM	476181	474130	71.5	7.15
					LOD = 6.9, LOQ = 22.9	
		0 nM	158733	158540		
		35 nM	236888	236589		
		70 nM	316636	316133		
		105 nM	388988	389460		
		140 nM	460142	456902	75.1	7.51
					LOD = 4.9, LOQ = 16.4	
		0 nM	156699	155118		
		35 nM	230955	230074		
		70 nM	308298	309056		
		105 nM	378946	378603		
		140 nM	449538	445681	75.6	7.56
					LOD = 4.5, LOQ = 15.0	
					mean	7.40 ± 0.26

Table 5.33: Results of cordycepin quantification by standard addition for strain yJT42-2 grown in darkness (D) and under blue light (L, 465 nm, 30 $\frac{\mu mol}{m^2 \cdot s}$) condition. For each condition three main cultures were grown and and samples were measured in duplicate. From the standard deviation of the linear regression σ the LOD (3σ) the LOQ (10σ) were calculated. Data visualized in figure 2.34 was converted to mg/L ($M_{cordycepin} = 251.24\,g/mol$).

sample	light cond.	cordycepin spike	area (counts · s) rep. 1	area (counts · s) rep. 2	$c_{cordycepin}$ [nM] (sample 1:100 dilution)	$c_{cordycepin}$ [µM] (culture)
yJT42-2	D	0 nM	90739	95527		
		35 nM	180418	180304		
		70 nM	263918	263815		
		105 nM	342611	343985		
		140 nM	414038	422034	41.9	4.19
					LOD = 5.9, LOQ = 19.6	
		0 nM	94241	94998		
		35 nM	177220	179984		
		70 nM	265439	266178		
		105 nM	343020	336106		
					LOD = 5.0, LOQ = 16.5	
		140 nM	421029	422907	41.6	4.16
		0 nM	95789	101979		
		35 nM	185152	183552		
		70 nM	267548	267999		
		105 nM	351584	350666		
		140 nM	430643	427034	42.7	4.27
					LOD = 3.7, LOQ = 12.2	
					mean	4.21 ± 0.02
yJT42-2	L	0 nM	304994	301652		
		35 nM	377320	378483		
		70 nM	454702	455019		
		105 nM	528345	527866		
		140 nM	601544	598337	143.2	14.32
					LOD = 2.7, LOQ = 8.9	
		0 nM	297311	296041		
		35 nM	368897	369892		
		70 nM	445995	435029		
		105 nM	512027	514718		
		140 nM	584652	583108	144.7	14.47
					LOD = 4.3, LOQ = 14.3	
		0 nM	301543	299754		
		35 nM	373257	373167		
		70 nM	447982	447275		
		105 nM	518867	518743		
		140 nM	585915	582762	148.4	14.84
					LOD = 4.1, LOQ = 13.6	
					mean	14.54 ± 0.11

Table 5.34: Results of cordycepin quantification by standard addition for the WT strain yDS495 grown in darkness (D) and under blue light (L, 465 nm, 30 $\frac{\mu mol}{m^2 \cdot s}$) condition. For each condition three main cultures were grown and and samples were measured in duplicate. From the standard deviation of the linear regression σ the LOD (3σ) the LOQ (10σ) were calculated. Data visualized in figure 2.34 was converted to mg/L ($M_{cordycepin} = 251.24\,g/mol$).

sample	light cond.	cordycepin spike	area (counts · s) rep. 1	area (counts · s) rep. 2	$c_{cordycepin}$ [nM] (sample 1:100 dilution)	$c_{cordycepin}$ [µM] (culture)
WT	D	0 nM	1642	6013		
		35 nM	81774	81421		
		70 nM	161978	163232		
		105 nM	240365	238439		
		140 nM	310718	313631	2.3	NC
					LOD = 3.6, LOQ = 12.1	
		0 nM	1743	1660		
		35 nM	84491	84923		
		70 nM	169692	170192		
		105 nM	249925	251538		
		140 nM	325636	324882	1.7	NC
					LOD = 4.1, LOQ = 13.8	
		0 nM	1689	1675		
		35 nM	82627	77149		
		70 nM	161560	161360		
		105 nM	235524	235977		
		140 nM	309339	307481	1.6	NC
					LOD = 4.2, LOQ = 14.2	
					mean	NC
WT	L	0 nM	1760	2356		
		35 nM	77131	76197		
		70 nM	150651	150804		
		105 nM	222305	221066		
		140 nM	288726	289322	2.1	NC
					LOD = 3.6, LOQ = 11.9	
		0 nM	1836	1908		
		35 nM	81429	81501		
		70 nM	163210	163648		
		105 nM	238897	237859		
		140 nM	312157	311719	1.8	NC
					LOD = 3.8, LOQ = 12.5	
		0 nM	1713	1729		
		35 nM	71429	71034		
		70 nM	144022	144112		
		105 nM	211355	209404		
		140 nM	275864	276370	1.6	NC
					LOD = 3.4, LOQ = 11.5	
					mean	NC

5.0.4 Plasmids and Strains

Table 5.35: Description of mentioned plasmids.

plasmid	description	reference
pUDE269	P_{TDH3}-*crtYB-T2A1-crtI-T2A2-crtE-tTEF URA3*	Beekwilder *et al.* 2014[10]
pDS263	pRS316 *URA3 CEN/ARS ori bla* P_{LexA}-*YFP-CNS3-*T_{DIT1}	Dr. Christof Taxis
pBP02	P_{LexA}, myCitrine-Truncated Cns3 (AA 1-107), Tdit1, Obtained with Primer BP07_rev/yfp-cns3_up from pDS263	Bastian Pook
pBP03	P_{LexA}, myCitrine-Truncated Cns3 (AA 1-119), Tdit1, Obtained with Primer BP08_rev/yfp-cns3_up from pDS263	Bastian Pook
pBP04	P_{LexA}, myCitrine-Truncated Cns3 (AA 1-153), Tdit1, Obtained with Primer BP09_rev/yfp-cns3_up from pDS263	Bastian Pook
pMB1	P_{ADH1}-*GAI-VN HIS3*	Dr. Jonathan Trauth
pMB2	P_{ADH1}-*AtGid1A-VC TRP1*	Dr. Jonathan Trauth
pMB3	P_{ADH1}-*LexA-BD-Cry2* P_{LexA}-*Clb-DB-3myc LEU2* Amp^R	Marco Bentele 2018
pMB4	P_{ADH1}-*LexA-BD-Cry2* P_{LexA}-*deltaN_sic1-3myc LEU2* Amp^R	Marco Bentele 2018
pRS313	*CEN6 ARSH4 HIS3*	Dr. Christof Taxis
pRS314	*CEN6 ARSH4 TRP1*	Dr. Christof Taxis
pRS315	*CEN6 ARSH4 LEU2*	Dr. Christof Taxis
pRS316	*CEN6 ARSH4 URA3*	Dr. Christof Taxis
pJS26	P_{LexA}-*YFP-OsKS-TDIT1 ARS/CEN URA3*	Dr. Christof Taxis
pJS27	P_{LexA}-*YFP-AtKS-TDIT1 ARS/CEN URA3*	Dr. Christof Taxis
pDS312	P_{CYC1}-*tagRFP-bPAC LEU2*	Dr. Christof Taxis
pDS229	pRS315 P_{CLB2}-*clb2ΔDB-3myc-psd3*	Dr. Christof Taxis
pDS261	P_{LexA}-*YFP-CNS1-Tdit1 URA3 CEN6 ARSH4*	Dr. Christof Taxis

Table 5.36: Description of mentioned *S. cerevisiae* strains.

strain	description	reference
Cdc48-psd^3 (ySH2)	ESM356-1 *cdc48-mCherry-psd3::kanMX1*	Sophia Hasenjäger[43]
Clb2$^{\Delta DB}$-psd^3	ESM356-1, pDS229	Sophia Hasenjäger[43]
bPAC (ySEB38)	yCR75 *cyr1Δ::hphNT1*, pDS312	Dr. Sebastian Hepp[46]
ESM356-1	S288c MATa *ura3-53 leu2Δ1 his3Δ200 trp1Δ63*	Pereira *et. al.* 2001[86]
SK1 (YCR75)	MATa *ho::LYS2 his3 leu2 trp1ΔFA ura3*	Dr. Christof Taxis
yDS591	yDS493 *CDC48-psd3::kanMX6 PTDH3-CrtYB-T2A1-CrtI-T2A2-CrtE-TTEF::can1*	Dr. Christof Taxis
yBP03	*HIS3::hphNT1:::*P_{ADH1}*-VP16-CIB1::HIS3 URA3::natNT2::*P_{ADH1}*-LexA-BDCry2::URA3 LEU2::*P_{LexA}*-myCitrine-Cns2::LEU2*, pDS261	Bastian Pook
yJT42	ESM356 *cyr1-myc-AsLOV-cODC1::kanMX6 HIS3::hphNT1::*P_{ADH1}*-VP16-CIB1::HIS3 URA3::natNT2::*P_{ADH1}*-LexA-BDCry2::URA3 LEU2::*P_{LexA}*-myCitrineCns2::LEU2, pDS261*	Dr. Jonathan Trauth
yJS6	yBP03 cdc48-mCherry-iLIDΔA-cODC1::kanMX6	Dr. Johannes Scheffer
yDS495	ESM357-3 Matα *leu2Δ1 trp1Δ63 HIS3::hphNT1:::*P_{ADH1}*-VP16-CIB1::HIS3 URA3::natNT2::*P_{ADH1}*-LexA-BDCry2::URA3*	Dr. Christof Taxis
yDS493	ESM356-1 MATa *ura3-53 LEU2 trp1Δ63 his3Δ200*	Dr. Christof Taxis
ySH1	yDS28 *cdc48-mCherry-iLIDΔA-cODC1::kanMX6*	Sophia Hasenjäger
yJS13	ESM357 x Sk1 Matα *can1::Tdit1-PsKAO-YFP*–P_{LexA}*::*P_{LexA}*-YFP-AtKO-Tdit1 ura3::Tdit1-CmKS-YFP-*P_{LexA}*::*P_{LexA}*-YFP-AtCPS-Tdit1 leu2::Tdit-AtATR2-YFP-*P_{LexA}*-*P_{ADH1}*-LexA-EDLL 911b::Tdit1-PsGA3ox-YFP-*P_{LexA}*-::*P_{LexA}*-YFP-CmGA20ox-Tdit1*	Dr. Christof Taxis
yGA01	yJS13-2, pMB1-2 pMB2-2 pJS26-3	Dr. Christof Taxis
yGA02	yJS13-2, pMB1-2 pMB2-2 pJS27-3	Dr. Christof Taxis
yGA03	yJS13-4, pMB1-2 pMB2-2 pJS27-3	Dr. Christof Taxis
yGA04	yJS13-2, pMB1-2 pMB2-2 pJS27-3	Dr. Christof Taxis
yJT23	S288C MATα *ura3-53 leu2Δ1 his3Δ200 trp1Δ63*	Dr. Christof Taxis
yDS28	ESM356-1 MATa P_{HIS3}*-mCherry-TUB1::TRP1*	Dr. Christof Taxis
ESM357	MATα *ura3-53 leu2Δ1 trp1Δ63*	Pereira *et. al.* 2001[86]

5.0.5 Protein Sequences

> LexA-EDLL
MKALTARQQEVFDLIRDHISQTGMPPTRAEIAQRLGFRSPNAAEEHLKALARKGVIEI
VSGASRGIRLLQEEEEGLPLVGRVAAGEPLLAQQHIEGHYQVDPSLFKPNADFLLRVS
GMSMKDIGIMDGDLLAVHKTQDVRNGQVVVARIDDEVTVKRLKKQGNKVELLPEN
SVFKPIVVDLRQQSFTIEGLAVGVIRNGDWLEFPGIREVFEFEYLDDKVLEELDSEERK
R

> *Cm*GA20ox
GSMHVVTSTPEARHDGAPLVFDASVLRHQHNIPKQFIWPDEEKPAATCPELEVPLID
LSGFLSGEKDAAAEAVRLVGEACEKHGFFLVVNHGVDRKLIGEAHKYMDEFFELPLS
QKQSAQRKAGEHCGYASSFTGRFSSKLPWKETLSFRFAADESLNNLVLHYLNDKLG
DQFAKFGRVYQDYCEAMSGLSLGIMELLGKSLGVEEQCFKNFFKDNDSIMRLNFYPP
CQKPHLTLGTGPHCDPTSLTILHQDQVGGLQVFVDNQWRLITPNFDAFVVNIGDTF
MALSNGRYKSCLHRAVVNSERTRKSLAFFLCPRNDKVVRPPRELVDTQNPRRYPDF
TWSMLLRFTQTHYRADMKTLEAFSAWLQQEQQEQQEQQFNI

> *At*KO
GSMAFFSMISILLGFVISSFIFIFFFKKLLSFSRKNMSEVSTLPSVPVVPGFPVIGNLLQL
KEKKPHKTFTRWSEIYGPIYSIKMGSSSLIVLNSTETAKEAMVTRFSSISTRKLSNALT
VLTCDKSMVATSDYDDFHKLVKRCLLNGLLGANAQKRKRHYRDALIENVSSKLHAH
ARDHPQEPVNFRAIFEHELFGVALKQAFGKDVESIYVKELGVTLSKDEIFKVLVHDM
MEGAIDVDWRDFFPYLKWIPNKSFEARIQQKHKRRLAVMNALIQDRLKQNGSESDD
DCYLNFLMSEAKTLTKEQIAILVWETIIETADTTLVTTEWAIYELAKHPSVQDRLCKE
IQNVCGGEKFKEEQLSQVPYLNGVFHETLRKYSPAPLVPIRYAHEDTQIGGYHVPAG
SEIAINIYGCNMDKKRWERPEDWWPERFLDDGKYETSDLHKTMAFGAGKRVCAGA
LQASLMAGIAIGRLVQEFEWKLRDGEEENVDTYGLTSQKLYPLMAIINPRRS

> *Ps*KAO2
GSMASLWFIFGAIAGALLVLRSLLKNVNWFLYEAKLGDKQYSLPPGDMGWPIIGNM
WSFLRAFKSSKPDSFMDSIVKRFGNTGIYKVFMFGFPSVIVTSPEACKKVLTDDENF
EPGWPQSTVELIGEKSFIKMPFEEHRRLRRLTSASINGYEALSVYLKYIEEIVISSLEKW
TQMGEIEFLTQMRKLTFKIIIHIFLGSESEPVMEALEREYTVLNLGVRAMRINIPGFAFH
KSLKARKNLVAIFQSIVDKRRNERRGKEPAPGKKAKDMMDSLIDAVDENGRKLGDD
EIIDIMLMYLNAGHESSGHITMWATYFLQRHPEFFRKAKEEQVEMLKRRPPSQKGLK
LEDVRKMEYLSKVIDETMRVVTFSLMVFRQARNDVKVNGYLIPKGWRVLTWFRSV
HFDSELYPDPREFNPENFSVVRKAGEFLPFGAGTRLCPGNDLAKLEISVFLHHFLLKY
ELEQLNPKSPIRFLPHTRPLDNCLARIKKQEAA

> *At*ATR2

GSMSSSSSSSTSMIDLMAAIIKGEPVIVSDPANASAYESVAAELSSMLIENRQFAMIVT
TSIAVLIGCIVMLVWRRSGSGNSKRVEPLKPLVIKPREEEIDDGRKKVTIFFGTQTGTA
EGFAKALGEEAKARYEKTRFKIVDLDDYAADDDEYEEKLKKEDVAFFFLATYGDGE
PTDNAARFYKWFTEGNDRGEWLKNLKYGVFGLGNRQYEHFNKVAKVVDDILVEQG
AQRLVQVGLGDDDQCIEDDFTAWREALWPELDTILREEGDTAVATPYTAAVLEYRV
SIHDSEDAKFNDINMANGNGYTVFDAQHPYKANVAVKRELHTPESDRSCIHLEFDIA
GSGLTYETGDHVGVLCDNLSETVDEALRLLDMSPDTYFSLHAEKEDGTPISSSLPPP
FPPCNLRTALTRYACLLSSPKKSALVALAAHASDPTEAERLKHLASPAGKDEYSKWV
VESQRSLLEVMAEFPSAKPPLGVFFAGVAPRLQPRFYSISSSPKIAETRIHVTCALVYE
KMPTGRIHKGVCSTWMKNAVPYEKSENCSSAPIFVRQSNFKLPSDSKVPIIMIGPGT
GLAPFRGFLQERLALVESGVELGPSVLFFGCRNRRMDFIYEEELQRFVESGALAELSV
AFSREGPTKEYVQHKMMDKASDIWNMISQGAYLYVCGDAKGMARDVHRSLHTIAQ
EQGSMDSTKAEGFVKNLQTSGRYLRDVW

> *At*CPS

GSMSLQYHVLNSIPSTTFLSSTKTTISSSFLTISGSPLNVARDKSRSGSIHCSKLRTQEY
INSQEVQHDLPLIHEWQQLQGEDAPQISVGSNSNAFKEAVKSVKTILRNLTDGEITISA
YDTAWVALIDAGDKTPAFPSAVKWIAENQLSDGSWGDAYLFSYHDRLINTLACVVA
LRSWNLFPHQCNKGITFFRENIGKLEDENDEHMPIGFEVAFPSLLEIARGINIDVPYDS
PVLKDIYAKKELKLTRIPKEIMHKIPTTLLHSLEGMRDLDWEKLLKLQSQDGSFLFSP
SSTAFAFMQTRDSNCLEYLRNAVKRFNGGVPNVFPVDLFEHIWIVDRLQRLGISRYFE
EEIKECLDYVHRYWTDNGICWARCSHVQDIDDTAMAFRLLRQHGYQVSADVFKNFE
KEGEFFCFVGQSNQAVTGMFNLYRASQLAFPREEILKNAKEFSYNYLLEKREREELID
KWIIMKDLPGEIGFALEIPWYASLPRVETRFYIDQYGGENDVWIGKTLYRMPYVNNN
GYLELAKQDYNNCQAQHQLEWDIFQKWYEENRLSEWGVRRSELLECYYLAAATIFE
SERSHERMVWAKSSVLVKAISSSFGESSDSRRSFSDQFHEYIANARRSDHHFNDRNM
RLDRPGSVQASRLAGVLIGTLNQMSFDLFMSHGRDVNNLLYLSWGDWMEKWKLYG
DEGEGELMVKMIILMKNNDLTNFFTHTHFVRLAEIINRICLPRQYLKARRNDEKEKTI
KSMEKEMGKMVELALSESDTFRDVSITFLDVAKAFYYFALCGDHLQTHISKVLFQKV

> *Cm*KS

GSMYLSRPTGVARFAASSSSSSSASLFPGVDVDTTTKTGALHFEETKERIKKLFDKV
ELSVSAYDTAWVAMVPSPNSLNQPLFPECINWVLDSQHADGSWGLLHNDQLLMKA
NLLSTLACVLTLKRWNIGHDHMSKALDFIKSNIASATDENQRSPVGFDIIFPGMIEYA
KDLNLNLPLAPTNVDALVRKKELELRSCRSNSEGGKAYLAYVSEGIGKLQDWDMVM
QYQRKNGSLFNSPSTTAAAFMHRNDDGCFDYLRSLLQKFDGSVPTIYPLDIYARLH
MVDSLQKFGIARHFKEEIRSVLDETYRCWMQGEENIFLDASTCAMAFRMLRVEGYD
VSSDQLTQFSEDIFPNCLGGYLKDFGASLELYKASQIITHPDESVLENINSWTSRFLKH
GLSSDSVWSDRTDSVVKQEAVNALEFPYNATLERLISKRAMESYSGDIVRISKSPYAC
LNFGHQDFLELAVEDFNTLQRIHLKELEELQRWVVENKLDELKFFRLHLGYCYFAAA
ATLTDPELHDARIAWAQNGVLTTVVDDFYDGGGSEEELDNLIELVEKWDPDGEVGY
CSKDVEIVFLALHSTVCEIGRRALVWQGRSVMRNVIDGWLALLKVMRKEAEWSTNK
VVPSMGEYMEQAHVSFALGPIILPMLFFVGPKLSEEMIGSCEYQKLYKLMSTAGRLK
NDIRSYDRECKEGKLNILSLWMIDGGGNVTKEEAIEAIKGDFERAIRELLGLVLQENTT
IPRACKDLFWKLMSIVNLFYMEDDGYTSNRLMNTVKAMFEQPMDLDALLNK

> *Ps*GA3Ox

GSMPSLSEAYRAHPVHVNHKHPDFNSLQELPESYNWTHLDDHTLIDSNNIMKESTT
TVPVIDLNDPNASKLIGLACKTWGVYQVMNHGIPLSLLEDIQWLGQTLFSLPSHQKH
KATRSPDGVSGYGIARISSFFPKLMWYEGFTIVGSPLDHFRELWPQDYTRFCDIVVQ
YDETMKKLAGTLMCLMLDSLGITKEDIKWAGSKAQFEKACAALQLNSYPSCPDPDH
AMGLAPHTDSTFLTILSQNDISGLQVNREGSGWITVPPLQGGLVVNVGDLFHILSNGL
YPSVLHRVLVNRTRQRFSVAYLYGPPSNVEICPHAKLIGPTKPPLYRSVTWNEYLGT
KAKHFNKALSSVRLCTPINGLFDVNDSNKNSVQVG

> YFP

MSKGEELFTGVVPILVELDGDVNGHKFSVSGEGEGDATYGKLTLKFICTTGKLPVPW
PTLVTTLGYGLMCFARYPDHMKQHDFFKSAMPEGYVQERTIFFKDDGNYKTRAEV
KFEGDTLVNRIELKGIDFKEDGNILGHKLEYNYNSHNVYIMADKQKNGIKVNFKIRHN
IEDGSVQLADHYQQNTPIGDGPVLLPDNHYLSYQSRLSKDPNEKRDHMVLLEFVTA
AGITHGMDELYKGS

> Clb2_db-psd3

MSNPIENTENSQNTSSSRFLRNVQTTFQKSNANNPALTNFKSTLNSVKKEGSRIPQF
TRESVSRSTAAQEEKRTLKENGIQLPKNNLLDDKENQDPSSQQFGALTSIKEGRAEL
PANISLQESSSAKEIIQHDPLKGVGSSTEVVHNSVENEKLHPARSQLQVRNTESETDS
GKKRPISTIVEQELPKKFKVCDENGKEEYEWEDLDAEDVNDPFMVSEYVNDIFEYLH
QLEVITLPKKEDLYQHRNIHQNRDILVNWLVKIHNKFGLLPETLYLAINIMDRFLGKEL
VQLDKLQLVGTSCLFIASKYEEVYSPSIKHFASETDGACTEDEIKEGEKFILKTLKFNL
NYPNPMNFLRRISKADDYDIQSRTLAKFLLEISLVDFRFIGILPSLCAAAAMFMSRKML
GKGKWDGNLIHYSGGYTKEELAPVCHMIMDYLVSPIVHDEFHRKYQSRRFMKASIIS
VQWALKVRKNGYDIMTLHESRGEQKLISEEDLNGEQKLISEEDLNGEQKLISEEDLNG
SSRVMRRGIDLATTLERIEKNFVITDPRLPDNPIIFASDSFLQLTEYSREEILGRNCRFL
QGPETDRATVRKIRDAIDNQTEVTVQLINYTKSGKKFWNVFHLQPMRDYKGDVQY
FIGVQLDGTERLHGAAEREAVMLIKKTAFQIAEAKELPMSCAQESITSLYKKAGSENL
YFQ

> Cdc48-mCherry-psd3

MGEEHKPLLDASGVDPREEDKTATAILRRKKKDNMLLVDDAINDDNSVIAINSNTM
DKLELFRGDTVLVKGKKRKDTVLIVLIDDELEDGACRINRVVRNNLRIRLGDLVTIHPC
PDIKYATRISVLPIADTIEGITGNLFDVFLKPYFVEAYRPVRKGDHFVVRGGMRQVEF
KVVDVEPEEYAVVAQDTIIHWEGEPINREDEENNMNEVGYDDIGGCRKQMAQIREM
VELPLRHPQLFKAIGIKPPRGVLMYGPPGTGKTLMARAVANETGAFFFLINGPEVMS
KMAGESESNLRKAFEEAEKNAPAIIFIDEIDSIAPKRDKTNGEVERRVVSQLLTLMDG
MKARSNVVVIAATNRPNSIDPALRRFGRFDREVDIGIPDATGRLEVLRIHTKNMKLAD
DVDLEALAAETHGYVGADIASLCSEAAMQQIREKMDLIDLDEDEIDAEVLDSLGVTM
DNFRFALGNSNPSALRETVVESVNVTWDDVGGLDEIKEELKETVEYPVLHPDQYTK
FGLSPSKGVLFYGPPGTGKTLLAKAVATEVSANFISVKGPELLSMWYGESESNIRDIF
DKARAAAPTVVFLDELDSIAKARGGSLGDAGGASDRVVNQLLTEMDGMNAKKNVF
VIGATNRPDQIDPAILRPGRLDQLIYVPLPDENARLSILNAQLRKTPLEPGLELTAIAKA
TQGFSGADLLYIVQRAAKYAIKDSIEAHRQHEAEKEVKVEGEDVEMTDEGAKAEQEP
EVDPVPYITKEHFAEAMKTAKRSVSDAELRRYEAYSQQMKASRGQFSNFNFNDAPL
GTTATDNANSNNSAPSGAGAAFGSNAEEDDDLYSRTLQVDMVSKGEEDNMAIIKEF
MRFKVHMEGSVNGHEFEIEGEGEGRPYEGTQTAKLKVTKGGPLPFAWDILSPQFMY
GSKAYVKHPADIPDYLKLSFPEGFKWERVMNFEDGGVVTVTQDSSLQDGEFIYKVK
LRGTNFPSDGPVMQKKTMGWEASSERMYPEDGALKGEIKQRLKLKDGGHYDAEVK
TTYKAKKPVQLPGAYNVNIKLDITSHNEDYTIVEQYERAEGRHSTGGMDELYKLQM
RRGIDLATTLERIEKNFVITDPRLPDNPIIFASDSFLQLTEYSREEILGRNCRFLQGPET
DRATVRKIRDAIDNQTEVTVQLINYTKSGKKFWNVFHLQPMRDYKGDVQYFIGVQL
DGTERLHGAAEREAVMLIKKTAFQIAEAKELPMSCAQESITSLYKKAGSENLYFQ

> hph::NT1
MGKKPELTATSVEKFLIEKFDSVSDLMQLSEGEESRAFSFDVGGRGYVLRVNSCADG
FYKDRYVYRHFASAALPIPEVLDIGEFSESLTYCISRRAQGVTLQDLPETELPAVLQPV
AEAMDAIAAADLSQTSGFGPFGPQGIGQYTTWRDFICAIADPHVYHWQTVMDDTV
SASVAQALDELMLWAEDCPEVRHLVHADFGSNNVLTDNGRITAVIDWSEAMFGDSQ
YEVANIFFWRPWLACMEQQTRYFERRHPELAGSPRLRAYMLRIGLDQLYQSLVDGN
FDDAAWAQGRCDAIVRSGAGTVGRTQIARRSAAVWTDGCVEVLADSGNRRPSTRP
RAKE

> tagRFP-bPAC
MSELIKENMHMKLYMEGTVNNHHFKCTSEGEGKPYEGTQTMRIKVVEGGPLPFAF
DILATSFMYGSRTFINHTQGIPDFFKQSFPEGFTWERVTTYEDGGVLTATQDTSLQD
GCLIYNVKIRGVNFPSNGPVMQKKTLGWEANTEMLYPADGGLEGRSDMALKLVGG
GHLICNFKTTYRSKKPAKNLKMPGVYYVDHRLERIKEADKETYVEQHEVAVARYCD
LPSKLGHKLQMMKRLVYISKISGHLSLEEIQRIGKVSIKNNQRDNITGVLLYLQGLFFQI
LEGENEKVDKLYKKILVDDRHTNILCLKTEYDITDRMFPNWAMKTINLNENSELMIQ
PIKSLLQTITQSHRVLEKYMPARVIYLINQGINPLTVEPQLVEKIIFFSDILAFSTLTEKL
PVNEVVILVNRYFSICTRIISAYGGEVTKFIGDCVMASFTKEQGDAAIRTSLDIISELKQ
LRHHVEATNPLHLLYTGIGLSYGHVIEGNMGSSLKMDHTLLGDAVNVAARLEALTRQ
LPYALAFTAGVKKCCQAQWTFINLGAHQVKGKQEAIEVYTVNEAQKYYDTLQITQLI
RQTLENDK

> kanMX6
MGKEKTHVSRPRLNSNMDADLYGYKWARDNVGQSGATIYRLYGKPDAPELFLKHG
KGSVANDVTDEMVRLNWLTEFMPLPTIKHFIRTPDDAWLLTTAIPGKTAFQVLEEY
PDSGENIVDALAVFLRRLHSIPVCNCPFNSDRVFRLAQAQSRMNNGLVDASDFDDER
NGWPVEQVWKEMHKLLPFSPDSVVTHGDFSLDNLIFDEGKLIGCIDVGRVGIADRYQ
DLAILWNCLGEFSPSLQKRLFQKYGIDNPDMNKLQFHLMLDEFF

5.0.6 Data Deposition

Data used for this thesis, including raw data of MS-experiments, was deposited on servers maintained by the the group of Prof. Dr. Essen. The folder structure of the deposited archive (without raw MS data) is listed below.

Biomass Analysis
- protein
  - 2L scale
  - proteomics experiment
- carbohydrates
- RNA
- DNA
- lipids
- amino-acids

Proteomics Analysis
- pivot tables
  - Cdc48
  - Clb2
  - bPAC
- fasta files

Product Quantification
- 3AMP
- cordycepin
- GA4

R-Scripts
- CellPlot
- pheatmap
- EnhancedVolcano